UNIVERSITY OF CAPE COAST

GENERATION AND AMPLIFICATION OF TERAHERTZ

RADIATION IN CARBON NANOTUBES

ABUKARI SULEMANA SEIDU

2011

UNIVERSITY OF CAPE COAST

GENERATION AND AMPLIFICATION OF TERAHERTZ

RADIATION IN CARBON NANOTUBES

BY

ABUKARI SULEMANA SEIDU

THESIS SUBMITTED TO THE DEPARTMENT OF PHYSICS OF THE

SCHOOL OF PHYSICAL SCIENCES, UNIVERSITY OF CAPE COAST, IN

PARTIAL FULFILMENT OF THE REQUIREMENTS FOR AWARD

OF DOCTOR OF PHILOSOPHY DEGREE IN PHYSICS

JANUARY 2011

DECLARATION

Candidate's Declaration

I hereby declare that this thesis is the result of my original research and that no part of it has been presented for another degree in this university or elsewhere.

………………………   Date …………………………

Abukari Sulemana Seidu

 (Candidate)

Supervisor's Declaration

We hereby declare that the preparation and presentation of the thesis were supervised in accordance with the guidelines on supervision of thesis laid down by the University of Cape Coast.

Principal Supervisor's Signature: ………   Date: ……………

Name: Professor S. Y. Mensah

Co-supervisor's Signature :   Date: January 03, 2011

Name: Professor Kofi W. Adu

ABSTRACT

The Boltzmann kinetic equation was used to investigate and derived theoretically the current density characteristics of carbon nanotubes exposed simultaneously to both constant (dc) and high-frequency (ac) electromagnetic fields. Generation and amplification of terahertz radiation at room temperature was predicted. We demonstrated that this can suppress electric current instabilities while still preserving a broadband THz gain. We have further shown that THz gain in the conditions of suppressed electric instabilities can be possible for direct current generation in carbon nanotubes by mixing two coherent electromagnetic waves with commensurate frequencies.

ACKNOWLEDGEMENTS

DEDICATION

I wholeheartedly dedicate this work to my dearest mother, Hajia Adisa Baba, my dearest wife, Mutiyatu Ibrahim Yahaya and my dearest uncle, Alhaji Abukari Baba Seidu whose encouragement and inspiration have helped to make me what I am today.

TABLE OF CONTENTS

LIST OF FIGURES

LIST OF TABLE

LIST OF SYMBOLS

THz	Terahertz Radiation
NDC	Negative Differential Conductivity
SLs	Superllatices
CNs/CNT	Carbon Nanotubes
MWCNTs	Multi-Walled Carbon Nanotubes.
SWCNTs	Single-Walled Carbon Nanotubes.
HRTEM	High Resolution Transmission Electron Microscopy
C_h	Chiral vector
T	Translation vector
d_l	Nanometer diameter
0D	Zero Dimensional
1D	One Dimensional
2D	Two Dimensional
3D	Three Dimensional
DOS	Density of State
NEC	Nippon Electric Company
IBM	International Business Machines
FETs	Field-Effect Transistors
MOSFET	Metal Oxide Semiconductor Field-Effect Transistor
CNFET	Carbon Nanotube Field-Effect Transistor
STM	Scanning Tunneling Microscopy
PDC/pdc	Positive Differential Conductivity
DC/dc	Direct current

AC/ac	Alternating current
CW	Continuous wave
BO	Bloch oscillator
ω_B	Bloch frequency
Ω/E_o	Electric field
$\sigma_E(\omega)/\sigma(\omega)$	Differential conductivity
τ	Electron relaxation time
β_1	Electric field amplitude
$J_k(\beta)$	Bessel function of the kth
j_z/j_o	Normalized current density
ω	Field frequency
ω/ω_B	Frequency (a.u)

CHAPTER ONE

INTRODUCTION

Terahertz Radiation

Terahertz (THz) radiation refers to the region of electromagnetic (EM) spectrum with frequency between 0.3THz and 10 THz. It is the borderline of photonics (i.e. high frequency edge of the microwave band) and electronics (i.e. long wavelength edge of far-infrared light) as depicted in Figure 1 [1-3]. The terahertz (THz) regime of the EM spectrum has not been explored until recently [2]; mainly due to the lack of suitable emitters (sources). The generation of wide spectral range of THz radiation is nowadays feasible in laboratory arrangements [3], however, due to the vast application potential and the size of existing generators, there is great demand for compact and reliable sources based on solid-state devices.
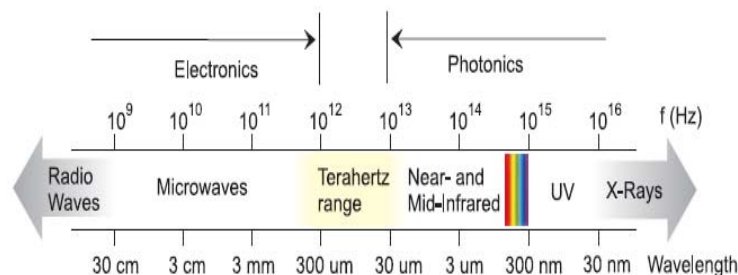
Figure 1: Electromagnetic (EM) spectrum [4].

Terahertz Radiation Applications and Opportunities

THz radiations provide a wide variety of applications and opportunities in different fields. Following the examples of reference [4] two main categories of THz applications; THz spectroscopy and THz imaging are briefly reviewed.

Spectroscopy is a measurement technique used to study the responses of a material to its interaction with electromagnetic radiation. The response is normally measured as a function of frequency. Terahertz frequencies are of particular interest because many chemical species' rotational and vibrational frequencies fall in this region, thus are useful for molecular spectroscopy [4, 5]. Astronomical and Atmospheric sciences are two areas where terahertz spectroscopy is used widely.

In astronomical science THz spectroscopy is normally used to study radiations from interstellar matter. A significant fraction of the energy emitted after the Big Bang falls into the range of THz radiation [4, 6, 7]. Therefore, the use of THz spectroscopy to study emission by cooled interstellar dust inside galaxies, gives information about star formation and decay [4, 6]. THz radiation received from space also contains information on the cosmic background radiation and distance of newly formed galaxies [4, 8]. Most of sub-millimeter spectroscopy for space applications has been done on satellite platforms due to the large THz absorption in the atmosphere.

THz spectroscopy has also been used in atmospheric science studies. The chemical processes related to ozone depletion and global warming could be studied according to the thermal emission from gasses such as water vapour, oxygen, and nitrogen compounds in the atmosphere [4, 5]. For example, the Earth

Observing System (EOS) is a coordinated series of satellites for long-term observation of the land surface, the biosphere, the solid Earth, the atmosphere, the and oceans. In this system a frequency of 2.5THz is used to monitor the OH level of the atmosphere [4, 9].

THz imaging was first developed by Hu and Nuss [10]. Since then the field has developed extensively and has attracted many reseachers in both academia and industry. THz imaging usually performed using ultra-short terahertz pulses generated by optical ulra-short pulses interacting with photoconductors or nonlinear crystals [4, 11]. Reflected or transmitted pulses are detected and image information is extracted from the phase and amplitude of the received signal. THz frequencies are of specific interest because many materials that are opaque in visible wavelengths are transparent in this region. Medical imaging of teeth or sub-dermal melanoma [4, 12, 13], and security imaging of concealed weapons [4, 14] are examples of this type of imaging.

Terahertz Generation Techniques

The generation and detection of THz radiation has been a challenging endeavor for many years and there is genearally a recognized "THz Gap" which stems from the fact that the energy levels involved in creating THz radiation fall below those used in photonic sources and beyond the inherent speed of electronic devices [4]. Electronic solid-state devices, such as transitors, Gunn oscillators and Schottky diodes multipliers are generally limited in frequency due to the transit time of carriers and resistance-capacitance effects which causes high frequency roll-off [4, 1]. On the other hand, photonic approaches to direct THz generation

are limited by lack of appropriate materials with small bandgap (1-10THz- 1-10meV) [4, 1]. Despite these limitations, many techniques have been developed to generate radiation at frequencies above 1THz [4, 1]. These techniques can be classified into three main categories: microwave up-convertors, optical down-convertors, and THz lasers. THz generation by up-conversion of microwave to the terahertz is done with chains of Schottky doublers or triplers whose frequencies are very low [4, 15].

Optical down-conversion can be used to generate THz frequency using optical nonlinearity or photoconductivity by applying optical short pulses or two optical wavelengths (for continuous-wave THz generation) [4, 16].

THz lasers are realized with optically pumped molecular gas lasers [4, 17], free electron lasers [4, 18], or quantum cascade lasers [4, 19]. Although many of these sources are very useful, each has its own advantages and disadvantages. The limitations of these THz generation sources have served as an impetus to develop a "perfect" terahertz source. In this section two classes of the most popular THz sources: quantum cascade lasers and photo-mixers, are briefly reviewed.

Quantum Cascade Laser

Quantum cascade lasers (QCLs) are semiconductor lasers that emit in the mid- to far-infrared portion of the electromagnetic spectrum and were first at Bell Laboratories in 1994 [4, 20]. In conventional laser diodes, electromagntic radiation is emitted via recombination of electron-holes pairs across the material band gap. However, in quantum cascade lasers, laser emission is achieved through the use of intersubband transitions in a periodic repetition of layers of two

different compositions, or superlattice structure (Figure 2) [4, 20]. A superlattice is a periodic structure of quantum wells and barriers. The photon emitted by the superlattice is due to the intersubband transition in the superlattic (as shown in Figure 2). Such transitions can be specified by the thickness of the coupled wells and barriers. Therefore, by toiloring the periodicity of the superlattice to specific well-barrier thickness, THz radiations of specified energy range can be generated. Althougth the idea of interband emission was known since 1971 [4, 21], the crystal growth technology for creating quantum cascade lasers is relatively new and expensive. Molecular beam epitaxy (MBE), in which individual monolayers can be grown, provides the required precision [4, 22]. Recent reports indicate advances in quantum cascade lasers for THz radiation generation [4, 19].
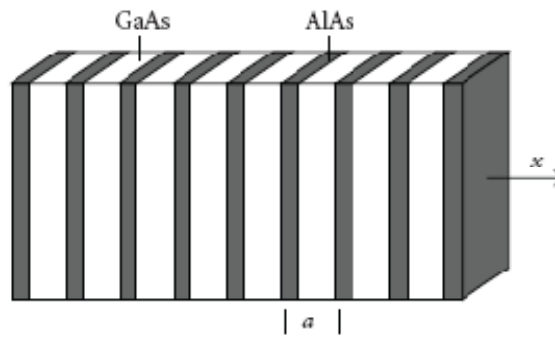
Figure 2: Superlattice. The superlattice consists of GaAs and AlAs layers in turn. A GaAs layer and an adjacent AlAs layer form one superlattice period (length *a*) along the superlattice axis (*x*) [19].

Currently, THz quantum cascade lasers have been realized to generate radiation in the 1.2-5THz range with powers up to tens of mW [19]. There are two main drawbacks of these THz sources; poor beam patterns and low working

temperature. So far the highest temperature attained for a THz source operating at 3THz frequency is 160K [4, 23].

Photo-Mixers

Photo-mixers are the most common THz sources and are commonly available up to 2THz with output power in μW range [1, 2, 4]. The continuous wave generation of high frequency radiation by photomixing uses two lasers emitting at nearly the same wavelengths, but detuned by the THz frequency generate carriers in a semiconductor. The beat of two incident frequencies then modulate the carrier density in the crystal, and therefore the conductivity between the electrical contacts of the material. If these photogenerated carriers are subject to a DC electric field applied between the two cntacts, a THz current is induced that can be connected to an antenna to radiate [4]. The ultra-short THz pulses could be generated from the carrier density modulation by applying ultra-short optical pulses to the photo-mixer [4].

Photomixer based THz sources are limited in frequency due to the carrier recombination lifetime and carrier transit time or mobility in semiconductors. Low temperature grown GaAs is one of the mostly widely used material for THz photomixing [4, 24] which has a recombination lifetime of 130fs corresponding to 3 dB frequency of 1.2THz. While highly suitable and readily available for effecient operation up to this frequency, extending operation to multiple THz remains a challenge and new materials (such as carbon nanotubes) are proposed for this purpose [4, 16].

Scope of Work

Creating a compact reliable source of THz radiation is one of the most formidable tasks of comtemporary applied physics [16]. So much work has been done on superlattices (SLs) material. In 1970 Esaki and Tsu [25] reported that a semiconductor superlattice (SL) biased by a strong electric field would, under certain favourable conditions, exhibit a negative differential conductivity (NDC) up to frequencies on the order of the Bloch oscillation frequency. This made the SL a potential candidate for the active medium in a Bloch oscillator (BO) operating up into the terahertz regime. Such superlattice could be used in the generation of THz radiation [26]. In 1972 S.A. Ktitorov and co-workers [27] showed that the linear differential conductivity $\sigma_E(\omega)$ of a biased superlattice is negative up to the Bloch frequency. Later A.A. Ignatov, *et al* [28] calculated the finite-field ac response of a biased superlattice and showed that the amplification efficiency, i.e the ratio of power absorbed by a THz field and the power delivered from a bias source, is larger at larger ac fields. That is what one needs to make an oscillator work at $\omega \sim \Omega$ (where ω is the field frequency and Ω is the Bloch frequency). However, $\sigma_E(\omega)$ is also negative as $\omega \longrightarrow 0$, and this dc negative differential conductivity (NDC) leads to a low frequency instability of the space-charge waves and to the formation of domains [29, 30]. The electric domains (i.e. depletion layers, accumulation layers, or a combination of both inside or at the boundary of the SL) are believed to be destructive for the THz gain in superlattices [31]. For a Bloch oscillator to operate the domain instability should be suppressed [32]. It was shown by A.Yu. and coworkers [33] and also by H. Kroemer [34] that in the nonlinear regime with high enough frequency, the dc

differential conductivity is positive, while the large-signal high-frequency differential conductivity still remains negative, consequently, the steady-state operation of a Bloch oscillator in large-signal regime can be achieved.

Recently, Mensah, 1992 [35] studied the negative differential effect in a semiconductor superlattice in the presence of an external electric field. The theory indicated that the current-density electric field characteristic shows a negative differential conductivity when $\omega\tau << 1$ (where ω is the field frequency and τ is the electron relaxation time) and this occurs in the neighbourhood where the constant electric field E_o is equal to the amplitude of the ac electric field E_1 and the peak decreases with increasing E_1. The theory agrees with the recent experiment [36] that indicated "right shift" of the IV maximum, (i.e. increasing the electric field will result in the peak value of the current-density shifts towards greater values of the electric field and then decreasing) which is typical for a SL without domain formation. In reference [36], the authors demonstrated ultrafast creation and annihilation of space-charge domains in a semiconductor superlattice. They observed this by the use of THz fields.

One of the latest trends in THz technology [37] is to use carbon nanotubes:-cylindrical molecular structures of high aspect ratio (nanometer diameter and micrometer length) [38-41] as building blocks off novel high-frequency devices. There are several promising proposals of using carbon nanotubes for THz applications. These include (but not limited to) nanoklystron which utilizes extremely efficient high-field electron emission from nanotubes [37, 42], devices based on negative differential conductivity in large diameter semiconducting nanotubes [43, 44] high-frequency resonant-tunneling diodes [45]

and Schottky diodes [46-49], electric-field-controlled carbon nanotube superlattices [50] frequency multipliers [51, 52] THz amplifiers [53] switches[54] and antennas [55].

Maksimenko et al [43] suggested that simultaneously applied dc- and ac-fields will result in the dynamic electron localization (which is the nonlinear phase of the instability) and in a 2D analogue of the self-induced transparency. The above mentioned effects are responsible for the absolute negative conductivity predicted to be exhibited in CNs [43]. This could lead to absolute negative conductivity zones in the properties of CNs. This provides the potential to design nanodiodes in microwave and infrared ranges with both single CNs and bundles of CNs [43].

In this work we study theoretically the scheme for generation and amplification of THz radiation in dc-biased CNs at room temperature using monochromatic alternating pump field and direct current generation by mixing two coherent electromagnetic waves with commensurate frequencies. This approach suppresses electric current instabilities while simultaneously preserving broadband THz gain.

The proposed theoretical studies are performed within the semiclassical Boltzmann kinetic equation approximation.

Organization of Work

This work is organized as follows: a review of the literature on THz radiation and its sources is given as introduction in chapter one while a review of the literature on CNs is given in chapter two. Chapter three focuses on the

9

theoretical investigation of amplification of THz radiation in dc-ac driven CNs at room temperature using the semiclassical Boltzmann kinetic approximation. The discussions of the results in this theoretical investigation are presented in chapter four. The conclusions and recommendations for future work are given in chapter five.

CHAPTER TWO

LITERATURE REVIEW

History of Carbon Nanotubes

Fullerenes were discovered in 1985 by Rick Smalley and coworkers [55]. C_{60} was the first fullerene to be discovered. C_{60}, or "bucky ball," is a soccer ball (icosahedral)-shaped molecule with 60 carbon atoms bonded together in pentagons and hexagons. The carbon atoms are sp^2 hybridized, but in contrast to graphite, they are not arranged on a plane. The geometry of C_{60} strains the bonds of the sp^2 hybridized carbon atoms, creating new properties for C_{60}. Graphite is a semimetal, whereas C_{60} is a semiconductor [56].

The discovery of C_{60} was, similar to many other scientific breakthroughs, unintended result of a synthesis experiment. It started because Kroto [56] was interested in interstellar dust, the long-chain polyynes formed by red giant stars. Smalley and Curl [57] developed a technique to analyze atom clusters produced by laser vaporization with time-of-flight mass spectrometry, which caught Kroto's attention. When they used a graphite target, they could produce and analyze the long chain polyynes (Figure 3a). In September of 1985, the collaborators experimented with the carbon plasma, confirming the formation of polyynes [56].

They observed two mysterious peaks at mass 720 and, to a lesser extent, 840, corresponding to 60 and 70 carbon atoms, respectively (see Figure 3b).
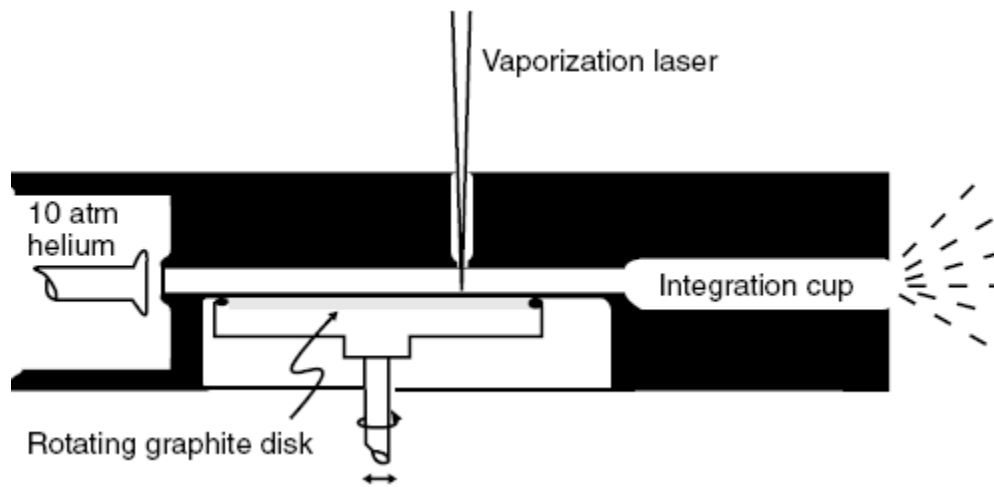
(a)
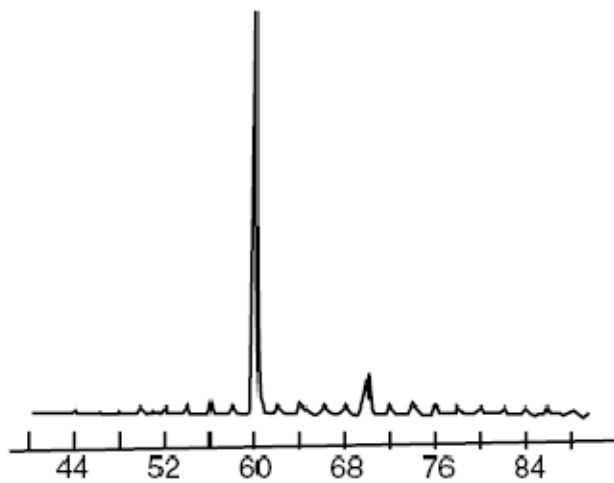
Number of carbon atoms per cluster

(b)

Figure 3: (a) Schematic of the pulsed supersonic nozzle used to generate carbon cluster beams. (b) Time-of-flight mass spectra of carbon clusters prepared by laser vaporization of graphite [55].

Further theoretical and experimental investigations confirmed a spherical structure, leading to the conclusion that C_{60} is made of 12 pentagons and 20 hexagons arranged to form a truncated icosahedrons [55, 57] (see Figure 4).

In 1990, at a carbon-carbon composites workshop, Rick Smalley proposed the existence of a tubular fullerene [58]. He envisioned a bucky tube that could be made by elongating a C_{60} molecule. In August of 1991, Dresselhaus followed up in an oral presentation in Philadelphia at a fullerene workshop on the symmetry proposed for carbon nanotubes capped at either end by fullerene hemispheres [59]. Experimental evidence of the existence of carbon nanotubes came in 1991 when Iijima imaged multiwalled carbon nanotubes (MWNTs) using a transmission electron microscope [38] (as indicated in Figure 4). Two years later, Iijima and coworkers [60] and Bethune and coworkers [61] simultaneously and independently observed single walled carbon nanotubes (SWNTs).
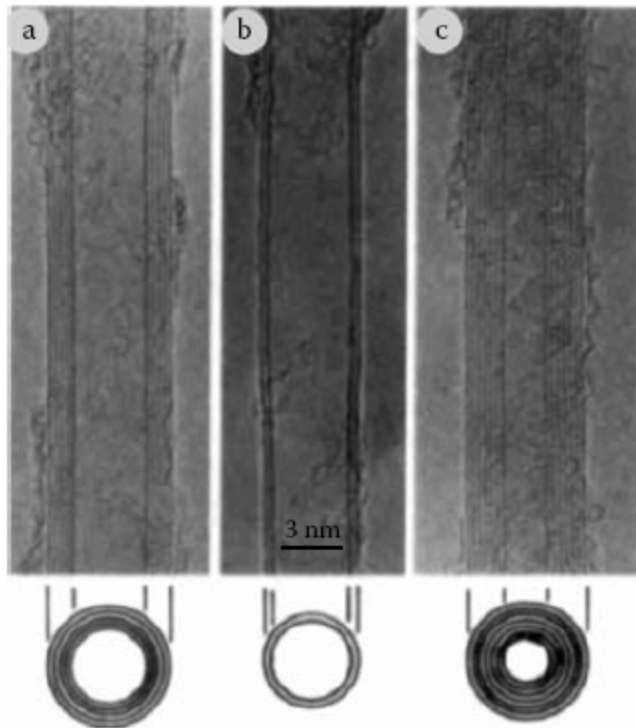
Figure 4: Transmission electron micrographs (TEMs) of the first observed multiwalled carbon nanotubes (MWNTs) reported by Iijima in 1991 [56].

Although Ijima is credited with their official discovery of carbon nanotube, it was probably already observed thirty years earlier from Bacon at Union Carbide in Parma, Ohio, USA. He was studying the melting of graphite under high temperatures and pressures and probably found carbon nanotubes in his samples. In his paper, published in 1960, he presented the observation of carbon nanowhiskers under SEM investigation of his material [62] and he proposed a scroll like-structure. Nanotubes were also produced and imaged directly by Endo in the 1970's via high resolution transmission electron microscopy (HRTEM) when he explored the production of carbon fibers by

14

pyrolysis of benzene and ferrocene at 1000°C [63]. He observed carbon fibers with a hollow core and a catalytic particle at the end. He later discovered that the particle was iron oxide from sand paper. Currently, Iron is well-known as a catalyst in the production of carbon nanotubes.

Although carbon nanotubes were observed four decades ago, it was not until the discovery of C_{60} and theoretical studies of other possible fullerene structures that the scientific community realized their importance. Since then, carbon nanotube research has developed into a leading area in nanotechnology expanding at an extremely fast pace [56].

Structural Forms of Carbon

Carbon is the most versatile element in the periodic table, owing to the type, strength, and number of bonds it can form with many different elements. The diversity of bonds and their corresponding geometries enable the existence of structural isomers, geometric isomers, and enantiomers. These are found in large, complex, and diverse structures of endless variety of organic molecules [56].

The properties of carbon are a direct consequence of the arrangement of electrons around the nucleus of the atom. There are six electrons in a carbon atom, shared evenly between the 1s, 2s, and 2p orbitals. Since the 2p atomic orbitals can hold up to six electrons, carbon can make up to four bonds. However, the valence electrons involved in chemical bonding occupy both the 2s and 2p orbitals. Covalent bonds are formed by promotion of the 2s electrons to one or more 2p orbitals. The resulting hybridized orbitals are the sum of the original orbitals. The hybridization can occur in three different ways

depending on the number of p orbitals involved. In the first type of hybridization, the 2s orbital pairs with one of the 2p orbitals, forming two hybridized sp^1 orbitals in a linear geometry, separated by an angle of 180°. The second type of hybridization involves the 2s orbital hybridizing with two 2p orbitals; as a result, three sp^2 orbitals are formed. These are on the same plane separated by an angle of 120°. In the third hybridization, one 2s orbital hybridizes with the three 2p orbitals, yielding four sp^3 orbitals separated by an angle of 109.5°. sp^3 hybridization yields the characteristic tetrahedral arrangements of the bonds. In all three cases, the energy required to hybridize the atomic orbitals is given by the free energy of formation of chemical bonds with other atoms [56].

Carbon can bind in a sigma (σ) bond and a pi (π) bond in forming a molecule. The final molecular structure depends on the level of hybridization of the carbon orbitals. An sp^1 hybridized carbon atom can make two σ bonds and two π bond. The sp^2 hybridized carbon forms three σ bonds and one π bond. Whereas, an sp^3 hybridized carbon atom forms four σ bonds. The number and nature of the bonds determine the geometry and properties of carbon allotropes (see Figure 5) [56].

Prior to the discovery of fullerenes, graphite and diamond were the only known crystalline forms of carbon. Diamond has sp^3 –hybridized structure, forming a three-dimensional (3D) network by binding the tetrahedral unit structures together, whereas the sp^2 hybridization in graphite links carbon atoms in a two-dimensional (2D) layer of hexagons. C_{60} fullerenes, the 0-dimensional (0D) molecule has a particular shape like a "soccer ball" (so-called "buckyball"). These fullerenes are made up of 60 carbon atoms arranged in pentagonal and

hexagonal rings. The discovery and subsequent synthesis in macroscopic quantities of fullerenes has initiated a new field in the chemistry and physics of carbon.
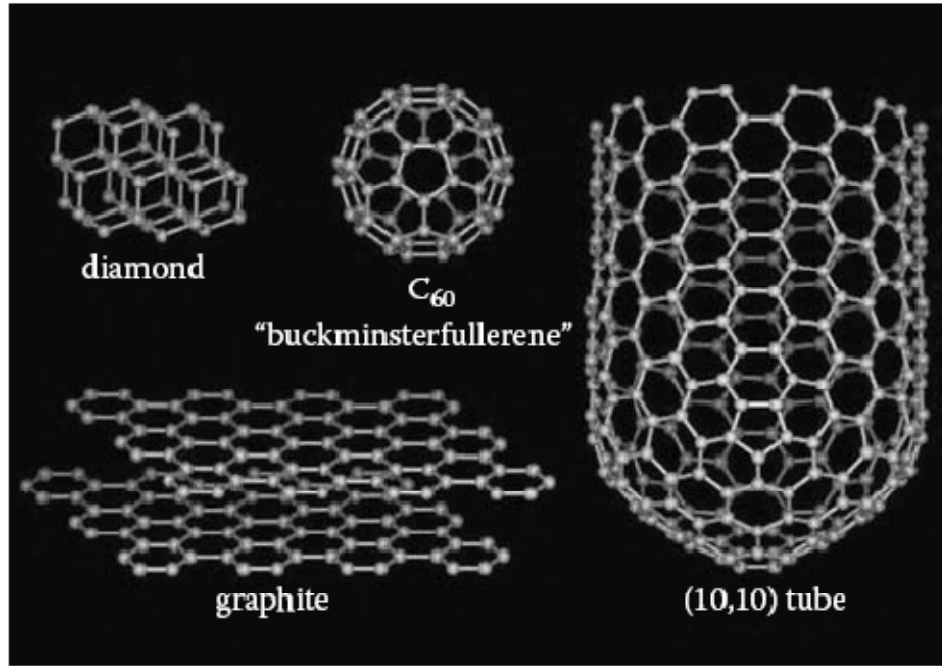
Figure 5: Allotropes of carbon [64].

Whereas fullerenes are usually spherical in shape, carbon nanotubes (CNTs) on the other hand are long, thin seamless hollow cylinders of graphene sheets, closed at each end with a hemispherical cap which contain precisely six pentagonal rings. The name is derived from its size. They contain an array of carbon atoms in a long, thin hollow cylinder with diameter ranging between 0.5nm to 3.5nm and microns long. A nano metre is one billionth of a metre, or about 100,000 times smaller than a human hair. They can be viewed as single molecules, regarding their small size, or as quasi-one dimensional crystals with

translational periodicity along the tube axis. Simply put, carbon nanotubes exist as a large macromolecule of carbon, analogous to a grahene sheet rolled into a cylinder [64, 65].

Nanotubes have an impressive list of attributes. They are light, flexible, thermally stable and chemically inert. They can be metal or semiconductor depending on the "chirality" of the tube, can conduct electricity better than copper, can transmit heat better than diamond, and they are ranked among the strongest materials known [64, 66, 67].

These large macromolecules are unique for their size, shape and remarkable physical properties. These intriguing structures have sparked much excitement in recent years and a large amount of researched has been dedicated to their understanding. Since the discovering of carbon nanotubes (CNTs) by Iijima in 1991 [67], increasing attention has been attracted to this newly emerging material due to its remarkable mechanical and electrical properties [68, 69].

The summary of notable properties of carbon nanotubes are:

i.   Carbon nanotubes can be metallic, semiconducting, or insulating depending on their length, diameter and rolling helicity [70], and do not requiring any doping.

ii.   The energy gap of semiconducting carbon nanotubes can be varied continuously by varying the nanotube diameter. Here the band gap of semiconducting nanotubes decreases with increasing diameter [71].

iii. Individual carbon nanotubes are able to carry electrical current at significantly higher densities than most metals and semiconductors

(maximum current density~ 10^{13} A/m^2) [72, 73, 74].

iv.   Nanotubes have high thermal conductivity (~ 2000 W/m/K, whereas copper has 400 W/m/K) [72, 75].

v.   Nanotubes are also inert and have no surface states, making them very compatible with other materials such as oxides.

vi.   Nanotubes can be either grown at specific locations, or simply dispersed from solution.

vii. A nanotube device will consume less power than an equivalent Si device.

These properties make carbon nanotube device a better choice than other molecular device.

Classification of Carbon Nanotubes

There are two broad categorizations of CNTs possible in terms of the physical structure. If the tube is mono-atomic, that is, the surface (and the tube itself) is composed of a single layer of carbon atoms, we have a structure known as the single wall carbon nanotube (SWCNT). Because of certain fabrication procedures, however, CNTs obtained with more than one layer of carbon atoms, such a structure may be viewed as a multi-walled carbon nanotube (MWCNT), where two or more CNTs are coaxially aligned.

In Figure 6, examples of a SCWNT and a MCWNT are shown.
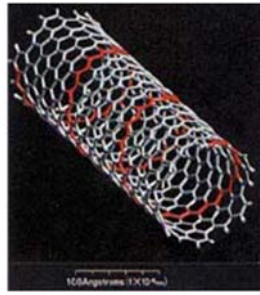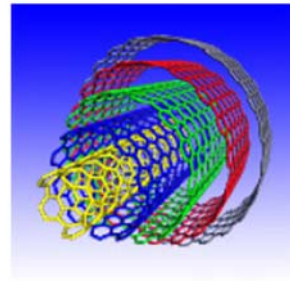
(a)   (b)

Figure 6: The structure of a single wall (SWCNT) (a) and a multi wall (MCWNT) (b) carbon nanotubes [64]. The SWCNT is a hollow cylinder of graphite while the second one is an array of coaxial nanotubes.

In general the MWCNTs have a larger diameter than the SWCNTs.

Single-wall nanotubes with only one single layer generally have a diameter of 1 to 5 nm . The properties of SWCNT are more stable than MWCNT so it is more favourable. MWCNT is a little bigger than SWCNT because MWCNT has about 50 layers. MWCNT's inner diameter is from 1.5 to 15 nm and the outer diameter is from 2.5 nm to 30 nm. Distances between the walls are mostly found to be between 0.1 and 0.4 nm [60]. Depending on the number of walls, CNTs may have different conductive properties. For example, MCWNTs have metallic conducting properties, whereas SWCNTs can have semi conducting properties as well as metallic conducting properties. This depends on the so-called chirality of the SWCNTs.

Both SWCNT and MWCNT are usually many microns long and hence they can fit well as components in submicrometer-scale devices and nanocomposite structures that are very important in emerging technologies.

SWCNT have better defined shapes of cylinder than MWCNT, thus MWCNT has more possibilities of structure defects and its nanostructure is less stable. Most researchers focus on SWCNT and develop applications based on SWCNT due to the physical stability of SWCNT.

The second form of classification is common among both MWCNTs and SWCNTs and depends on the arrangement of carbon atoms in a given tube or how the two-dimensional graphene sheet is "rolled up". The primary symmetry classification of a carbon nanotube is as either being achiral (symmorphic) or chiral (non-symmorphic). An achiral carbon nanotube is defined by a carbon nanotube whose mirror image has an identical structure to the original one. There are only two cases of achiral nanotubes:

a) armchair and

b) zigzag nanotubes

The names of armchair and zigzag arise from the shape of the cross-sectional ring, as shown at the edge of the nanotubes in Figure 7 (a) and (b). An armchair nanotube corresponds to the case of $n = m$, (ie, n, m is a chiral index) that is $C_h = (n,n)$; and a zigzag nanotube corresponds to the case of $m = 0$ or $C_h = (n,0)$. Chiral nanotubes exhibit a spiral symmetry whose mirror image cannot be superposed on to the original one. All (n,m) chiral vectors other than (n,n) and $(n,0)$ correspond to chiral nanotubes. Because of the hexagonal symmetry of the lattice, we need to consider only $0 < |m| < n$ in $C_h = (n,m)$ for chiral nanotubes.
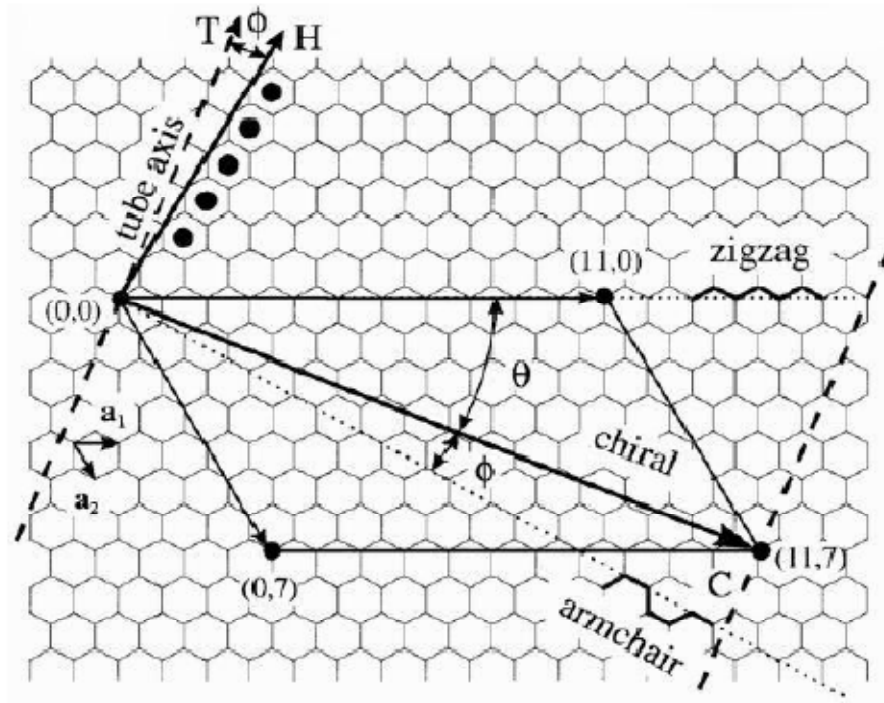
Figure 7: Shows the chiral and the translation vectors in the case of the unrolled hexagonal lattice of a (4, 2) carbon nanotube [40].

This classification depends on the geometric structure of CNTs described by the circumference vector or Chiral vector of the nanotube, C_h , whose magnitude represents the full circumference of the tube. It is defined by $C_h = na_1 + ma_2$, where a_1 and a_2 are unit vectors in the two-dimensional hexagonal lattice. The integers n and m denote the number of unit vectors along two directions in the hexagonal lattice of graphene. This is often thought of as representing the number of carbon atoms around the circumference of the tube, and the number of atoms down the tube axis. Another important parameter is the chiral angle θ, which is the angle between C_h and a_1

Armchair carbon nanotubes are formed when $n = m$ and the chiral angle is 30°. Zigzag carbon nanotubes are formed when either n or m is zero and the chiral angle is 0°. All other carbon nanotubes formed when $n \neq m$, n or $m \neq 0$ with chiral angles intermediate between 0° and 30°, are known as chiral carbon nanotubes.

The chiral vector is a line that traces the CNs along its circumference from one carbon atom (we will call it the reference atom) back to itself. If we cut open the carbon nanotube along the tube axis and through the reference atom, we can imagine spreading out the nanotube into a graphene sheet that could exactly match a portion of an infinitely large graphene sheet. Figure7 shows the hexagonal carbon network that can be thought of as the infinitely large graphene sheet. The dotted lines at the left and right represent the cut made along the CNT. Location (0,0) represents the reference atom and is the location that the chiral vector C_h starts from. Although the chiral vector begins and ends on the same reference atom, end is represented by location (11,7) in the graphene sheet, shown in Figure 7. When the graphene sheet is wrapped into a cylinder, chiral vector C_h which connects crystalographically equivalent points (0,0) and (11,7) of the graphene lattice will both converge on the same reference atom. The unit vectors a_1 and a_2 both begin at one corner of a single hexagon and end two corners away in the same hexagon. Each hexagon corner in the hexagonal network represents one carbon atom in the physical graphene sheet. a_1 and a_2 point in the zigzag directions, or directions that make 30° angles with the armchair direction. Since a_1 and a_2 each transverse one whole hexagon, the coordinates *(n,m)* represent atoms that are n and m hexagons away from the reference atom in the a_1 and a_2

23

directions respectively. a_1 points in the indicated zigzag direction, 30° away from the armchair direction. If C_h lines up with the dotted zig-zag line in Figure 7, the resulting nanotube would be a zigzag CNT. The terms zigzag and armchair come from the patterns traced along the hexagons along those directions, as shown by the zigzag and armchair-like lines drawn in Figure 7. The angles θ and Φ always combine to form 30° [64, 65]. The chiral angle and vector also play an important role in determining the important properties of nanotubes , besides being parameters used to discriminate between different types of carbon nanotubes, The properties of carbon nanotubes are also determined by their diameter, which depends on n and m [40]. The nanotube diameter is calculated using the formula given by

$$d_t = \sqrt{3a_{c-c}}(m^2 + mn + n^2)/\pi = C_h/\pi, \qquad (1)$$

where a_{c-c} is the distance between adjacent carbon atoms in the flat sheet or a_{c-c} is the C-C bond length (0.142 nm) and C_h is the length of the circumference or chiral vector C_h.

The chiral angle θ, on the other hand is calculated using the formula given by

$$\theta = \tan^{-1}\left(\sqrt{3n}/(2m+n)\right) \qquad (2)$$

The translational vector $\mathbf{T}$, which is perpendicular to the chiral vector, is expressed as,

$$\mathbf{T} = [(2m+n)\mathbf{a}_1 - (2n+m)\mathbf{a}_2]/d_R. \qquad (3)$$

The length T is the unit lattice length along the tube axis direction:

$$T = \sqrt{3}C_h / d_R = 3a_{c-c}\sqrt{n^2 + nm + m^2} / d_R. \qquad (4)$$

Here, d_R is the greatest common divisor of $(2n+m)$ and $(2m+n)$. For example, let consider a (11, 8) tube: $2n+m=30$ and $2m+n = 27$ and $d_R=3$.

or

$$d_R = \begin{cases} d & \text{if } n-m \text{ is not a multiple of } 3d \\ 3d & \text{if } n-m \text{ is a multiple of } 3d \end{cases} \qquad (5)$$

and d is the highest common divisor of (n, m). For example, let consider a (11, 8) tube : d is 1 and hence $d_R=3$ since $11-8 =3$ is a multiple of $3(1)=3$

The number of hexagons N in a unit cell is given by,

$$N = \frac{2(n^2 + nm + m^2)}{d_R} \qquad (6)$$

One of the most remarkable properties of a given (n,m) carbon nanotubes is that depending on their structure and diameter , conducting or semiconducting nanotubes are possible. The condition for metallic or conducting nanotubes is that $(2n+m)$ or equivalently (n-m) is a multiple of 3.That is for a given (n,m) nanotube, if $2n + m=3i$ or $n-m=3i$ (where i is an integer), then the nanotube is metallic, otherwise the nanotube is a semiconductor. This leads to the cases that all armchair nanotubes are metallic or conducting, and zigzag nanotubes are only metallic or conducting if n is a multiple of 3. Figure 8 shows which carbon nanotubes are predicted to be metallic and which are semiconducting, denoted by the yellow and blue circles respectively. It can be seen from this diagram that approximately one third of carbon nanotubes are metallic or conducting while the other two thirds are semiconducting. These

basic predictions from the theory have been verified using scanning tunnelling microscope studies.
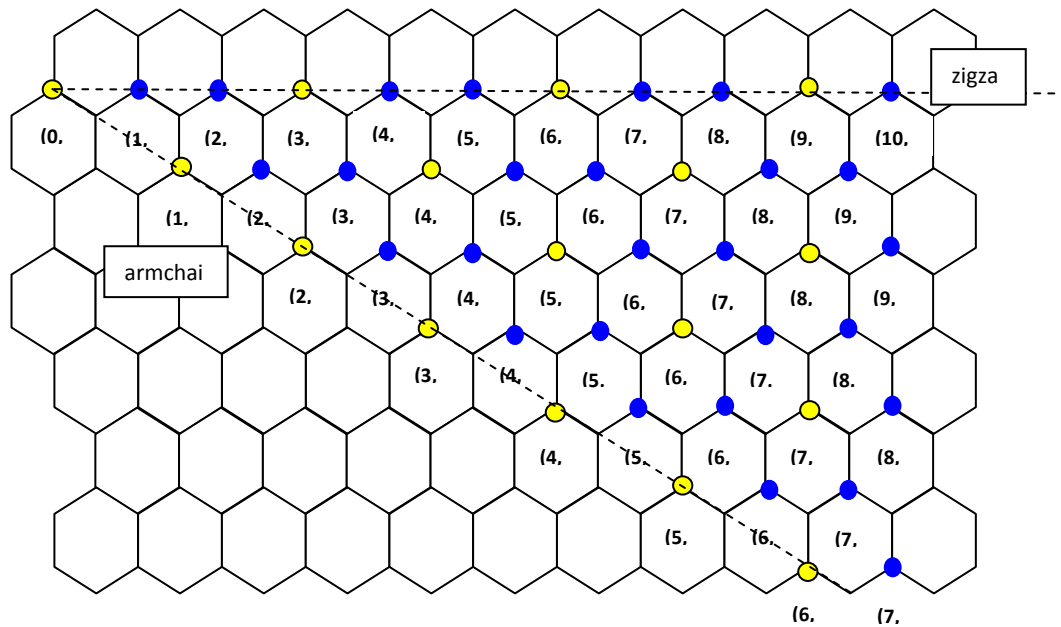
Figure 8: The carbon nanotubes (n,m) that are metallic are denoted by a yellow dot and the semiconducting ones are denoted by blue dots [40].

Zigzag nanotubes correspond to (*n*, 0) or (0, *m*) and have a chiral angle of 0°, armchair nanotubes have (*n*, *n*) and a chiral angle,θ, of 30°, while chiral nanotubes have general (*n*, *m*) values and a chiral angle of between 0° and 30°.

Band-structure calculations show that the conductive properties of nanotubes depend strongly on the tube diameter as well as on the winding of the chiral

angle. Small changes in the said properties can transform the tube from a metal into a large-gap semiconductor
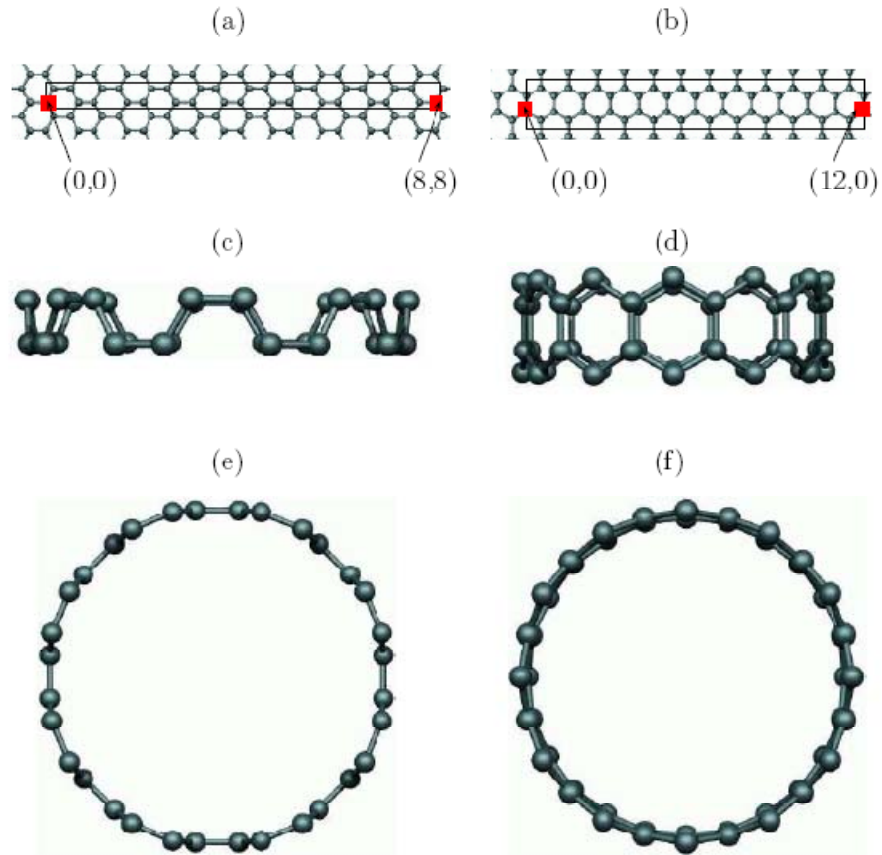
Figure 9: The planar unit cells of (a) (8,8) and (b) (12,0) nanotubes surrounded by rectangles and their start and end positions are marked by squares, and the fully optimised structure of the (c,e) (8,8) and (d,f) (12,0) nanotubes, top and side views [72].
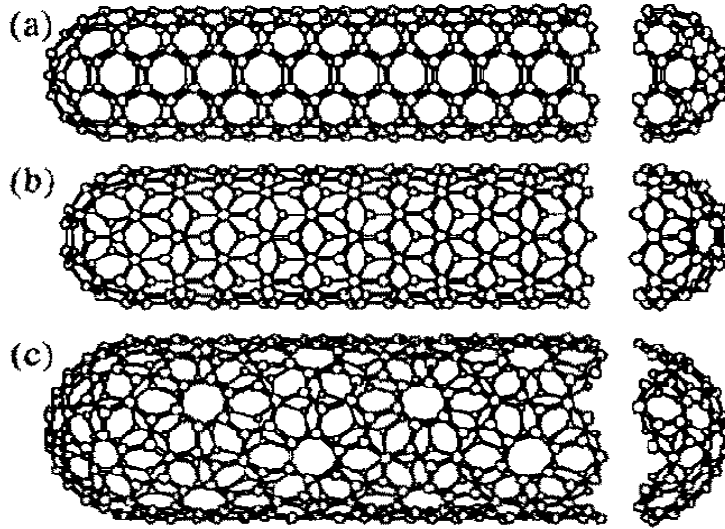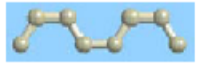
Figure 10: Classifications of carbon nanotubes: (a) armchair, (b) zigzag, and (c) chiral nanotubes.

From Figure 10 above it can be seen that the orientation of the six-membered ring in the honeycomb lattice relative to the axis of the nanotube can be taken almost arbitrarily.

Zigzag nanotubes are formed when either n or m is zero, hence it is referred to $(n,0)$ or $(m,0)$ tube structure and chiral angle ,θ, is 0° , also referred to as the zigzag axis and Chiral nanotubes are formed when either n or m is not zero and also $n \neq m$., hence it is general chiral (n, m) nanotube which corresponds to a chiral angle lying between $0^{o} < \theta < 30^{o}$.

Table 1 Classification of Carbon nanotubes [39].

Type	Chiral Vector, C_h	Length of Chiral Vector, L	Chiral Angle, θ	Number of hexagons in a unit cell, N	Shape of Cross-Section
Armchair	(n,n)	$\sqrt{3}\ na$	30^0	$2n$	Cis-type:
Zigzag	$(n,0)$	na	0^0	0	Trans-type:
Chiral	(n,m)	$a\sqrt{n^2+nm+m^2}$	$0^0<\mid\theta\mid<30^0$	$\dfrac{2(n^2+nm+m^2)}{d_R}$	Mixture of cis and trans.

Carbon nanotubes are subject of many theoretical and experimental studies [76-81]. It is a material with extraordinary properties and with a wide variety of possible applications [82, 83]: a few examples are field effect transistors, field emission devices, composite materials, nanotube sensors, hydrogen storage, lighting elements, memory device, optoelectronic, diode, ultraminiaturized electronics, new x-ray machine ,drug delivery vehicle, biomedicine ,fibre and fabrics [84-88, 89].

Typical Energy Dispersion Relations for Metal, Semiconductor and Semimetal

Before starting with the band structure of graphene, we would briefly mention the principal band structures of solids. One could distinguish between metals, semiconductors, insulators, and semi-metals.

Important for this differentiation is whether the Fermi level (E_F) lies in the conduction band, the valence band, or within a band gap. The Fermi level is defined as the energy at which the probability of occupation of the electron states is 1/2. In solids, the valence band is the band with the highest range of electron energies where the electrons are present at zero temperature (0K). In contrast, the conduction band is the band in which the electrons are free to be accelerated under the influence of an applied electric field. It is, therefore, located at higher energies than the valence band. Both bands are separated by a band gap Eg.

A metal is characterized by the position of the Fermi level within the conduction band, which is, therefore, also the valence band. Metals conduct electricity easily because there are so many electrons with easy access to adjacent conduction states. A semiconductor, in contrast to a metal, is characterized by a finite band gap between a filled valence and an empty conduction band at 0K. In an undoped (intrinsic) semiconductor the Fermi level lies in the middle of the band gap (Figure 11 (b)). An excitation of the electrons in the valence band is necessary to transfer them into the conduction band and to allow electronic transport in a semiconductor. Therefore, in semiconductors, electrons need an energy boost from light or electric field to jump the gap to the first available conduction state as shown in Figure 11. The amount of energy needed depends on

the separation between the two levels. Doping the semiconductor will shift the Fermi level either towards the valence band or towards the conduction band, making the semiconductor p-type or n-type, respectively.

In a p-type semiconductor holes are the majority carriers and electrons the minority carriers, whereas in a n-type semiconductor it is vice versa. If the band gap becomes too large one obtains an insulator, where excitations of electrons into the conduction band become very unlikely.

A particular case is a semi-metal, which is neither a distinct metal nor a real semiconductor. In a semi-metal the Fermi level is degenerated to a single point – the Fermi point (K-point) (Figure 11(c)). The valence band of a semi-metal is almost completely filled whereas the conduction band is almost completely empty. The graphite is a semimetal that just barely conducts, because without the external boosts such as external electric field or light, only a few electrons can access the narrow path to a conduction band.
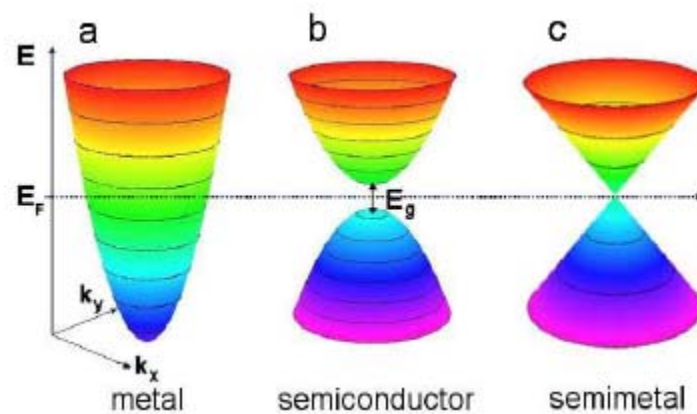
Figure 11: Simplified band structures of a metal (a), a semiconductor (b), and a semi-metal (c) [93].

Electrical properties of a material depend on the separation between the collection of energy states that are filled by electrons (below Fermi level) and the additional "conduction" states that are empty and available for electrons to hop into (above Fermi level). The Fermi level E_F in a metal lies within the conduction band, whereas in a semiconductor it lies within the band gap Eg between valence and conduction bands. In a semi-metal the valence and conduction bands touch at a point – the Fermi point. The axis **kx** and **ky** define the vectors in reciprocal space [93].

Two-Dimensional Graphite

Graphite is a three-dimensional (3D) layered hexagonal lattice of carbon atoms. A single layer of graphite, forms a two-dimensional (2D) material, called 2D graphite or a graphene layer, Even in 3D graphite, the interaction between two adjacent layers is small compared with intra-layer interactions, since the layerlayer separation of 3.35 Å is much larger than nearest-neighbor distance between two carbon atoms, $a_{c-c} = 1.42$Å. Thus the electronic structure of 2D graphite is a first approximation of that for 3D graphite [93].

Figure 12 shows (a) the unit cell and (b) the Brillouin zone of two dimensional graphite as a dotted rhombus and shaded hexagon, respectively, where $\vec{a_1}$ and $\vec{a_2}$, are unit vectors in real space, and $\vec{b_1}$ and $\vec{b_2}$ are reciprocal lattice vectors. In the x, y coordinates shown in the Figure 12, the real space unit vectors $\vec{a_1}$ and $\vec{a_2}$ of the hexagonal lattice are expressed as

$$\vec{a_1} = \left(\frac{\sqrt{3}}{2}a, \quad \frac{a}{2} \right), \quad \vec{a_2} = \left(\frac{\sqrt{3}}{2}a, - \frac{a}{2} \right) \quad (7)$$

Where $a = |\vec{a_1}| = |\vec{a_2}| = 1.42 \times \sqrt{3} = 2.46$Å is the lattice constant of two dimensional graphite. Correspondingly the unit vectors $\vec{b_1}$ and $\vec{b_2}$ of

the reciprocal lattice vectors are given by

$$\vec{b_1} = \left(\frac{2\pi}{\sqrt{3}a}, \quad \frac{2\pi}{a}\right), \quad \vec{b_2} = \left(\frac{2\pi}{\sqrt{3}a}, -\frac{2\pi}{a}\right) \quad (8)$$

corresponding to a lattice constant of $4\pi/\sqrt{3a}$ in reciprocal space. The direction

of the unit vectors $\vec{b_1}$ and $\vec{b_2}$ of the reciprocal hexagonal lattice are rotated by

$90°$ from the unit vectors $\vec{a_1}$ and $\vec{a_2}$ of the hexagonal lattice in real space, as

shown in Figure 12. By selecting the first Brillouin zone as the shaded hexagon

shown in Figure 12 (b), the highest symmetry is obtained for the Brillouin zone of

2D graphite. Here we define the three high symmetry points, of 2D graphite. Here

we define the three high symmetry points, Γ, K and M as the centre the corner,

and the center of the edge, respectively. The energy dispersion relations are

calculated for the triangle $\Gamma K M$ shown by the dotted lines in Figure 12(b).
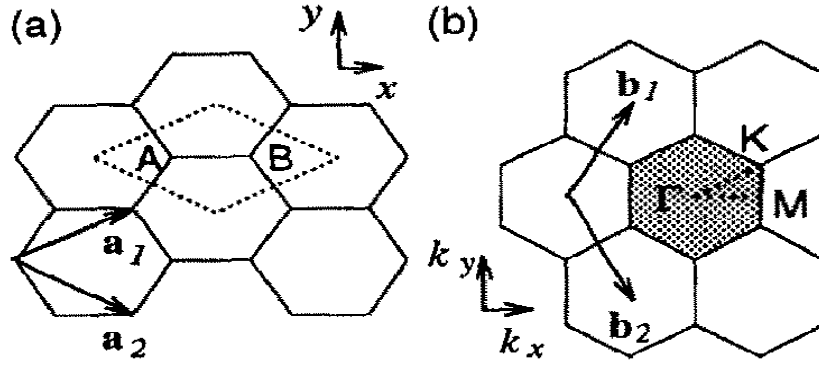
Figure 12: (a) The unit cell and (b) Brillouin zone of two dimensional graphite are shown as the dotted rhombus and the shade_d hexagon, respectively. $\vec{a_i}$, and $\vec{b_i}$, $(i = 1, 2)$ are unit vectors and reciprocal lattice vectors, respectively. Energy dispersion relations are obtained along the perimeter of the dotted triangle connecting the high symmetry points, Γ, K and M [39].
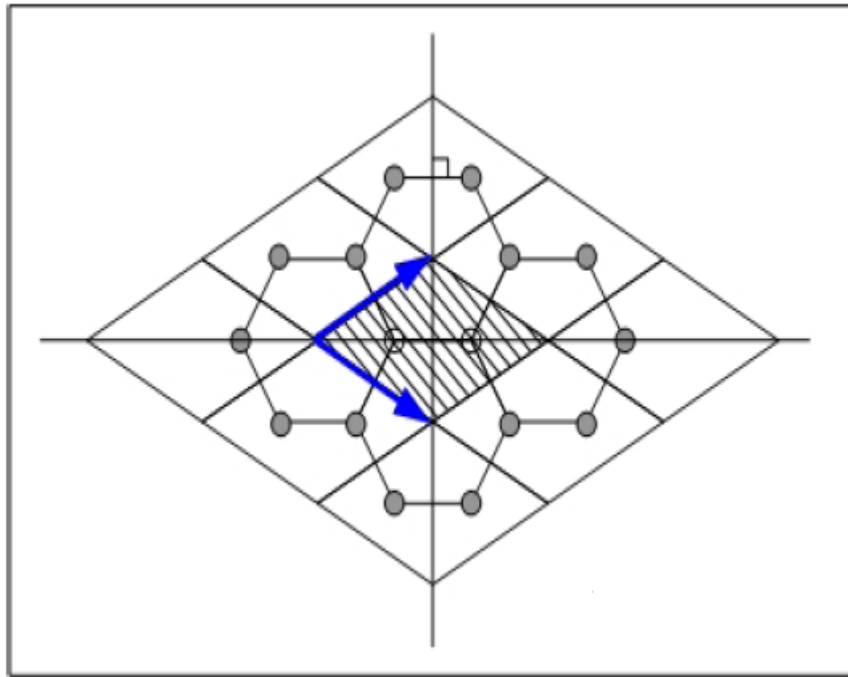
Figure 13: Unit Cell of Graphene containing 2 atoms/unit cell and unit vectors a_1 and a_2 in two equivalent zigzag directions [39].

π bands of graphene

Before we are able to find the energy dispersion relation of the nanotube, we need the energy dispersion relation of the graphene sheet. To determine the energy band structure of nanotubes, it is convenient to start by calculating the energy band structure of a graphite sheet by the tight-binding approximation [94, 95] and then to superimpose the periodic boundary conditions of nanotubes along the circumferential direction. In order to characterize the binding within the basal planes, a "tight-binding approximation" is used. With this approximation, the electronic structure is calculated by separating the interaction within each basal planes (covalent) from in-plane interactions (van der Waals). Such a

35

separation is justified due to the weak interaction that exists between graphene sheets.

The unit cell in real space of graphene contains two carbon atoms as shown in Figure 12 (a). Each carbon atom in the graphene sheet has four valence electrons. The first three electrons form a strong sp^2 σ-bond with its three nearest neighbours which are in the same plane with angles of 120^0 and are at energies - 2.5 eV which lie far below the Fermi level and do not contribute to the electrical conduction.The fourth valence electron, however, is located in the π orbital which lobes is perpendicular to the plane of the graphene sheet, which is slighlty below the Fermi Level; therefore, this electron is predicted to control electrical conduction and transport properties. This corresponds to the valence band of the energy diagram. The anti-bonding π orbital (π* orbital) is slightly above the Fermi level, which corresponds to the conduction band in an energy diagram shown in Figure 14. Hence, the electronic properties of graphene and carbon nanotubes are well described taking into account the energy dispersion of the π-electrons only.

Figure 14: Energy band structure of the graphene layer [39].

Using two crystal Bloch functions φ_A and φ_B, (constructed from atomic orbitals for the in equivalent carbon atoms at A and B in Figure (14)) as the basis functions, the nearest neighbour tight binding energy dispersion relation is obtained from[95] as,

$$E_{g2D}(\mathbf{K}) = \frac{\epsilon_{2p} \pm \gamma_0 \omega(\mathbf{K})}{1 \pm s\omega(\mathbf{K})} \qquad (9)$$

where the + signs in the numerator and denominator go together to define the bonding π energy band, the $-$ signs in the numerator and denominator give the anti-bonding π^*band. Also,

$$\omega(\mathbf{K}) = \sqrt{1 + 4cos\frac{\sqrt{3}\kappa_x a}{2}cos\frac{\kappa_y a}{2} + 4cos^2\frac{\kappa_y a}{2}} \qquad (10)$$

$$\epsilon_{2p} = H_{AA} = H_{BB} = \frac{1}{N}\sum_{R_A}\langle\varphi_A(r - R_A)|H|\varphi_A(r - R_A)\rangle$$

$$\gamma_0 = \langle\varphi_A(r - R_A)|H|\varphi_A(r - R_A - R_i)\rangle \qquad (i = 1, 2, 3)$$

$$s = \langle\varphi_A(r - R_A)\varphi_B(r - R_A - R_i)\rangle \qquad (i = 1, 2, 3)$$

R_A is the position of carbon atom A, R_i is the vector pointing from atom A to its three nearest neighbours. Reich et al. [99] have shown that the nearest-neighbour tight binding approximation for the dispersion of the π and π^* electronic bands in graphene and CNTs applies to only a very limited range of wave vectors, and that interaction with more distant neighbours qualitatively improves the tight binding approximation for the dispersion of the electronic bands.

The energy dispersion relation for the π -electrons of the graphene sheet can be calculated in a tight-binding approximation yielding a bonding (-) and anti-bonding (+) energy band given by

$$E(k_x, k_y) = \pm\gamma_0\left[1 + 4\cos\left(\frac{\sqrt{3}k_x a}{2}\right)\cos\left(\frac{k_y a}{2}\right) + 4\cos^2\left(\frac{k_y a}{2}\right)\right]^{\frac{1}{2}} \qquad (11)$$

where $\gamma_0 \approx 3.0\text{eV}$ is the energy overlap integral between nearest neighbours and a = 0.246nm is the in − plane lattice constant. This equation yields two bands resulting from bonding and anti-bonding states between the two atoms in the unit cell. Figure 15 shows a three-dimensional plot of the energy dispersion $E(kx; ky)$, as follows from Eq. (11).

The conduction and valence bands touch and are degenerate at six K points; these six points define the vertices of the first Brillouin zone, as shown in Figure 15 (b). That is the vanishing energy gap at six points coincides with the

corners of the hexagonal Brillouin zone. The Fermi surface is thus reduced to six points, two of which, the *K* and *K'* points, are inequivalent, where the conduction and valence bands meet or where the anti-bonding and bonding bands touch .

At 0K, the lower bonding bands are completely filled and the upper bands are empty, so graphite is classified as a zero-gap semiconductor.

Conduction

(a)   (b)
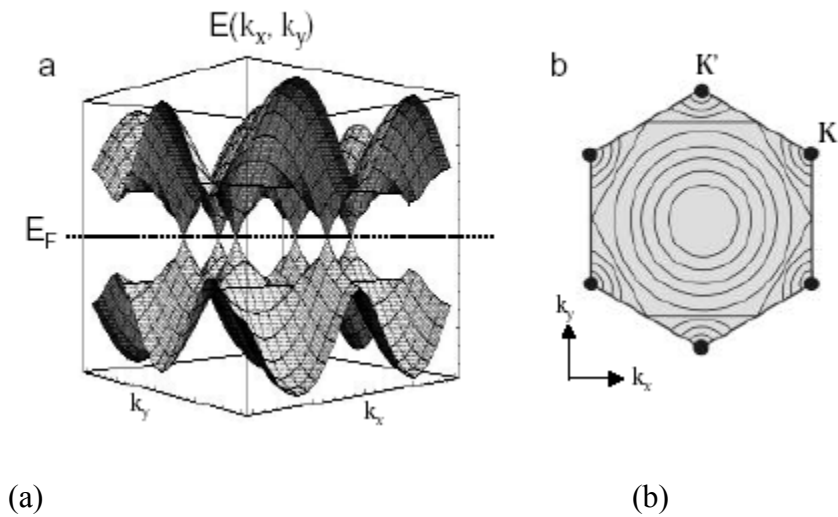
Valance

Figure 15: Energy dispersion for graphite. (a) A three-dimensional graph of the energy E(kx, ky) of valence and conduction states in graphene plotted as a function of wavevector k. (b) The hexagonal Brillouin zone of graphene with energy contours schematically drawn for the bonding band. The Fermi level is reduced to the six corner points, indicated by black dots [39].

The π and π^* bands touch at the K points. Because there are two electrons in the unit cell, the π band (valence band) is completely filled and π^* band

(conducting band) is empty. The valence and conduction states meet at singular points in k-space called K points. Dispersion around these points is conical. The Fermi energy E_F is reduced to six points where the bonding and antibonding bands touch.

Energy contours for the bonding band are drawn in the first Brillouin zone in Figure 15 (b). The antibonding band is similar. Also indicated are the gapless Fermi points at the corners by black dots. Two of these are in equivalent, K and K'; the others can be obtained by lattice transformations along $\boldsymbol{b_1}$ and $\boldsymbol{b_2}$. The energy dispersion in the vicinity of these points is approximately radially symmetric within the **kx, ky** plane.

$$E\text{-}E_F = \frac{\sqrt{3}}{2} a\, \gamma_o \left| k - k_F \right| \tag{12}$$

Energy dispersion for 2D graphene where π and π^* bands touch at the K points and the hexagonal Brillouin zone of 2D graphene is illustrated in Figure 16
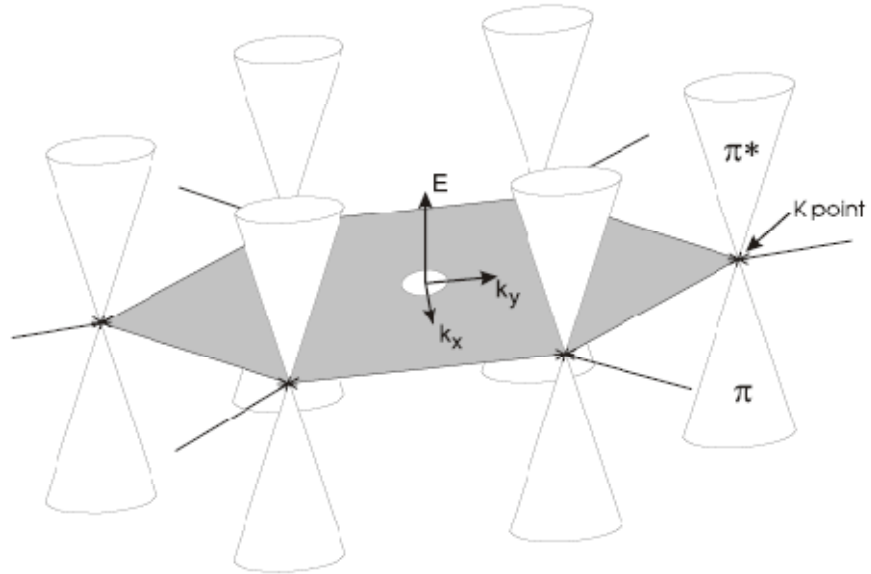
Figure 16: Three dimensional plot of the graphene band structure near E$_F$. The cones represent the π and π* bands touching in the corners of the hexagonal Brillouin zone. and the black dots called K-point are zero-gap points [96].

Figure 16 shows the electronic bands near the Fermi level, i.e. parts of the π and π* bands. The bands touch at the corners of the Brillouin zone and form 'cones' above and below the Fermi level.

$$E(k) = E_F \pm \hbar.\text{vF}.|\, k - kF \,| \qquad\qquad (13)$$

where *kF* is the momentum at a K point and vF = |v(k)| = |$\hbar^{-1}$ dE/dk| ≈ 10^6 m/s. This description holds for a range of several hundred meV around the Fermi level [97]. The states at the K points can be visualized very easily.

In Figure 17 the six momenta belonging to the K points are retransferred into the real lattice. They correspond to a motion along the 'zig-zag' directions in the graphene lattice. This is reasonable, as the zig-zag directions offer the most direct path for current transport if transport is imagined as moving an electron from bond to bond.

        (a)   **(b)**
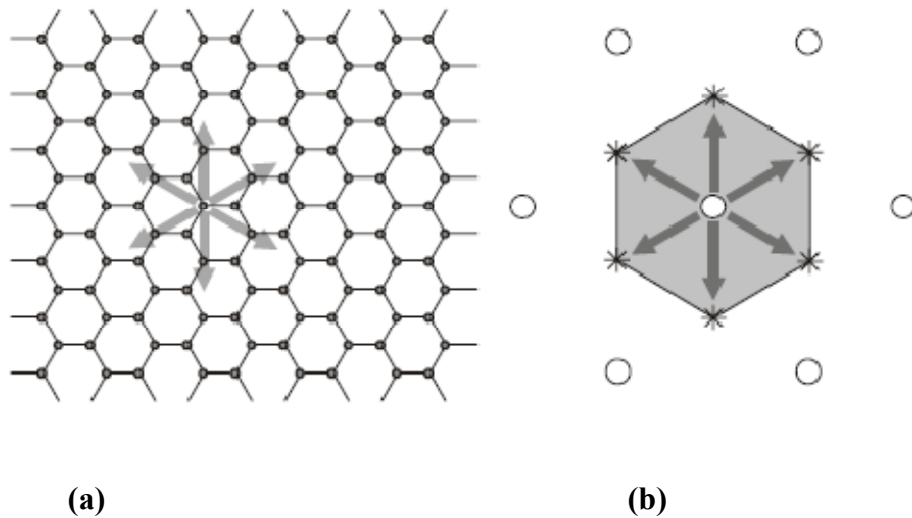
Figure 17: The momenta of the K points in the reciprocal lattice (right hand side) correspond to a motion along the 'zig-zag' directions in the graphene sheet (left hand side) [39].

Wave Vector (k)
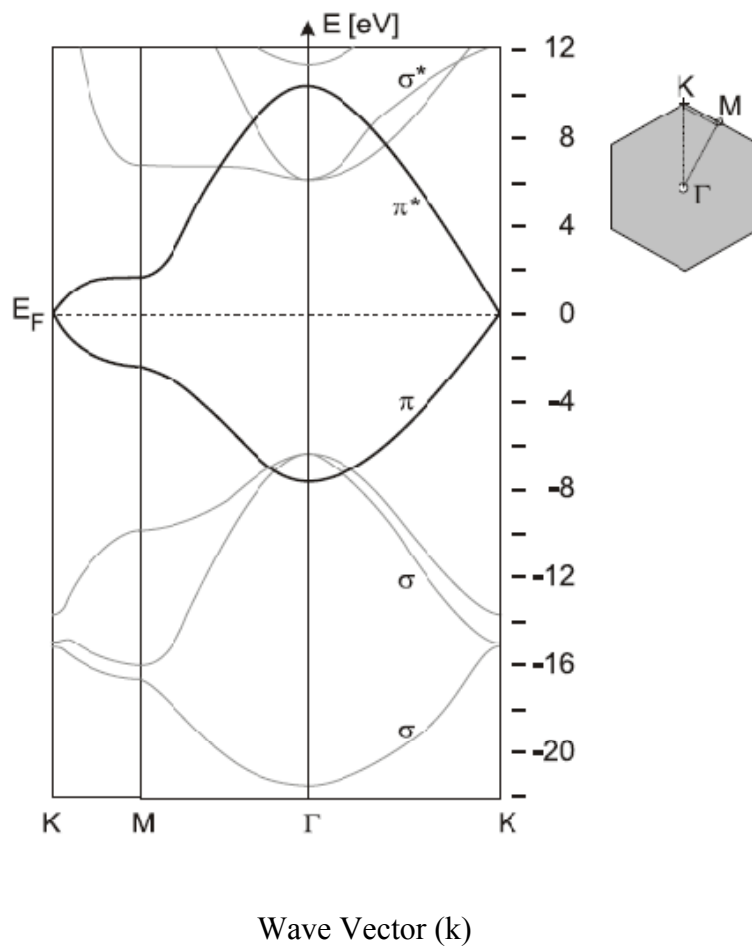
Figure 18: Band structure of graphene along several lines in the Brillouin zone [39].

The σ and σ* bands are derived from the sp^2 hybrid orbitals forming the in-plane bonds. The π and π* bands (emphasized) result from the delocalized p orbitals. Since every carbon atom supplies one electron in its p orbital, the bonding π band is completely filled, while the antibonding π* band is completely empty. These electronic bands touch each other at the K point, that is in the

corners of the Brillouin zone, and thus the Fermi level is pinned there, making graphene a zero gap semiconductor.
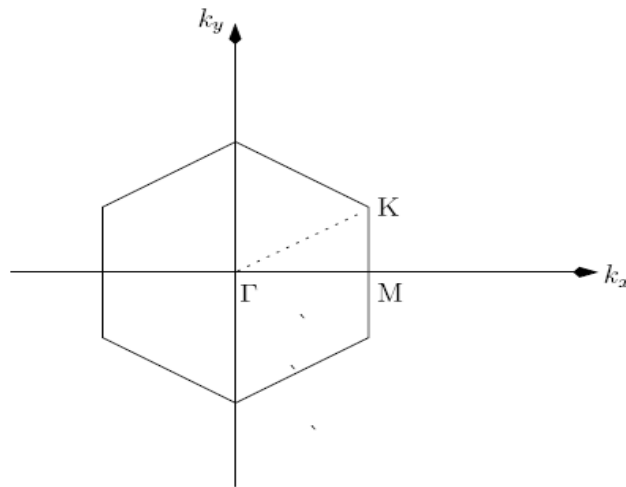
Figure 19: Sketch of Γ, M, and K which are points of high symmetry in the First Brillouin zone of 2D graphite [39].

 Unit Cell of Carbon Nanotube

The first thing we have to do is to choose our primitive lattice vectors $\boldsymbol{a}_1$ and $\boldsymbol{a}_2$ of the graphene sheet (as indicated in Figure 7). These vectors define a parallelogram, which is called the primitive unit cell, and fill all space by the repetition of suitable crystal translations operations. So we can always make sure that we have chosen the right ones. There are many ways of choosing the lattice vectors, but some are more comfortable to work with than others. In Figure 2.5, we have chosen $\boldsymbol{a}_1$ and $\boldsymbol{a}_2$ to be two secants of an isosceles triangle within two hexagons . In Cartesian coordinates (x, y) basis [39], the lattice vectors are

$$a_1 = (\frac{\sqrt{3}a}{2}, \frac{a}{2}) \quad , \quad a_2 = (\frac{\sqrt{3}a}{2}, -\frac{a}{2}) \qquad (14)$$

where a is lattice constant given by $a = \sqrt{3}\, a_{c\text{-}c}$ and with $a_{c\text{-}c}$ denoting the nearest neighbour distance, $a_{c\text{-}c} = 1.42$ Å . Hence the value of a is given by

$a = |a_1| = |a_2| = 2.46$ Å

Another choice could be with an angle of 120 degrees instead of our 60 degrees. The two lattice vectors are now used to determine the roll up vector (also called the Chiral vector) given by

$$C_h = na_1 + ma_2 \qquad (15)$$

which determines the circumference of the carbon nanotube. Here n and m are the indices of the tube and for that reason it is obvious that ($n.m$) directly describes the size of the tube. Translation vector, T, describes the distance between two similar lattice points. Now, the two vectors C_h and T span a rectangle, which is called the 2D unrolled nanotube unit cell depicts various fundamental parameters of a CNT, and their relationships to graphene.

This is the rectangle, we roll up in the Chiral vector direction that forms the cylinder (see Figure 7). The side OB is put together with the side AB' .This define a CNT unit cell, that repeatedly put together forms the tube. The nanotube just created has no distortion of bond angles other than in the circumference direction, caused by the cylindrical curvature of the surface. This curvature, the chiral angle θ, the diameter $d_t = C_h/\pi$ and an applied magnetic field along the tubule axes have influence of the electrical properties of the tube. The unit cell of the nanotube is

therefore defined as the rectangle formed by Chiral vector, Ch, and the one-dimensional translational vector ,T, as shown in Figure 7.

Reciprocal Lattice

Reciprocal space is also called Fourier space, k- space, or momentum space. In contrast to real space or direct space, the reciprocal space lattice is a set of imaginary points constructed in such a way that the direction of a vector from one point to another coincides with the direction of a normal to the real space planes and the separation of those points (absolute value of the vector) is equal to the reciprocal of the real interplanar distance. We are to find the lattice vectors in the reciprocal space given the real space lattice vectors. All calculations are done in Cartesian coordinates. The first Brillouin zone is found by Wigner-Zeits primitive unit cell [89]. In the following this zone is referred to as the Brillouin zone. The derivation of the reciprocal lattice vectors are first given generally. This approach is chosen because more than one set of reciprocal lattice vectors are to be calculated and the choice of real space lattice vectors is ambiguous.

The general equation can be applied to the different kinds of real space lattice vectors connected with the carbon nanotube. The general relationship between a direct lattice vector, and reciprocal lattice vector is given by [90]:

$$\boldsymbol{a}_i \bullet \boldsymbol{b}_j = 2\pi\delta_{ij} \qquad (16)$$

Where the a's are the basis vectors of the real or direct lattice. The b's are then

called the fundamental vectors of the reciprocal lattice. Here δ_{ij} is the well known

Kronecker delta function defined by [91]:

$$\delta_{ij} = \begin{cases} 1 & if \quad i = j \\ 0 & if \quad i \neq j \end{cases} \qquad (17)$$
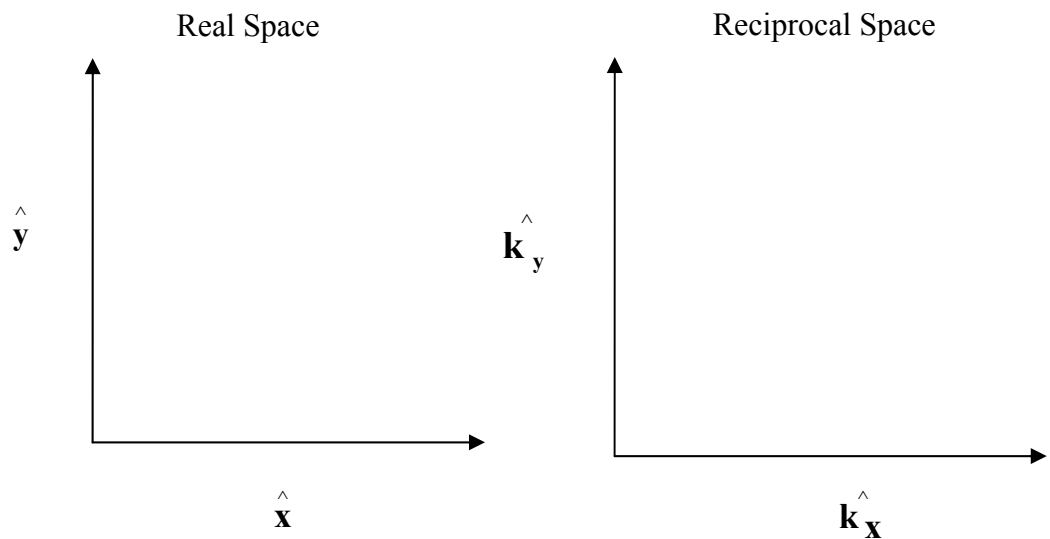
Figure 20: Real space with unit vectors $(\hat{x}, \hat{y})$ and reciprocal space with unit vectors $(\hat{k}_x, \hat{k}_y)$ of length 2π [92].

Figure 20 shows how the unit vectors of the two-dimensional Cartesian

coordinate system in real space which transform to the unit vectors in the

reciprocal space according to equation (16). The $\hat{x}$ unit vector is perpendicular to

$\hat{k}_y$ and vice versa. The unit lengths of the reciprocal vectors are 2π (not shown at

Figure 20). If the two real space vectors are not perpendicular, it is not possible to do the transformation to reciprocal space. In a three dimensional lattice with real space vectors a_1, a_2 and a_3, the reciprocal lattice vectors are found by

$$b_1 = 2\pi \frac{a_2 \times a_3}{\text{Vreal}}, b_2 = 2\pi \frac{a_3 \times a_1}{\text{Vreal}}, b_3 = 2\pi \frac{a_1 \times a_2}{\text{Vreal}} \qquad (18)$$

Where Vreal $= a_1 \bullet a_2 \times a_3$ is the volume of the box spanned by a_1, a_2 and a_3.

These vectors obey equation (16). The length of a reciprocal lattice vector is given by

$$\left| b_i \right| = \frac{2\pi}{\left| a_i \right|} \qquad (19)$$

where i is 1, 2 or 3. In our case we are only in two dimensions.

This equation is only correct in special case where it is later used. $a_3 = (0,0,1)$ and a_1 **is** perpendicular to a_2 in the plane orthogonal to a_3

$$a_1 = \begin{pmatrix} a_{1x} \\ a_{1y} \\ 0 \end{pmatrix}, \, a_2 = \begin{pmatrix} a_{2x} \\ a_{2y} \\ 0 \end{pmatrix}, a_3 = \begin{pmatrix} 0 \\ 0 \\ 1 \end{pmatrix}$$

The reciprocal lattice vectors of the plane are b_1 and b_2

The volume spanned by the real space vectors are

$$V_{real} = \begin{pmatrix} a_{1x} \\ a_{1y} \\ 0 \end{pmatrix} \bullet \left[\begin{pmatrix} a_{2x} \\ a_{2y} \\ 0 \end{pmatrix} \times \begin{pmatrix} 0 \\ 0 \\ 1 \end{pmatrix} \right] = \begin{pmatrix} a_{1x} \\ a_{1y} \\ 0 \end{pmatrix} \bullet \begin{pmatrix} a_{2y} \\ -a_{2x} \\ 0 \end{pmatrix}$$

$$= a_{1x} a_{2y} - a_{1y} a_{2x}$$

Using equation (17) one gets the reciprocal vectors

48

$$b_1 = \frac{2\pi}{a_{1x}a_{2y} - a_{1y}a_{2x}} \begin{pmatrix} a_{2y} \\ -a_{2x} \\ 0 \end{pmatrix} \qquad (20)$$

$$b_2 = \frac{2\pi}{a_{1x}a_{2y} - a_{1y}a_{2x}} \begin{pmatrix} -a_{1y} \\ a_{1x} \\ 0 \end{pmatrix} \qquad (21)$$

The vector b_3 is not calculated, because it is irrelevant to our purpose. We are only working in two dimensions. Now for any choice of real space lattice vectors, the reciprocal lattice vectors can be calculated easily by equation (20) and (21). The Brillouin zone is obtained by finding Wigner-Zeits primitive cell. The above equations of the reciprocal lattice vectors are used to find the Brillouin zone of a general nanotube. In this derivation actually three Brillouin zones are in play.

These three are

       i.The 2D Brillouin zone of the graphene sheet (as discussed earlier)

       ii. The 2D Brillouin zone of the nanotube unit cell

       iii. The 1D Brillouin zone of the nanotube

It is very important to distinguish these three zones.

The (i) is found by the real space lattice vectors of the graphene sheet (a_1, a_2), equations (20) and (21). The same procedure is used in the (ii) case, but now with the real space lattice vectors defining the nanotube (**Ch, T**). Both cases give a two dimensional Brillouin zone. The (iii) Brillouin zone is a result of the boundary condition, which arises when the graphene is made to a tube. By using the zonefolding technique the dimension of the 2D

Brillouin zone of the nanotube unit cell reduces to 1D Brillouin zone of the nanotube.

The 2D Brillouin Zone of the Nanotube Unit Cell

If chiral vector Ch and translation vector T define a CNT real unit cell in 2-D (Figure 7), then we may similarly assign two associated reciprocal vectors K_1 and K_2 respectively. The corresponding reciprocal lattice vectors K_1 (in the circumferential direction) and K_2 (along the direction of the nanotube axis) are calculated by the expression (16) which gives;

$$Ch \cdot K_1 = 2\pi \quad T \cdot K_1 = 0$$

$$Ch \cdot K_2 = 0 \quad T \cdot K_2 = 2\pi \tag{22}$$

Simple vector algebra gives:

$$K1 = (-t2b1 + t1b2)/N \ and \ K2 = (mb1 - nb2)/N \tag{23}$$

where N denotes the number of hexagons in SWCNT unit cell

$$N = (n^2 + nm + m^2)/dR \tag{24}$$

Where $t1$ and $t2$ are integers. Because of the translational symmetry of T, wave vectors in the direction of K_2 are continuous for an infinitely long nanotube. In the circumferential direction there are N wave vectors iK_1 ($i = 0,1. . .$ N -1), which means N discrete k vectors. Thus K_1 and K_2 define a CNT reciprocal unit cell in 2-D. The length of the reciprocal vectors K_1 and K_2 are respectively $2\pi/Ch$ and $2\pi/T$ from (19) it is also clear from the expressions of K_1 and K_2 that the larger the CNT unit cell, the smaller the 2-D reciprocal unit-cell. The transition from the 2D graphene to the 1D SCWNT results in a reduction of real and reciprocal space.
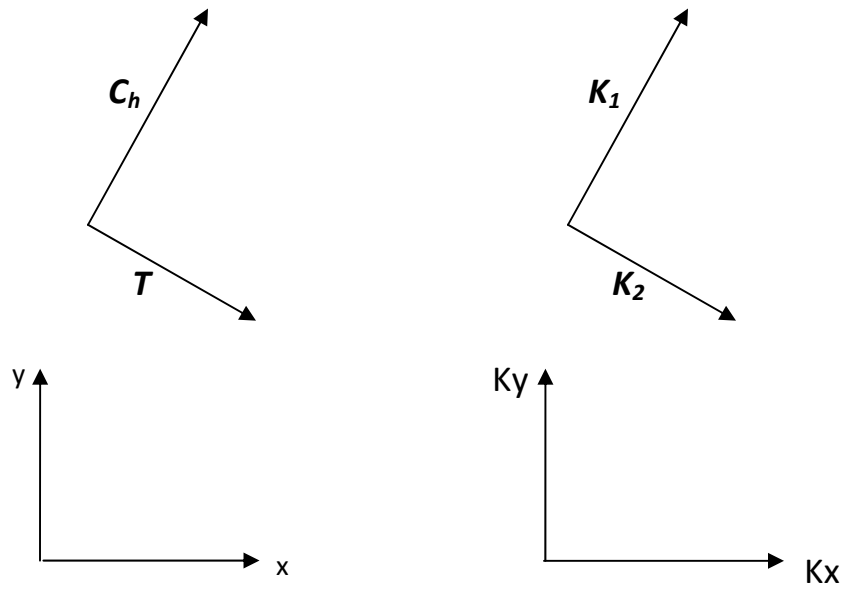
Figure 21: The real space vectors defining the nanotube (left) and the reciprocal vectors defining the 2D Brillouin zone of the nanotube unit cell (right) [92].

In Figure 21, the four vectors are shown. Here in the case of an unspecified chiral tube, the reciprocal lattice vectors of the nanotube unit cell in Cartesian coordinates are given by equation (20) and (21). The Brillouin zone depicted in Figure 21 (the rectangle) has the area spanned by the two reciprocal lattice vectors. The larger the area of the nanotube unit cell gets the smaller the area of the Brillouin becomes, because the reciprocal vectors are proportional to the reciprocal length of the unit vectors. In the chiral case even for small values of n and m, the area of the real space nanotube unit cell becomes large and thereby reducing the 2D Brillouin of the nanotube unit cell.

Boundary Condition

When the nanotube 2D unit cell is folded to a cylinder only a discrete set of wave-vectors along the reciprocal vector K_1 in the reciprocal space are allowed. This results in a number of quantization lines in the reciprocal space which represent the allowed pairs of (kx, ky).The condition on kx and ky is dependent on the choice of real space lattice vectors and the choice of coordinate system. Hence we first derive it generally. The expression derived can then be used with another choice than ours. The periodic boundary condition is a result of the required periodicity along the circumference of the Block wavefunction express as

$$\psi(x + \mathbf{Ch}) = \psi(x) \tag{25}$$

where $\psi(x)$ is the block wave function of the graphene sheet and x is along the circumference. This gives rise to the following equation

$$\mathbf{C}_h \bullet \mathbf{k} = 2\pi i \tag{26}$$

where $\mathbf{C}_h = n\mathbf{a}_1 + m\mathbf{a}_2$ is the chiral vector defining the nanotube, $\mathbf{k}$ the wavevector and i an integer. Restrictions are later made on i. We write the relation in Cartesian coordinates to express the dependence between k_x and k_y.

$$\left(n\begin{pmatrix} a_{1x} \\ a_{1y} \end{pmatrix} + m\begin{pmatrix} a_{2x} \\ a_{2y} \end{pmatrix} \right) \bullet \begin{pmatrix} k_x \\ k_y \end{pmatrix} = 2\pi i$$

$$(na_{1x} + ma_{2x})k_x + (na_{1y} + ma_{2y})k_y = 2\pi i \tag{27}$$

The last equation shows a linear dependence between k_x and k_y and gives the pairs of (k_x, k_y), which are allowed in the reciprocal space. When the tube is made only a subset of wave vectors in k-space are allowed.

Because of the linear dependence we speak about quantization lines. Using the defined real space lattice vectors $\boldsymbol{a}_1$ and $\boldsymbol{a}_2$ (14) the relation becomes

$$(n\frac{\sqrt{3}a}{2} + m\frac{\sqrt{3}a}{2})k_y = 2\pi i - (n\frac{a}{2} + m\{-\frac{a}{2}\})k_x$$

$$(n+m)k_y = \frac{4\pi i}{\sqrt{3}a} - \frac{n-m}{\sqrt{3}}k_x \tag{28}$$

$$k_y = \frac{4\pi i}{\sqrt{3}a(n+m)} - \frac{n-m}{\sqrt{3}(n+m)}k_x \tag{29}$$

Equation (28) expresses the boundary condition and is true for all n and m. Two particular simple cases appear for $n = m$ (armchair nanotube) and $n = -m$ (zig-zag nanotube).

In the armchair case the quantization condition is $k_y = \frac{4\pi i}{\sqrt{3}a(n+n)} = \frac{2\pi i}{\sqrt{3}an}$ which corresponds to horizontal lines, while the lines are vertical $k_x = \frac{2\pi i}{an}$ in the zigzag case. These two cases are often used as illustrative examples in articles. It is worth a remark that the (n,n) and $(n,-n)$ nanotubes are not in the same symmetry area i.e. between the 30 degrees. It is more obvious to look at the $(n,0)$ zigzag nanotubes, which are equivalent to the $(n,-n)$ tubes, together with the (n,n) armchair nanotubes. They are defining a symmetry area, where all nanotube can be constructed. In the following we will use equation (27) and thus not looking at the case, where $n = -m$.

Two different nanotubes are shown at Figure 22. The dashed lines are the allowed pairs of wavevectors according to the periodic boundary condition and the rectangle is the 2D Brillouin zone of the nanotube unit cell. Only the lines

near the Brillouin zone of the graphene sheet are depicted. The spacing between

the lines is $\dfrac{2\pi}{C_h}$, because the allowed wavevectors $\mathbf{k}$ are the projection on $\mathbf{C}_h$

of length 2π times an integer (16). This is exactly the reciprocal lattice vector $\mathbf{K}_1$.

The edge of the Brillouin zone of the nanotube unit cell parallel to the

quantization lines is half the distance of the vector $\mathbf{K}_1$. The vector $\mathbf{K}_2$ is along the

lines perpendicular to $\mathbf{K}_1$ and defines the edge of the Brillouin zone of the

nanotube unit cell in that direction. The angle between the lines and the kx-axis is

determined by equation (29). In the (9, 0) zigzag case the slope of the lines is

$\dfrac{-1}{\sqrt{3}}$, which is a line with an angle to the k_x-axes of -30 degrees (see left panel

of Figure 22). The (5, 5) armchair has $k_y = \dfrac{2\pi i}{5\sqrt{3}a}$, which is a constant. Thus

the horizontal lines in right panel of Figure 22.

[(9,0) zig-zag]   [(5,5) armchair]
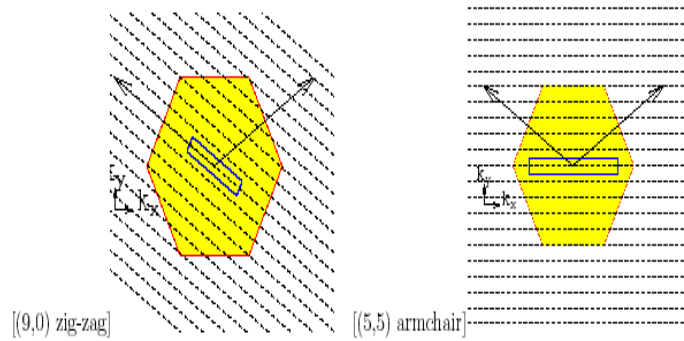
Figure 22: The 2D Brillouin zone of the carbon nanotube unit cell (blue rectangular) compared with the Brillouin zone of the graphene sheet. The dashed lines represent the allowed values of kx and ky. Only one line crosses the Brillouinin zone of the tubes unit cell [84].

The 1D Brillouin Zone of The Nanotube

By using the periodic boundary conditions in the circumferential direction imposed by chiral vector C_h (see Figure 7), the wave vector K_1 associated with the C_h direction becomes quantized in a CNT, while the wave vector K_2 associated with the direction of the translational vector T along the nanotube axis remains continuous for a nanotube of infinite length.

The quantization conditions imposed on the circumference vector give a quantization of the reciprocal vector $iK1$ (i = 0, 1,..,N-1). The momentum vector along the tube length $K2$ is continuous in the range of ($-\pi/T$, π/T) for an infinitely long nanotube. This gives rise to a set of k vectors that are parallel to T. These k vectors will result in cross-sections of the graphene electron dispersion.

These cross sections result in the appearance of various subbands in a CNT. The band structure is obtained along the $K2$ vector. Figure 23 (a) shows the reciprocal lattice vectors, K_1 and K_2, for a Ch = (4,2) chiral nanotube. The wavevectors of a carbon nanotube are indicated by the parallel lines since K_1 is discrete and K_2 is continuous. The length of all the parallel lines is $2\pi/T$ which is the length of the one-dimensional first Brillouin zone. Thus, the set of one dimensional (1D) energy dispersion relations of a carbon nanotube is made up of slices of the 2D energy band structure of graphite.

Figure 23(a) shows the reciprocal lattice structure of 2D graphite, and how the carbon nanotube fits into that structure.
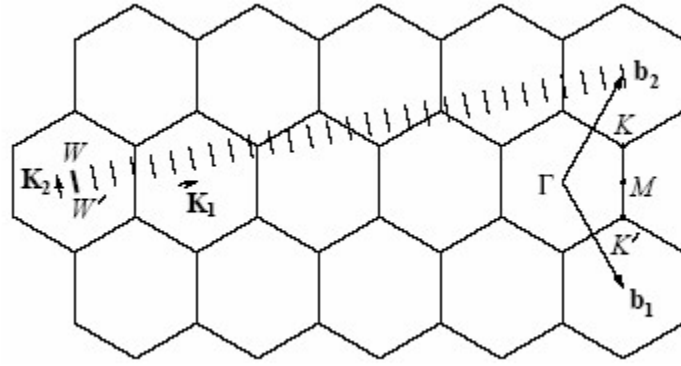
Figure 23(a): The reciprocal lattice vectors, K_1 and K_2, for a C_h=(4,2) chiral nanotube [39].

The vectors K_1 and K_2 are reciprocal lattice vectors corresponding to $\mathbf{C_h}$ and $\mathbf{T}$, respectively. The line segment WW', which is parallel to $\mathbf{K_2}$, represents the Brillouin zone of the nanotube. The figure corresponds to C_h = (4, 2), T = (4, -5), K_1 = (5$\mathbf{b_1}$ + 4$\mathbf{b_2}$)/28, K_2 = (4$\mathbf{b_1}$-2$\mathbf{b_2}$)/28 [39].

In this figure, the each hexagon represents a Brillouin zone of 2D graphite. The Brillouin zone represents a line of reciprocal vector **K2**. The first, and some of the extended Brillouin zones of the nanotube are shown in figure 23(a).

The reciprocal lattice vectors of the 2D graphite are $\mathbf{b_1}$ and $\mathbf{b_2}$,while **K1** and **K2** are the reciprocal nanotube lattice vectors corresponding to $\mathbf{C_h}$ and $\mathbf{k}$, respectively. The line segment WW' represents the first Brillouin zone of a carbon nanotube. Points Γ, M, K, and K' are points of high symmetry in the Brillouin zone of 2D graphite. This figure shows the nature of the quantization of the wave vectors of a carbon nanotube in the form of a series of parallel Brillouin zones. Total number of Brillouin zones equals number of hexagons in tube's unit

cell. Hence the transition from the 2D graphene to the 1D SWCNT results in a reduction of real and reciprocal space. This N distinct wave -vectors result in N pairs of 1D energy dispersion relations for the carbon nanotube.
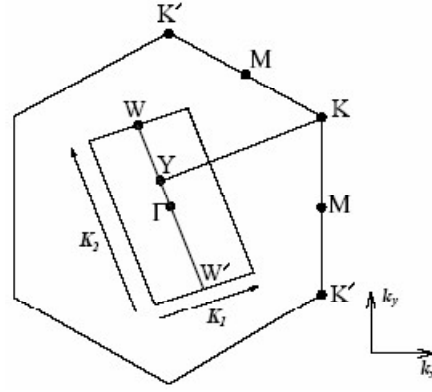
Figure 23 (b): The condition for metallic energy bands: if the ratio of the length of the vector YK to that of K_1 is an integer, metallic energy bands are obtained [39].

Figure 23 (b) illustrates the condition for obtaining metallic versus semiconducting CNTs. The condition for obtaining a metallic energy band is that the ratio of the length of the vector *YK* to that of K_1 (in Figure 23(b)) is an integer [39]. In general, the vector *YK* is given by

$$YK = \frac{(2n+m)\,K_1}{3} \qquad (30)$$

If the vector *YK* **is** an integer multiple of vector *K1*, we will have a CNT band line intersecting the graphene *K* point. This is because, in the extended zone scheme, CNT band lines are spaced |*K1*| apart. However a case in which *YK* is a non-integer multiple of *K1* does not correspond to a CNT band line, and the CNT

will be semiconducting. That is, if none of the Brillouin zones are passing through the K points of graphene inverse lattice unit cell, thus the tube is semiconducting. The condition for metallic nanotubes is that ($2n +m$) or equivalently ($n-m$) is a multiple of 3. In particular, the armchair nanotubes denoted by (n, n) are always metallic, and the zigzag nanotubes ($n, 0$) are only metallic when n is a multiple of 3.

Energy Dispersion Relation of the 1D Nanotube

The folding of the graphene layer to form a CNT introduces an additional level of quantization due to the confinement of electrons around the circumference of the nanotube. The component of the wave-vector **k** is constrained by imposing the periodic boundary or quantization condition $C_h.k=2\pi i$ (i = 0, 1, 2…) along the circumferential direction as shown in equation (2.21). Thus, in going from a 2D graphene sheet to a 1D CNT, each graphene band is split into a number of 1D subbands indexed by i. The number of available energy modes in the circumferential direction is quantized. The electrons are only free to move in an axial direction. This quantization along the circumferential direction gives rise to discrete numbers of parallel equidistant lines in the direction of the tube axis , representing the allowed k modes in the reciprocal space of the graphene.

i=-2   i=0   i=2
i=-3 i=-1   i=1   i=3
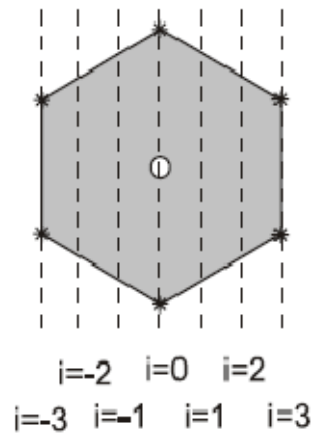
Figure 24: The dashed lines cutting through the Brillouin zone in the reciprocal lattice mark the momenta which are allowed states in the nanotube according to quantization condition (2.21) [96].

In Figure 24, the situation is visualized. The dashed lines mark the momenta which satisfy the quantization condition and are thus allowed states in this special nanotube. The only degree of freedom for the electronic momentum left is along the tube axis. The momentum around the circumference is quantized.
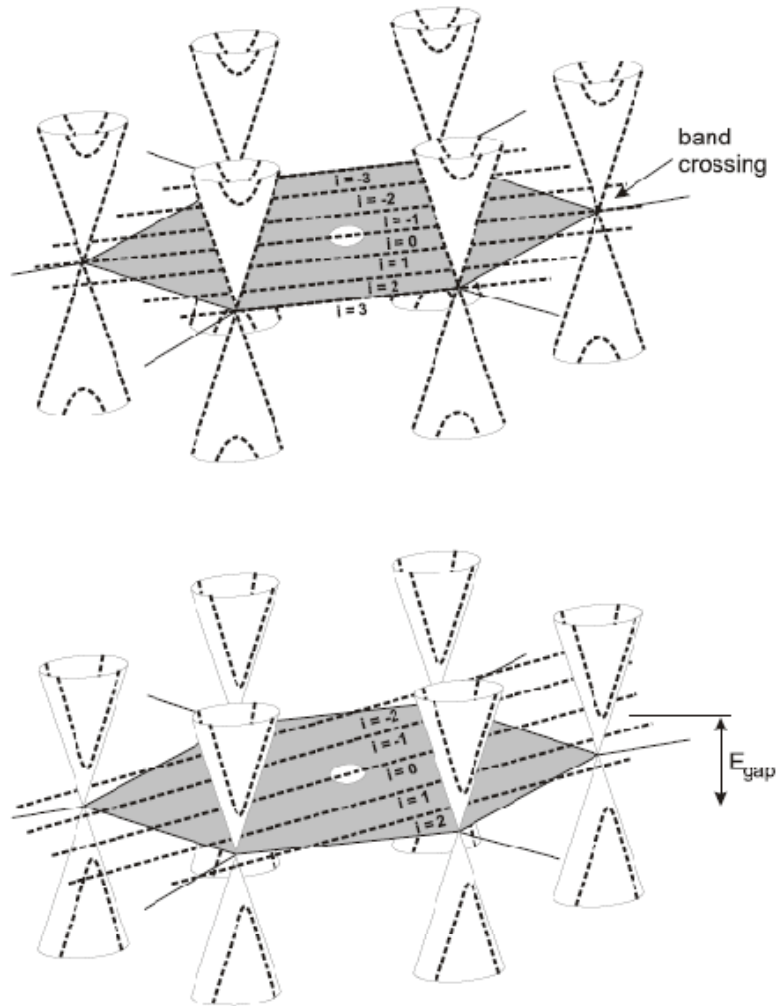
Figure 25: Three dimensional plot of the graphene band structure near E$_F$, together with the quantization condition marked by dashed lines in the Brillouin zone [96].

The resulting subbands in the π and π* bands (cones) are marked by the dotted lines. The upper figure shows a situation , where the K points are included in one of the quantization lines (i=0 and i=±3),hence the belonging subbands are touching (or crossing) at the Fermi level and the tube is metallic. In the lower

figure, the quantization lines miss the K points and a finite energy gap between the subbands results [96].

Figure 25 shows how the quantization condition results in semiconducting and metallic tubes when applied to the graphene band structure. If the quantization lines include the K points, the tube is metallic (i.e. there are allowed states at the Fermi level), while if the quantization misses these points, an energy gap between the subbands results. As can be seen, the closer the quantization is to the K points, the smaller the energy gap will be. When the diameter of the tube is increased, the interval between quantization lines for different subbands i shrinks and the lines draw closer to the K points, so the gap decreases. Using the quantization condition (11), one can compute how close (or how far) the K points are missed by the subbands. For a metallic tube, this distance is zero, at least for one subband-K point combination.

For the semiconducting tubes the minimum distance between a subband and a K point turns out to be

$$\delta k = \frac{1}{3} \cdot \frac{2\pi}{|\mathbf{C}_h|} = \frac{1}{3} \cdot \Delta k \tag{31}$$

where Δk is the separation of the quantization lines in the reciprocal space (see Figure 26).
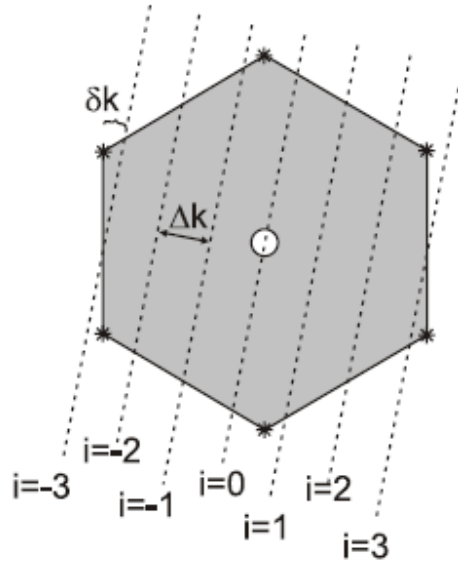
Figure 26: The quantization lines in the reciprocal lattice are spaced by

$\Delta k = 2\pi/|C_h|$ and miss the K points by at least $\delta k = 1/3.\Delta k$ [96].

Due to the linear dispersion relation around the K points, the energy gap for the semiconducting tubes turns out to be

$$E\text{gap} = 2\,\hbar\,v_F\,\delta k = \frac{2}{3}\,\hbar\,v_F\frac{2\pi}{|C_h|} = \frac{4}{3}\frac{\hbar}{d}\,v_F \qquad (32)$$

The gap energy scales inversely with the diameter d of the tube. Figure 26 visualizes the dependence of the gap energy on the tube diameter.
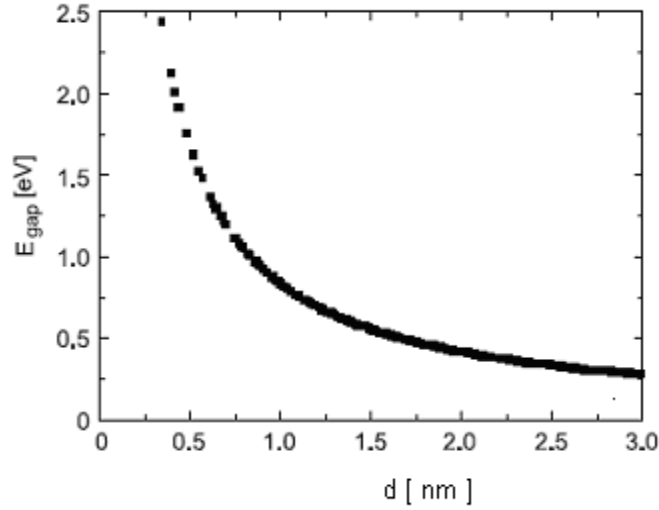
Figure 27: Gap energies for tubes of different diameters. One third of the tubes is metallic (the ones fulfilling n-m = 3i), hence they have zero energy gap. The gaps of the other two thirds of the tubes decrease with increasing diameter according to equation 2.9 [39].

Each quantization line corresponds to a one-dimensional channel for conduction along the nanotube. In the case of an armchair nanotube the quantization condition is n $\sqrt{3}k_x a$ = $2\pi i$ (i = 0; 1; 2… n) and the allowed k-lines run in the (vertical) $\mathbf{k_y}$ direction. For zigzag nanotubes the condition $nk_y a = 2\pi i$ (i = 0; 1; 2… n) applies and the allowed k-lines are in the (horizontal) $\mathbf{k_x}$ direction. The dispersion relations for armchair and zigzag nanotubes can be obtained by inserting these quantization conditions in Eq. (11), to yield

$$E_{armchair}(k_y) = \pm\gamma_0 \left[1 + 4\cos\left(\frac{\pi i}{n}\right)\cos\left(\frac{k_y a}{2}\right) + 4\cos^2\left(\frac{k_y a}{2}\right)\right]^{\frac{1}{2}} \qquad (33)$$

$$E_{zigzag}(k_x) = \pm\gamma_0 \left[1 + 4\cos\left(\frac{\sqrt{3}k_x a}{2}\right)\cos\left(\frac{\pi i}{n}\right) + 4\cos^2\left(\frac{\pi i}{n}\right) \right]^{\frac{1}{2}} \quad (34)$$

where $a = \sqrt{3}a_{c\text{-}c}$ is the lattice constant.

Band structures of typical metallic and semiconducting carbon nanotubes, which have similar diameters of ~1.3 nm are plotted in Figure 28 (a) and (b).
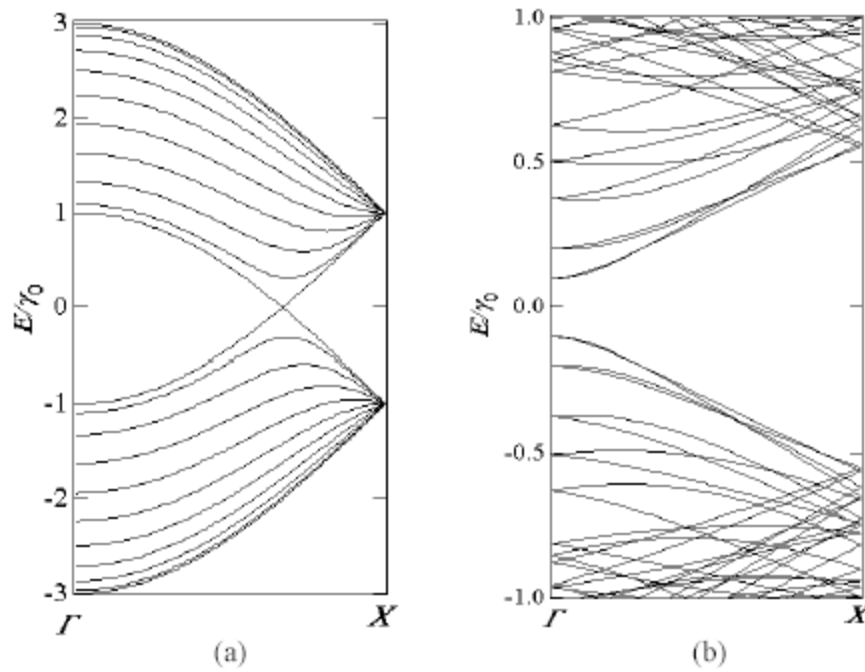
Figure 28: The band structure of (a) a typical metallic nanotube with chirality of (10, 10) and (b) a typical semiconducting nanotube with chirality of (14, 7) [39].

Density of States (DOS)

The 1D density of states (DOS) in units of (states/C-atom)/eV is calculated by

$$\text{D}(E) = \frac{T}{2\pi N} \sum_{\pm} \sum_{i=1}^{N} \int \frac{1}{\left| \dfrac{dE_i^{\pm}(k)}{dk} \right|} \delta(E_i^{\pm}(k) - E) dE \qquad (35)$$

where the summation is taken for the N conduction (+) and valence (−) 1D bands. T is the magnitude of the translation vector $\boldsymbol{T}$ shown in figure 2.1 and $E_i^{\pm}(k)$ is the 1D energy dispersion relations of a CNT. Since the energy dispersion near the Fermi energy is linear [98]. The density of states of metallic nanotubes is constant at the Fermi energy and is inversely proportional to the diameter of the tube.

$$D(E_F) = \frac{a}{2\pi^2 \gamma_0 dt} \qquad (36)$$

It is clear from (35) that the density of states becomes infinity at the points where the energy dispersion relation becomes flat as a function of k. One dimensional van Hove singularities (vHs) appear in the density of states, which are known to be proportional to $(E^2 - E_0^2)^{-1/2}$ at both the energy minima and maxima $(\pm E_0)$ of the dispersion relations for carbon nanotubes. These are important for determining many solid state properties of carbon nanotubes, such as the spectroscopy studies of SWCNTs with scanning tunneling microscope and optical absorption.

The DOS of typical metallic nanotube (10, 10) and semiconducting nanotube (14, 7) can be numerically calculated this way as clearly shown in

Figure 29 (a) and (b) respectively as well as the van Hove singularities. The vHs is the first peaks will tell us the magnitude of the bandgap for the semi-conducting tubes. The differences between the highest-lying valence band singularity and the lowest-lying conduction-band singularity in the 1D electronic density of states have been calculated by Mintmire and White [99], and White and Todorov [100] and are given by.

$$E_{11}^{M}(d_t) = 6a_{c-c}\gamma_0 / d_t \text{ and } E_{11}^{S}(d_t) = 2a_{c-c}\gamma_0 / d_t \qquad (37)$$

where the superscript M and S denotes metallic and semiconducting, respectively. Around a K point, the energy gap approximately has a linear dependence on $k = |\boldsymbol{k}|$ measured from K point. Within the small k approximation, we can derive the energy difference of the first pair of van Hove singularities in the 1-dimensional DOS for metallic and semiconducting nanotubes as shown in (29).
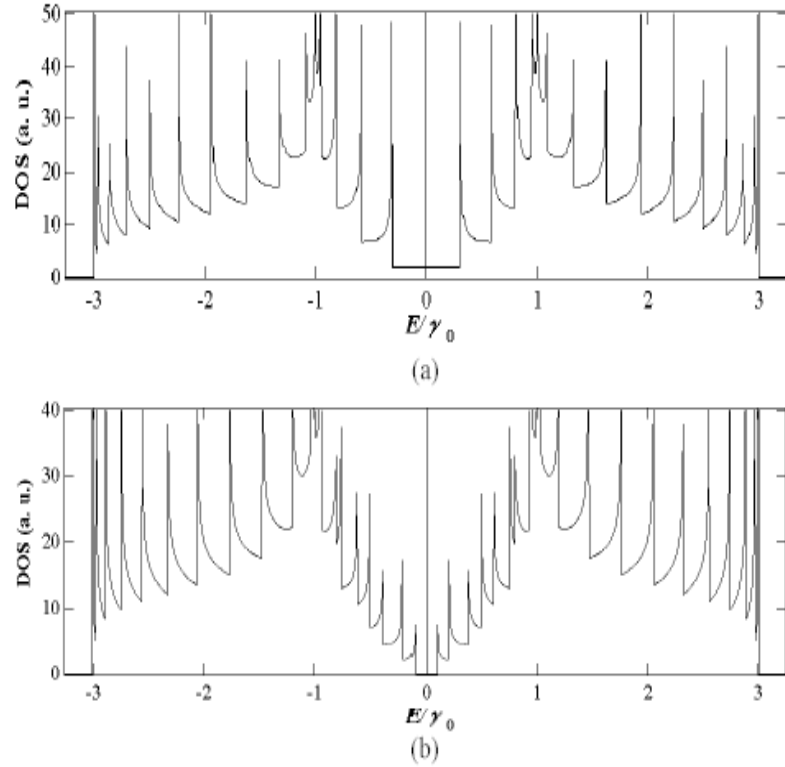
Figure 29: The density of states for (a) typical metallic nantube (10, 10) (b) typical semiconducting nanotube (14, 7).

Note that for the semiconducting nanotube, the gap between the first pair of van Hove singularities is half of that of the metallic nanotube, which has a similar diameter. For the semiconducting tube the DOS is zero at the Fermi level. For all nanotubes, vHs arise at each band edge due to the low dimensionality of the material [101].

Top figure of Figure 30 for kx; ky > 0 shows two normalized energy dispersion diagrams plotted as E/γ_0 against k that follow from Eqs. (33) and (34) for a (5, 5) and a (10, 0) nanotube and the density of states corresponding to metallic and semiconducting nanotubes respectively
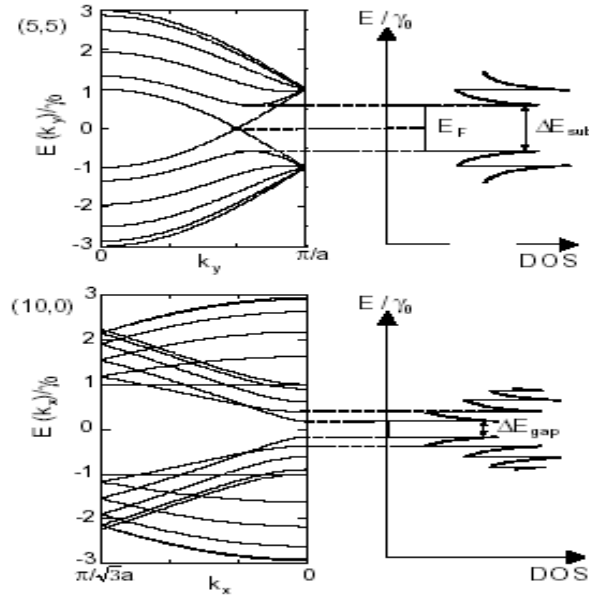
Figure 30: The energy band diagram (left) and density of states (right) for a metallic (top) and a semiconducting (bottom) nanotube [39].

The energy dispersion diagrams are Calculated with Eqs. (14) and (15) for a (5,5) and (10,0) nanotube respectively. The energy is divided by the energy overlap integral $\gamma_o \approx 3.0$ eV. In the density of states (DOS) diagrams a series of sharp peaks appear which are the subband onsets. The energy differences between the first two singularities near the Fermi level are indicated for the metallic and the semiconducting case by ΔEsub and ΔEgap respectively [39].

The top figure of Figure 31 schematically shows the density of states (DOS) that can be derived from the energy dispersion diagrams shown in the left figure. The linear crossing energy bands near the Fermi level yield a small constant DOS for the armchair nanotube. At energies away from the Fermi energy, the next subbands lead to Van Hove singularities at the onset due to the one-dimensional nature of the subbands. The energy separation between the first

singularities above and below the Fermi level is here defined as ΔEsub. The DOS

for a semiconducting nanotube also consists of a series of sharp Van Hove

singularities. In this case however, there is an energy gap ΔEgap. For chiral

nanotubes, the unit cell **T** x **C$_h$** is typically an order of magnitude larger than for

nonchiral nanotubes. It has been argued that a large number of subbands and

therefore also many singularities in the DOS may be expected [102]. However, it

has been found that near the Fermi level a universal DOS exists that scales with

diameter and depends, to first order, only on the metallic or semiconducting

character of a nanotube [91, 99]. The DOS for a chiral nanotube with the same

diameter is therefore similar to that of a zigzag or and armchair nanotube.
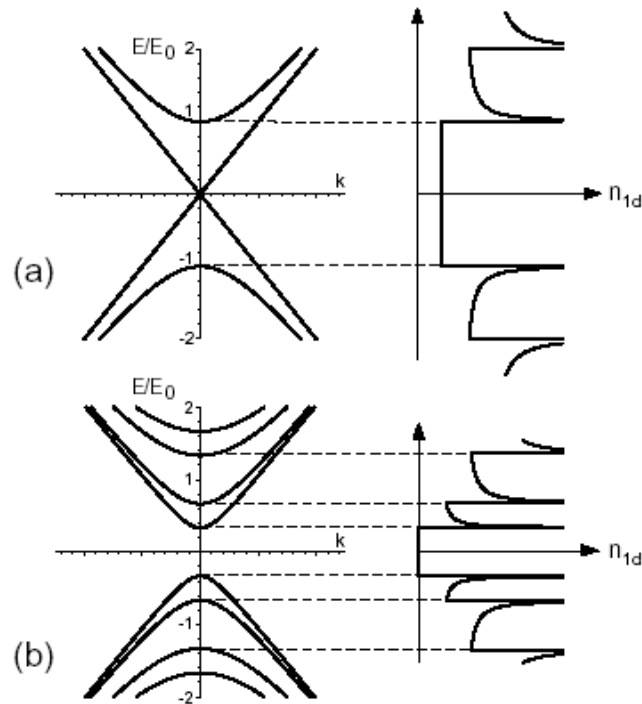
Figure 31: Approximate one-dimensional energy dispersion of carbon nanotubes (left) and corresponding density-of-states (right) [39].
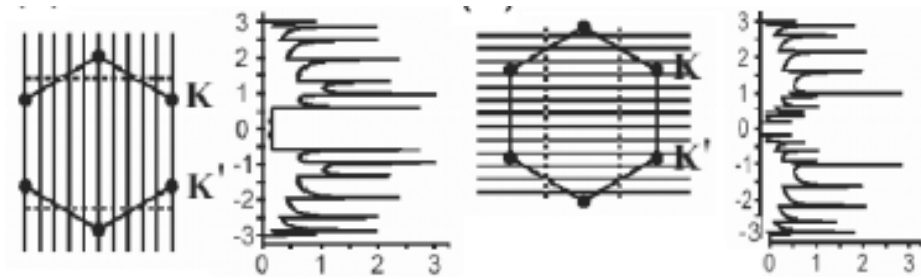
Figure 32: Allowed 1D states as cuts of the graphene Brillouin zone for (a) a (5,5) Armchair metallic and (b) a (5,0) Zigzag semiconducting nanotube, along with their associated density of states (DOS) [39].

There are two kinds of nanotubes: metallic and semiconducting one . A tube is metallic, if 2n +m is a multiple of three.
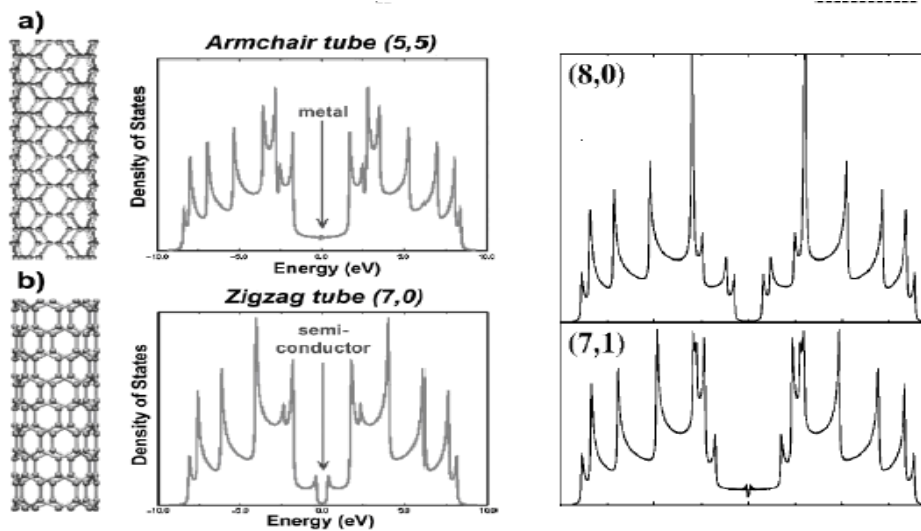
Figure 33: The DOS for metallic and semiconducting nanotubes using the tight binding k-space approach [39].

In Figure 33, Density of states (DOS) exhibiting the valence (negative values), the conduction band (positive values) and the Fermi energy (centered at 0eV) for (a) a metallic armchair (5, 5) tube, which shows electronic states at the Fermi energy (characteristic of a metal); (b) a zigzag tube (7, 0) revealing semiconducting behaviour caused by the energy gap located between the valence and conduction band (characteristic of semiconductors).

The (8, 0) zigzag tube is a large-gap semiconductor, the (7, 1) chiral tube has a tiny gap and will behave as a metal at room temperature. The spikes shown in the DOS of the tubules are called Van Hove singularities and are the result of the one dimensional quantum conduction, which is not present in an infinite graphite crystal. We see that the density of states near the Fermi level E_F (located at $E = 0$) is different for metallic and semiconducting nanotubes. The density of states at E_F has a value of zero for semiconducting nanotubes, but is non-zero (and small) for metallic nanotubes. The condition for a (n,m) carbon nanotube to be metallic is that *m- n* be a multiple of three [103]. An equivalent condition is that *2n + m* be a multiple of three [39]. Thus, a carbon nanotube can be either metallic or semiconducting, depending on its diameter and its chiral angle. Also of great interest are the singularities in the 1D density of states, corresponding to extrema in the *E*(k) relations.
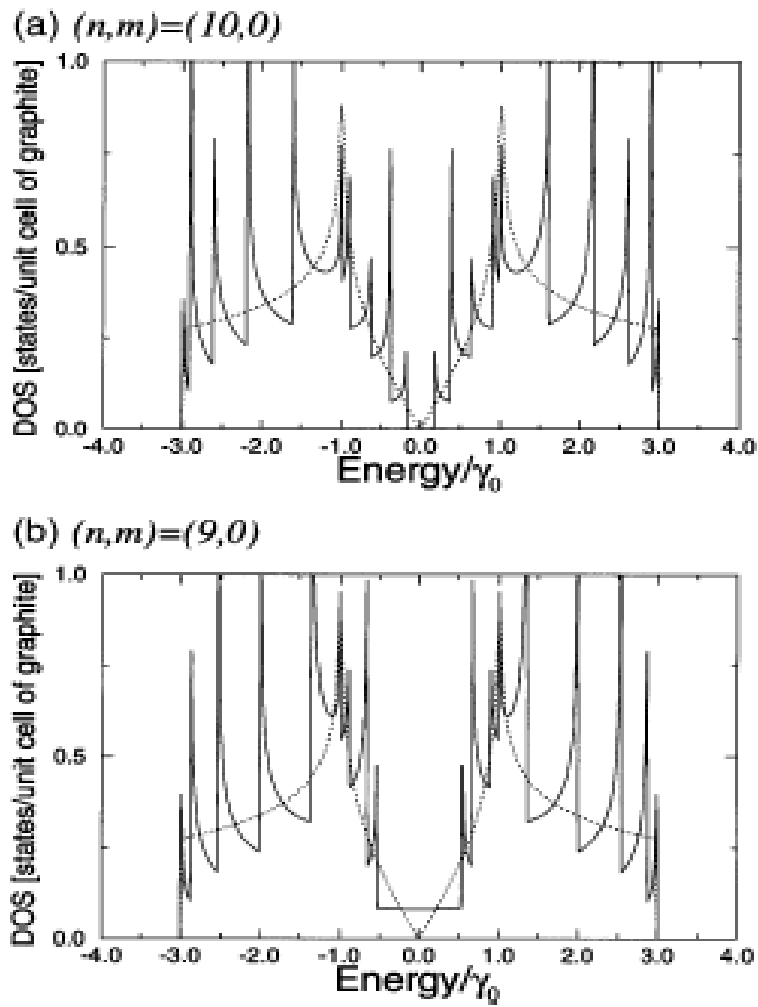
Figure 34: Electronic 1D density of states per unit cell of a 2D graphene sheet for two (n,0) zigzag nanotubes: (a) The (10,0) nanotube which has semiconducting behavior, and (b) the (9,0) nanotube which has metallic behavior. Also shown in the figure is the density of states for a 2D graphene sheet (dotted curve) [103].

Due to large length-to-diameter ratio for the nanotubes, the electron motion is normally confined to the tube axis, and therefore, for small diameter

nanotubes, the one-dimensional (1D) density of electronic states exhibits sharp

singularities below and above the Fermi level E_F as shown in Figure 34.

CHAPTER THREE

MATHEMATICAL MODEL OF CURRENT DENSITY

Nonlinear Electron Transport Effects in Carbon Nanotubes

This section explores theoretically, the electron transport effects in CNs. The Boltzmann kinetic equation is solved in the framework of momentum–independent relaxation time. The calculation is done using the semiclassical approach which provides us with the simplest route to this theory, supplying somewhat rough but quite tractable analytical results. We consider a CN simultaneously exposed to a constant (dc) and high-frequency (ac) electromagnetic fields. An analytical expression for the current density in a nanotube is derived. We show that different kinds of pump fields can suppress the formation of high-electric current instability inside the CN while still preserve a broadband THz gain. The reasons given in [55] why high-order harmonic generation by CNs are of interest include the possibility to use this process as a mechanism for the generation of coherent ultrashort light pulses at very short wavelengths because of the strong electronic nonlinearity in CNs. Another, it is possible to generate radiation with very short wavelengths in a device confined to a very small, sub-mm region and lastly, the spectra of the harmonics are of great interest for the potential applications in providing useful information on the dynamics of electron motion in CNs.

The results of these calculations are analysed in chapter 4, using MATLAB.

Phenomenological Model of a Nanotube

We consider an undoped single-wall zigzag (n, 0) or armchair (n, n) carbon nanotubes (CNs) exposed simultaneously to (i) constant (dc) using mono- and polychromatic fields and (ii) coherent electromagnetic waves with commensurate frequencies of $\omega_1 = \Omega$ and $\omega_2 = 2\Omega$. The investigation is done within the semiclassical approximation in which the motion of π-electrons are considered as classical motion of free quasi-particles in the field of crystalline lattice with dispersion law extracted from the quantum theory. Taking into account the hexagonal crystalline structure of a rolled graphene in a form of CNs and using the tight binding approximation, the energy is expressed as [43].

$$\varepsilon\left(s\Delta p_\varphi, p_z\right) \equiv \varepsilon_s(p_z)$$

$$= \pm\gamma_0\left[1 + 4cos(ap_z)cos\left(\frac{a}{\sqrt{3}}s\Delta p_\varphi\right) + 4cos^2\left(\frac{a}{\sqrt{3}}s\Delta p_\varphi\right)\right]^{1/2} \quad (38)$$

for zigzag CNs and

$$\varepsilon\left(s\Delta p_\varphi, p_z\right) \equiv \varepsilon_s(p_z)$$

$$= \pm\gamma_0\left[1 + 4cos(as\Delta p_\varphi)cos\left(\frac{a}{\sqrt{3}}p_z\right) + 4cos^2\left(\frac{a}{\sqrt{3}}p_z\right)\right]^{1/2} \quad (39)$$

for armchair CNs.

Where $\gamma_0 \sim 3.0eV$ is the overlapping integral, p_z is the axial component of quasimomentum, Δp_φ is transverse quasimomentum level spacing and s is an integer. The expression for a in Eqs. (38) and (39) is given as $a = 3b/2\hbar$,

$b = 0.142nm$ is the C-C bond length. The $-$ and $+$ signs correspond to the valence and conduction bands respectively. Due to the transverse quantization of the quasi-momentum, its transverse component can take n discrete values, $p_\varphi = s\Delta\,p_\varphi = \pi\sqrt{3}/an\ (s = 1\dots,n)$. Unlike transverse quasimomentum p_φ, the axial quasimomentum p_z is assumed to vary continuously within the range $0 \le p_z \le 2\pi/a$, which corresponds to the model of infinitely long $CN(L = \infty)$. This model is applicable to the case under consideration because of the restriction to the temperatures and /or voltages well above the level spacing [104], ie. $k_BT > \varepsilon_C,\ \Delta\varepsilon$, where k_B is Boltzmann constant, T is the temperature, ε_C is the charging energy. The energy level spacing $\Delta\varepsilon$ is given by $\Delta\varepsilon = \pi\hbar v_F/L$), where v_F is the Fermi velocity and L is the carbon nanotube length [105].

Assuming the high-order harmonic fields to be sufficiently weak, we neglect the role of high-order harmonics in the electron dynamics. We also neglect the transverse current on the CN surface, considering the axial current to be predominant. In that case we can presume the propagation of high order harmonics to be normal to the CN's axis, i.e., along the x axis. Then, neglecting the spatial dispersion in the charge carrier motion, we can describe this motion by the Boltzmann equation in the form as follows [43]:

$$\frac{\partial f(p,t)}{\partial t} + eE(t)\frac{\partial f(p)}{\partial P} = -\frac{[f(p) - f_0(p)]}{\tau} \qquad (40)$$

Where e is the electron charge, $f_0(p)$ is the equilibrium distribution function, $f(p,t)$ is the distribution function, and τ is the relaxation time. The electric field $E(t)$ is applied along CNTs axis. In this problem the relaxation term τ is assumed to be constant. The justification for τ being constant can be found in

[105]. The relaxation term of Eq. (40) describes the effects of the dominant type of scattering (e.g. electron-phonon and electron-twistons) [104, 106, 107]. For the electron scattering by twistons (thermally activated twist deformations of the tube lattice), τ is proportional to m and the $I - V$ characteristics have shown that scattering by twistons increases E^{max} and decreases $|\partial j_z / \partial E_z|$ in the NDC region; the lesser m, the stronger this effect. Quantitative changes of the $I - V$ curves turn out to be insignificant in comparison with the case of $\tau = $ const [106, 107, 108, 109, 110, 111].

Solution of Boltzmann Equation

Expanding the distribution functions of interest in Fourier series as

$$f_0(p) = \Delta p_\varphi \sum_{s=1}^{n} \delta(p_\varphi - s\Delta p_\varphi) \sum_{r \neq 0} f_{rs} \, e^{iarp_z} \qquad (41)$$

and

$$f(p,t) = \Delta p_\varphi \sum_{s=1}^{n} \delta(p_\varphi - s\Delta p_\varphi) \sum_{r \neq 0} f_{rs} \, e^{iarp_z} \emptyset_\upsilon(t) \qquad (42)$$

for zigzag CNs

$$f_0(p) = \Delta p_\varphi \sum_{s=1}^{n} \delta(p_\varphi - s\Delta p_\varphi) \sum_{r \neq 0} f_{rs} \, e^{ibrp_z} \qquad (43)$$

and

$$f(p,t) = \Delta p_\varphi \sum_{s=1}^{n} \delta(p_\varphi - s\Delta p_\varphi) \sum_{r \neq 0} f_{rs} \, e^{ibrp_z} \emptyset_\upsilon(t) \qquad (44)$$

for armchair CNs. Where $b = a/\sqrt{3}$.

Here the energy unit i.e $\hbar = 1$ has been used. $\delta(x)$ is the Dirac delta function, f_{rs} is the coefficient of the Fourier series and $\emptyset_\upsilon(t)$ is the factor by which the Fourier transform of the nonequilibrium distribution function differs from its equilibrium distribution counterpart.

$$f_{rs} = \frac{a}{2\pi\Delta p_\varphi S} \int_0^{\frac{2\pi}{a}} \frac{e^{-iarp_z}}{1 + exp(\varepsilon_s(p_z)/k_B T)} dp_z \qquad (45)$$

for zigzag CNs and

$$f_{rs} = \frac{a}{2\pi\Delta p_\varphi S} \int_0^{\frac{2\pi}{a}} \frac{e^{-ibrp_z}}{1 + exp(\varepsilon_s(p_z)/k_B T)} dp_z \qquad (46)$$

for armchair CNs.

Substituting Eqs. (41) and (42) into Eq. (40) and solving with $E(t) = E_o + E_1 cos\omega t$ we obtain,

$$\emptyset_\upsilon(t) = \sum_{k=-\infty}^{\infty} \sum_{m=-\infty}^{\infty} \frac{J_k(r\beta)J_{k-\upsilon}(r\beta)}{1 + i(earE_0 + k\omega)\tau} exp(i\upsilon\omega t) \qquad (47)$$

where $\beta = \frac{eaE_1}{\omega}$, $J_k(\beta)$ is the Bessel function of the kth order and $\Omega = eaE_0$ (for details see appendix B).

Current Density

To obtain the current density we expand $\varepsilon_s(p_z)/\gamma_0$ in Fourier series with coefficients ε_{rs}

$$\frac{\varepsilon_s(p_{s,}s\Delta p_\varphi)}{\gamma_0} = \varepsilon_s(p_z) = \sum_{r\neq 0} \varepsilon_{rs} e^{iearp_z} \quad (48)$$

Where

$$\varepsilon_{rs} = \frac{a}{2\pi\gamma_0} \int_0^{\frac{2\pi}{a}} \varepsilon_s(p_z) e^{-iearp_z} \, dp_z \quad (49)$$

and expressed the velocity as

$$v_z(p_z, s\Delta p_\varphi) = \frac{\partial \varepsilon_s(p_z)}{\partial p_z} = \gamma_0 \sum_{r\neq 0} iar \, \varepsilon_{rs} e^{iearp_z} \quad (50)$$

The surface current density is then defined as

$$j_z = \frac{2e}{(2\pi\hbar)^2} \iint f(p) \, v_z(p) d^2 p,$$

or

$$j_z = \frac{2e}{(2\pi\hbar)^2} \sum_{s=1}^{n} \int_0^{\frac{2\pi}{a}} f\left(p_z, s\Delta p_\varphi, \emptyset_v(t)\right) v_z(p_z, s\Delta p_\varphi) dp_z \quad (51)$$

and the integration is taken over the first Brillouin zone. Substituting Eqs. (42), (47) and (50) into (51) we find the current density for the zigzag CNs after averaging over a period of time t as

$$j_z = \frac{8e\gamma_0}{\sqrt{3}\hbar na} i \sum_{r=1}^{n} r \sum_{s=1}^{n} f_{rs}\varepsilon_{rs} \sum_{k=-\infty}^{\infty} \frac{J_k^2(r\beta)(1-i(\Omega r + k\omega)\tau)}{1+\left((\Omega r + k\omega)\tau\right)^2} \quad (52)$$

Simplifying (52) and considering the real terms we have,

$$j_z = j_o \sum_{r=1}^{\infty} r \sum_{k=-\infty}^{\infty} \frac{J_k^2(r\beta)(\Omega r + k\omega)\tau}{1+\left((\Omega r + k\omega)\tau\right)^2} \sum_{s=1}^{n} f_{rs}\varepsilon_{rs} \quad (53)$$

Where $j_o = \frac{8e\gamma_0}{\sqrt{3}\hbar na}$, $\Omega = eaE_0$ and $\beta = eaE/\omega_1$ for zigzag CNs.

When the electric field amplitudes are small $\beta \ll 1$, we can use the Bessel

function approximation $J_{\pm1}^2 \sim (r^2\beta/2)^2$ and $J_0^2 \sim 1 - \dfrac{r^4\beta^2}{2}$. Hence from Eq. (53)

we obtain,

$$j_z = \frac{8e\gamma_0}{\sqrt{3}\hbar na}\left(\frac{(\Omega r\tau)\beta^2}{2}\right)\sum_{r=1}^{\infty} r^2 \sum_{s=1}^{n} f_{rs}\varepsilon_{rs}$$

$$\times \left(\frac{(1 + (\omega\tau)^2 - (\Omega r\tau)^2)}{\left[1 + ((\Omega r - \omega)\tau)^2\right]\left[1 + ((\Omega r + \omega)\tau)^2\right]}\right) \qquad (54)$$

and the imaginary part

$$j_z = j_o \sum_{r=1}^{\infty} r \sum_{s=1}^{n} f_{rs}\varepsilon_{rs}$$

$$\times \left(\frac{i\omega\tau(1 - 3(\Omega r\tau)^2 + (\omega\tau)^2)}{[1 + (\Omega r\tau)^2]\left[1 + ((\Omega r - \omega)\tau)^2\right]\left[1 + ((\Omega r + \omega)\tau)^2\right]}\right) \qquad (55)$$

Where $j_0 = \dfrac{8e\gamma_0}{\sqrt{3}\hbar na}\left(\dfrac{(\omega\tau)\beta^2}{2}\right)$

(See appendix B for details).

On the other hand when $\omega\tau \leq 1$, Eq. (53) can be re-written in the form of

ref. [37] as;

$$j_z = j_o \sum_{r=1}^{\infty} r \left(\frac{\frac{1}{4}\{[1 + (Z_c + \beta)^2]^{1/2} + [1 + (Z_c - \beta)^2]^{1/2}\}^2 - \beta^2 - 1}{[1 + (Z_c + \beta)^2][[1 + (Z_c - \beta)^2]]}\right)^{1/2}$$

$$\times \sum_{s=1}^{n} f_{rs}\varepsilon_{rs} \qquad (56)$$

Where $j_o = \dfrac{8e\gamma_0}{\sqrt{3}\hbar na_{c-c}}$, $Z_c = eaE_o$ and $\beta = \dfrac{eaE_1}{\omega}$ for zigzag CNs.

Direct Current Generation Due To Wave Mixing in Carbon Nanotubes

Substituting Eqs. (41) and (42) into Eq.(40) and using

$$E(t) = E_1 cos\omega_1 t + E_2 cos(\omega_2 t + \theta) \quad \text{we get}$$

$$\emptyset_\upsilon(t) = \sum_{k_1,k_2 = -\infty}^{\infty} \sum_{\upsilon_1,\upsilon_2 = -\infty}^{\infty} J_{k_1}(r\beta_1)J_{k_2}(r\beta_2)J_{k_1+\upsilon_1}(r\beta_1)J_{k_2+\upsilon_2}(r\beta_2)$$

$$\times \left(\frac{(1 - i(k_1\omega_1 + k_2\omega_2)\tau)}{1 + ((k_1\omega_1 + k_2\omega_2)\tau)^2}\right) \times \{cos(\upsilon_1\omega_1 t + \upsilon_2(\omega_2 t + \theta))$$

$$- isin(\upsilon_1\omega_1 t + \upsilon_2(\omega_2 t + \theta))\} \qquad (57)$$

where $\beta_1 = \frac{eaE_1}{\omega_1}$, $\beta_2 = \frac{eaE_2}{\omega_2}$, and $J_k(\beta)$ is the Bessel function of the kth order.

Substituting Eqs. (42), (50) and (57) into (51) and linearizing with respect

to E_2 using $J_{\pm1}^2 \sim (r^2\beta/2)^2$ and $J_0^2 \sim 1 - \frac{r^4\beta^2}{2}$ and then averaging the result with

respect to time t, we obtain the DC subjected to $\omega_1 = \Omega$ and $\omega_2 = 2\Omega$ as follows;

$$j_z = j_0 E_2 cos\theta \sum_{r=1}^{\infty} r^2 \sum_{k=-\infty}^{\infty} \frac{kJ_k(r\beta_1)J_{k-2}(r\beta_1)}{1 + (k\Omega\tau)^2} \sum_{s=1}^{n} f_{rs}\varepsilon_{rs} \qquad (58)$$

Where $j_o = \frac{2e^2\gamma_0 a}{\sqrt{3}\hbar na}$

See appendix E for details.

Similar expressions are obtained for armchair CNs as follows;

$$j_z = \frac{4 e^2\gamma_0}{\sqrt{3} na\hbar^2} \sum_{r=1}^{\infty} \frac{r^2 E_0\tau}{1 + (\Omega r\tau)^2} \sum_{s=1}^{n} f_{rs}\varepsilon_{rs} \qquad (59)$$

$$j_z = \frac{8e\gamma_0}{3\hbar na} \sum_{r=1}^{\infty} r \sum_{k=-\infty}^{\infty} \frac{J_k^2(r^2\beta)(\Omega r + k\omega)\tau}{1 + ((\Omega r + k\omega)\tau)^2} \qquad (60)$$

$$j_z = \frac{8e\gamma_0}{3\hbar na}\left(\frac{(\Omega r\tau)\beta^2}{2}\right)\sum_{r=1}^{\infty}r^2\sum_{s=1}^{n}f_{rs}\varepsilon_{rs}$$

$$\times\left(\frac{(1+(\omega\tau)^2-(\Omega r\tau)^2)}{\left[1+((\Omega r-\omega)\tau)^2\right]\left[1+((\Omega r+\omega)\tau)^2\right]}\right) \qquad (61)$$

and the imaginary part

$$j_z = \frac{8e\gamma_0}{3\hbar na}\left(\frac{(\omega\tau)\beta^2}{2}\right)\sum_{r=1}^{\infty}r\sum_{s=1}^{n}f_{rs}\varepsilon_{rs}$$

$$\times\left(\frac{i\omega\tau(1-3(\Omega r\tau)^2+(\omega\tau)^2)}{\left[1+(\Omega r\tau)^2\right]\left[1+((\Omega r-\omega)\tau)^2\right]\left[1+((\Omega r+\omega)\tau)^2\right]}\right) \quad (62)$$

$$j_z = \frac{8e\gamma_0}{3\hbar na}\sum_{r=1}^{\infty}r\left(\frac{\frac{1}{4}\{[1+(Z_c+\beta)^2]^{1/2}+[1+(Z_c-\beta)^2]^{1/2}\}^2-\beta^2-1}{[1+(Z_c+\beta)^2][[1+(Z_c-\beta)^2]]}\right)^{1/2}$$

$$\times\sum_{s=1}^{n}f_{rs}\varepsilon_{rs} \qquad (63)$$

$$j_z = \frac{4e^2\gamma_0 a}{3\hbar na}E_2 cos\theta\sum_{r=1}^{\infty}r^2\sum_{k=-\infty}^{\infty}\frac{kJ_k(r\beta_1)J_{k-2}(r\beta_1)}{1+(k\Omega\tau)^2}\sum_{s=1}^{n}f_{rs}\varepsilon_{rs} \quad (64)$$

Where $\Omega = eaE_0/\sqrt{3}$ for armchair carbon nanotubes.

In this work, equations 53, 54, 56 and 58 are the basis for the current density-electric field $(I-V)$ characteristics for zigzag CNs while equations 60, 61, 63 and 64 are the basis for the $I-V$ characteristics for armchair CNs. Following ref [43], we assume that the equations do not take into account both interband transitions and quantum-mechanical corrections to the intraband motion or resonant transitions inherent in the CN lattice. $\Omega < \varpi$ holds true for the first approximation whereas the condition $\Omega < \delta E/\hbar$ must be fulfilled to utilize the second one [43]. In the above inequalities, ϖ is the low-frequency edge of the

optical transition band, and δE is the width of the allowed band. The order- of-magnitude estimate of the edge frequency is stated as;

$$\varpi \sim \begin{cases} 3\gamma_o b/2\hbar R & for\ metallic\ CNs \\ \gamma_o b/\hbar R & for\ semiconductor\ CNs \end{cases}$$

[100], where R is the CN's radius. This condition is decisive for the applicability of the developed theory in CNs. As the CN radius increases, the upper limit for the permissible fundamental frequency is shifted to the red. Thus, CNs with not too large radii are of the most interest. When $\delta E \sim \gamma_o$, both restrictions on the Stark frequency impose the limitation on the external electric field strength: $|E_z| < \gamma_o/2eR$. Otherwise, the bond of π electrons with the crystalline lattice breaks down, resulting in a strong Stark broadening and making the dispersion laws (38 and 39) inapplicable. Note also that our theory ignores the role of σ electrons that come to play where the high-order harmonic frequencies become comparable with the frequencies of corresponding transitions. Having resonant character, these transitions can disturb the high-order harmonic spectrum in a restricted number of narrow bands [100].

CHAPTER FOUR

RESULTS AND DISCUSSION

In chapter 3, the Boltzmann kinetic equation was used to investigate and derive theoretically;

1. the current-density j_z/j_0 in CNT in the presence of an external electric field,

2. the high-frequency differential conductivity in CNT and

3. direct current generation due to wave mixing in CNT.

This chapter will focus on the numerical analysis of the final equations obtained in chapter 3.

The Negative Differential Effect in Carbon Nanotubes in the Presence of an External Electric Field

We studied theoretically the electron transport properties in carbon nanotubes under the influence of an external electric field $E(t)$ using Boltzmann's equation. The current-density equation was derived. NDC was observed in the $I - V$ characteristic curve for the conditions that $\omega\tau \ll 1$ (quai-static case). This appeared in the vicinity where the constant electric field E_o is equal to the amplitude of the AC electric field E_1 and the peak decreases with increasing E_1.

This phenomenon can also be used for the generation of terahertz radiation without electric current instability.

We observed that the current density j_z is a function of the electric field E_o and E_1. We illustrated how these parameters affect j_z using Matlab. Figure 35 represents the graph of j_z/j_o on E_o for $\beta = 2, 4, and 8$ at $\omega\tau = 0.2$. Figure 35(a) represents the armchair CNs and (b) superlattices. The figures show the linear dependence of j_z on E_o at weak strengths of the electric of the external field (i.e. the region of ohmic conductivity). As E_o increases, the current density j_z/j_o increases and at $E_o = E_o{}^{max}$ the current density reaches a maximum value $(j_z/j_o)^{max}$. Further increase of E_o results in the decrease of the j_z/j_o Thus, the region of negative differential conductivity (NDC) where $\partial j_z/\partial E_o < 0$. We noted that in the case investigated there is a shift of the maximum of the current density electric field curves towards larger E_o values. This "right shift" is caused by a nonliearity of the Esaki-Tsu characteristics which is very strong in CNs because of the high stark component (summation over r). The role of the high stark components in CNs is essential and intergral nonlinearity of the CNs is much higher than in SL [37, 10]. The shift increases with increasing the amplitude of the ac field.

The $I - V$ curves are qualitatively similar for the CNs and the superlattices (see Figure 35). However, the NDC effect in SL appeared at larger field strengths comparing with the CNs.

As E increases, the turning point value grows smaller for the CNs than the SL (see Figures 35 and 36). This indicates that nonlinearity in the CNs is much

higher than in superlattice. The current-density relation obtain for superlattice is characterized by the dispersion relation $\varepsilon(p) = \Delta(1 - \cos p_z d)$ and is expressed in [37] as

$$j_z/j_o = \sum_{k=-\infty}^{\infty} \frac{J_k^2(\beta)(\Omega + k\omega)\tau}{1 + \big((\Omega + k\omega)\tau\big)^2} \qquad (65)$$

Where as for the CNs is expressed as

$$j_z/j_o = \frac{8e\gamma_0}{\sqrt{3}\hbar n a_{c-c}} \sum_{r=1}^{\infty} r \sum_{s=1}^{n} f_{rs}\varepsilon_{rs} \sum_{k=-\infty}^{\infty} \frac{J_k^2(\beta)(\Omega r + k\omega)\tau}{1 + \big((\Omega r + k\omega)\tau\big)^2} \qquad (53)$$

for zigzag CNs and

$$j_z/j_o = \frac{8e\gamma_0}{3\hbar n a_{c-c}} \sum_{r=1}^{\infty} r \sum_{s=1}^{n} f_{rs}\varepsilon_{rs} \sum_{k=-\infty}^{\infty} \frac{J_k^2(\beta)(\Omega r + k\omega)\tau}{1 + (\Omega r + k\omega)^2\tau^2} \qquad (60)$$

for armchair CNs

From Eqs. (65), (53) and (60) we can conclude that the CNs exhibited so much nonlinearity due to the presence of the stark components (summation with respect to r in equation).

From expression (56) a graph of $j_z/j_o - E_o$ is plotted and it is observed that j_z assumes its maximum value in the vicinity of $Z_c \cong \beta$ for any given value of β. This indicates that NDC is observed where the constant field E_o is approximately equal to the amplitude of the AC electric field E_1. It is quite interesting to note that the graphs of expression (53) and (56) are qualitatively the same for $\omega\tau \leq 1$. See Figure 36 (a) and (b) and the peaks of the curves decreases with increasing E_1.

Also shown in Figure 37 a and b are the respective 3 dimensional plot of j_z/j_o versus E_o and n for the CNs. The figures exhibit NDC. We observed that at

small n values the magnitudes of the maximum current-density is greater for the armchair CNs than the for the zigzag CNs with similar radius for about 2. However, for larger values n both the armchair and zigzag CNs characteristics curves appear to be identical.

(a)   (b)
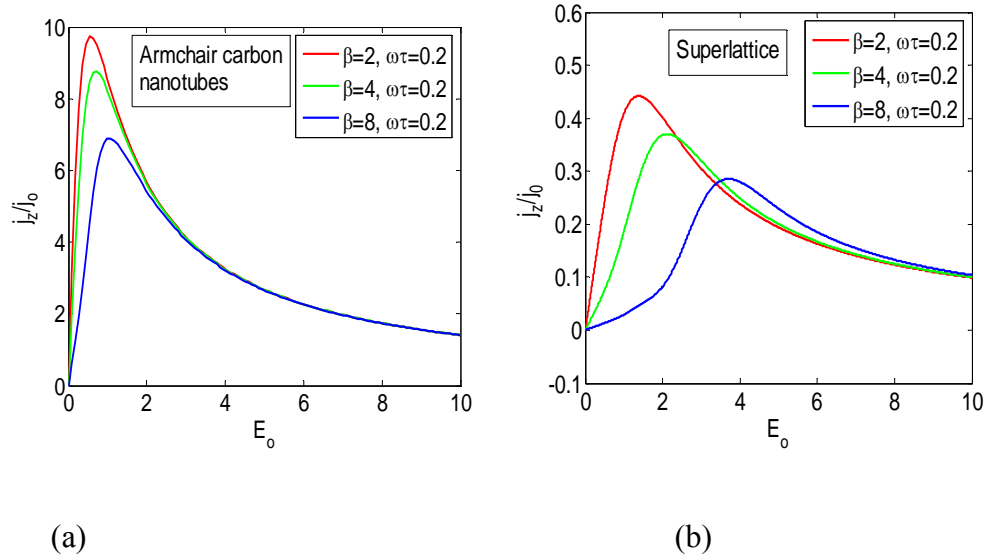
Figure 35: $j_z/j_o - E_o$ curves for (a) armchair and (b) superlattice when: $(-)$ $\omega\tau = 0.2, \beta = 2; (-) \omega\tau = 0.2, \beta = 4; (-)\omega\tau = 0.2, \beta = 8.$
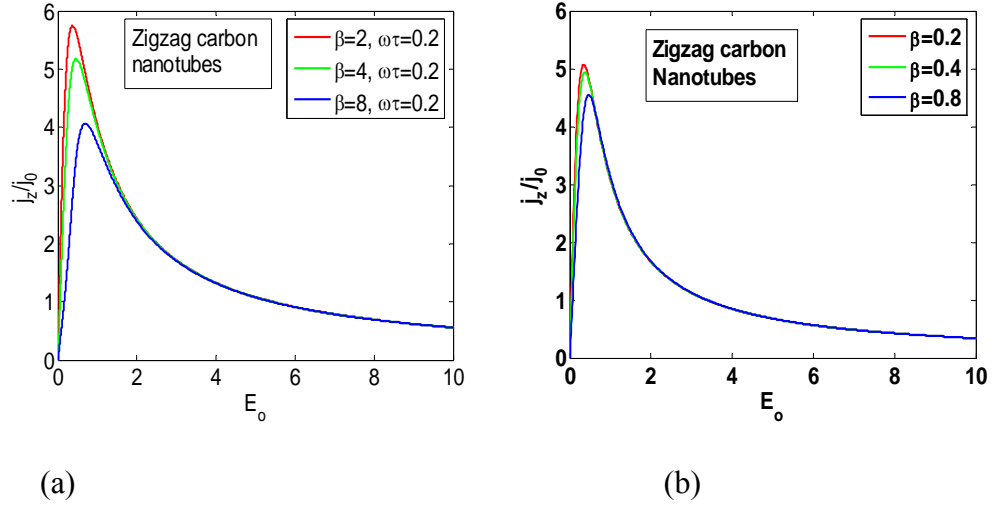
Figure 36: $j_z/j_o - E_o$ curves for (a) Expression (53); when: $(-)\omega\tau = 0.2, \beta = 2$; $(-)\omega\tau = 0.2, \beta = 4$; $(-)\omega\tau = 0.2, \beta = 8$ and (b) Expression (56); when: $(-)\beta = 0.2$; $(-)\beta = 0.4$; and $(-)\beta = 0.8$
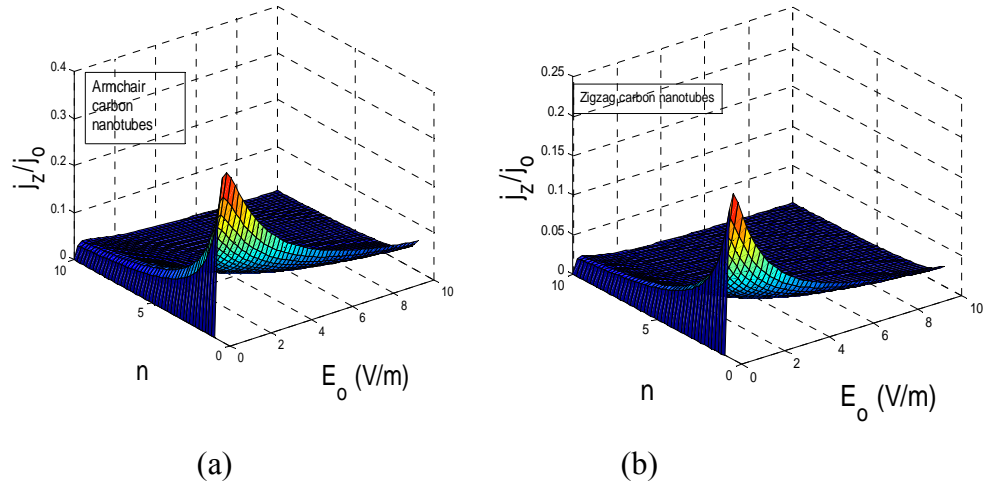
Figure 37: j_z/j_o is plotted against E_o and n.

High-frequency Differential Conductivity in Carbon Nanotubes

We present a semiclassical theory of electron transport in a CNT exposed to ac-dc driven fields. The Boltzmann's equation is solved in the frame work of momentum-independent relaxation time. An analytical expression for the current

density is obtained for the situation that $\beta \ll 1$. The nonlinearity is analyzed basically on the dependence of the current density on the frequency.

The real part of the high-frequency conductivity obtained via the calculation of Eqs. (60) and (53) are presented in Figure 38 a and b for the armchair CNs (18,18) and the zigzag CNT (18,0), respectively. In the limit $\omega \to 0$, Eq. (54) and (61) reduce to the form of ref [33, 27] as;

$$\sigma(o) = \frac{8e\gamma_0}{\sqrt{3}\hbar n a_{c-c}}\left(\frac{(\Omega r\tau)\beta^2}{2}\right)\sum_{r=1}^{\infty} r^2 \sum_{s=1}^{n} f_{rs}\varepsilon_{rs}\frac{1-(\varrho r)^2}{(1+(\varrho r)^2)^2} \quad (66)$$

for zigzag CNs and

$$\sigma(o) = \frac{8e\gamma_0}{3\hbar n a_{c-c}}\left(\frac{(\Omega r\tau)\beta^2}{2}\right)\sum_{r=1}^{\infty} r^2 \sum_{s=1}^{n} f_{rs}\varepsilon_{rs}\frac{1-(\varrho r)^2}{(1+(\varrho r)^2)^2} \quad (67)$$

for armchair CNs.

Where $Q \equiv \Omega\tau$, $\Omega = eaE_o$ for zigzag CNs and $\Omega = eaE_o/\sqrt{3}$ for armchair CNs. Using the approach of [33, 27] the parameter Q may also be expressed as $E_o/E_o{}^{max}$, where $E_o{}^{max}$ is the critical field of the $V-I$ characteristic, defined as the field at which the current density peaks and the differential conductivity goes through zero. As $E_o > E_o{}^{max}$, the static differential conductivity ($\omega \to 0$) is negative and low-frequency conductivity is also negative. This is the earlier results of Esaki and Tsu [25] and therefore an applied low-frequency will be enhanced.

For sufficiently large values of Q (i.e. $Q \gg 1$), resonance minimum occurs at about the frequency $\left(1 - \frac{1}{Q}\right).\Omega$ and the resonance enhancement will be about $\frac{Q}{4}$ relative to $\sigma(o)$ (See figure 38).

The conductivity crosses over to the positive values at the frequency $\omega = \Omega(1 - 1/Q^2)$. For large values of Q it appears just below Ω [33].

We observe that the real part of the differential conductivity is initially negative at zero frequency and becomes more negative with increasing frequency, until it researches a resonance minimum at a frequency just below the Bloch frequency and then turning positive (resonance enhancement) just below the Bloch frequency. This resonance enhancement is indicative for terahertz gain without the formation of current instabilities induced by a negative dc conductivity.

(a)   (b)
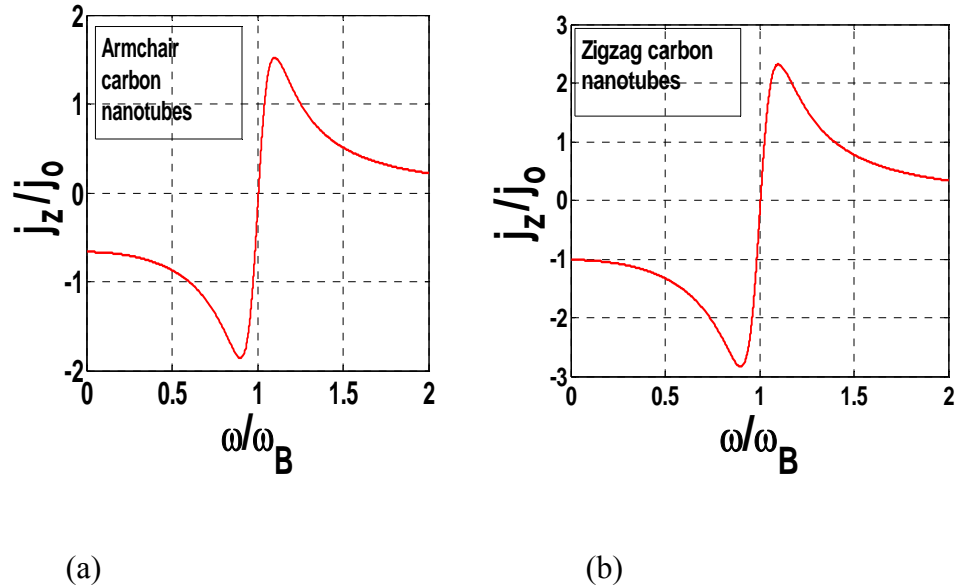
Figure 38: $j_z/j_o - \omega/\omega_B$ curves for (a) armchair and (b) zigzag.

Photon-assisted Peaks and Large-signal Gain in Carbon Nanotubes

We theoretically developed current dynamics of a single-wall carbon nanotubes to Bloch oscillate for the situations where, if in addition to the dc field

also an alternating field is applied, at a frequency somewhat below the Bloch frequency associated with the dc field. The differential conductivity at the ac drive frequency is then negative, since the nonlinearities in the system is strong, the dc differential conductivity is modified by the ac field. Large alternating fields can open new transport channels, which can be seen as distinctive peaks in the $V - I$ characteristic curve Figure 40. Because of the resonances the differential conductivity is positive at certain ranges of the dc field and domainless amplification of THz radiation can be achieved.

If we re-write eq. (53) in the form;

$$j_z = \frac{8e\gamma_0}{\sqrt{3}\hbar n a_{c-c}} \sum_{r=1}^{\infty} r \sum_{k=-\infty}^{\infty} J_k^2(r\beta) j_{dc}(\mathrm{E_o}r + kE^*) \sum_{s=1}^{n} f_{rs}\varepsilon_{rs} \quad (68)$$

Where $E^* = \frac{\hbar\omega}{a}$ and for $k \neq 0$, $j_{dc}(\mathrm{E_o}r + kE^*)$ is the photon replicas.

Expression (68) is the superposition of the dc current density and its various photon replicas and we obtain the dc differential conductivity as;

$$\sigma_z = \frac{\partial j_z}{\partial E_o}$$

$$= \frac{8e\gamma_0}{\sqrt{3}\hbar n a_{c-c}} \sum_{r=1}^{\infty} r \sum_{k=-\infty}^{\infty} k J_k^2(r\beta) \frac{(1 - (\mathrm{E_o}r + kE^*)^2)}{(1 + (\mathrm{E_o}r + kE^*))^2} \sum_{s=1}^{n} f_{rs}\varepsilon_{rs} \quad (69)$$

Figure (39) elucidates the dependence of j_z on $\mathrm{E_o}$ arising under the action of strong ac field for $\omega\tau = 10$. We noted a very steep positive slope in the neighbourhood of E^*, which indicates the differential conductivity is positive (PDC) in this region. The PDC is considered one of the conditions for electric stability in the system. It was observed from Figure 39 shows that the peaks occur

slightly below $E^* + E_o$. The negative ac conductivity at the drive frequency ω appears when $E_o > E^*$ and the range for the Bloch operation is $E^* < E_o < E^* + E^c$. From Figure (40), we noted that the PDC is within the range $E^* - E^c < E_o < E^* + E^c$.
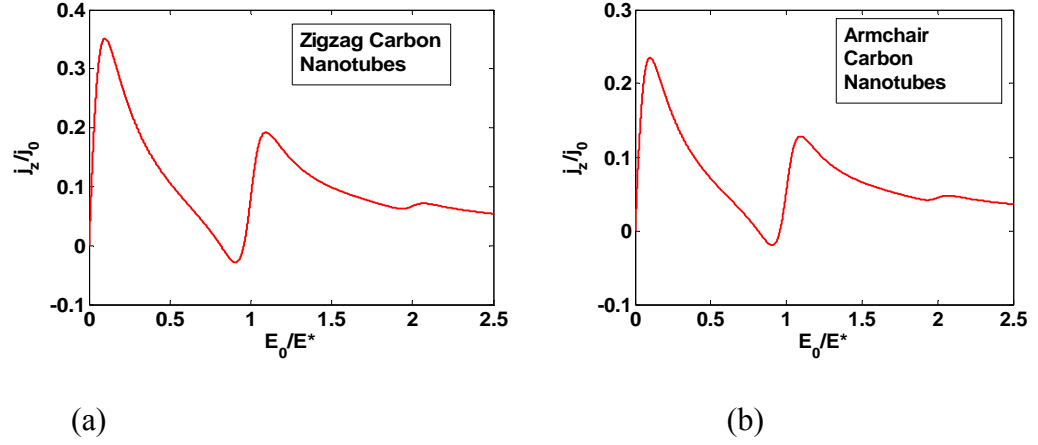
(a)   (b)

Figure 39: $j_z/j_o - E_o/E^*$ curves for (a) zigzag and (b) armchair carbon nanotubes.

(a)   (b)

Figure 40: $\sigma_z/j_o - E_o/E^*$ curves for (a) zigzag and (b) armchair carbon nanotubes.

92
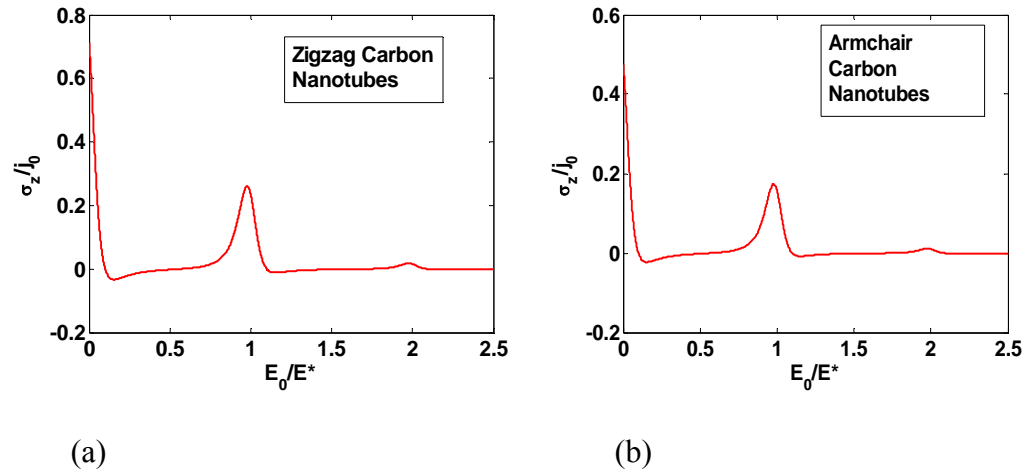
Direct Current Generation Due To Wave Mixing in Zigzag Carbon Nanotubes

Generation of direct current in zigzag carbon nanotubes due to harmonic mixing of two coherent electromagnetic waves is being considered. The electromagnetic waves have commensurate frequencies of $\omega_1 = \Omega$ and $\omega_2 = 2\Omega$. The rectification of the waves at high frequencies. i.e. $\Omega\tau \gg 1$ is quite smooth whiles at low frequencies there are some fluctuations. The nonohmicity observed in the $I - V$ characteristics is attributed to the nonparabolicity of the electron energy band which is very strong in carbon nanotubes because of high stark component. It is observed that the current falls off faster at lower electric field than the case in superlattice. For $\Omega\tau = 2$, the external electric field strength E^{max} for the observation of negative differential conductivity occurs around $1.03 \times 10^6 \, V/m$ which is quite weak. It is interesting to note that the peak of the curve shifts to the left with increasing value of $\Omega\tau$ [112].

Using the solution of the Boltzmann equation with constant relaxation time τ, the exact expression for current density in CNs subjected to an electric field with two frequencies $\omega_1 = \Omega$ and $\omega_2 = 2\Omega$ was obtained.

We noted that the current density j_z is dependent on the electric field E_2 and E_1, the phase difference θ, the frequency Ω, the relaxation time τ and n. To further understand how these parameters affect j_z, we sketched equation (56) using Matlab. Figure 41 represents the graph of j_z/j_o on β_1 for $\Omega\tau = 0.3, \ 0.5, \ 0.9, \ 1 \ and \ 2$. We observed that as β_1 increases, the magnitude of the normalized current j_z/j_o increases and at $\beta_1 = \beta_1{}^{max}$ the normalized current reaches a maximum value. Further increase of β_1 results in the decrease of the magnitude

of j_z/j_o. Thus, the region with negative differential conductivity (NDC) $\partial j_z/\partial \beta_1 < 0$. We further observed that for $r = 1$, the curve for the nanotube is qualitatively the same as the superlattice except that the peaks occur at higher values see Figure 41 (a) and 42. As we increase the r values the magnitude of the normalized current also increases. For $r > 1$ we observed some fluctuations in the NDC region when $\Omega\tau \ll 1$. On the other hand for $\Omega\tau \gg 1$ we observed that the current decreases monotonically in the NDC region. This indicates that at high frequency the rectification is smooth as against the case of low frequency. See Figures 41 (b)-(e). The rectification can be attributed to non ohmicity of the carbon nanotube for the situation where it Bloch oscillates and the high stark component (summation over r). From Figure 41 (d) for example, if $\Omega\tau = 2$, the external electric field strength E^{max} necessary to induce the stark frequency for the observation of negative differential conductivity occurs around $1.03 \times 10^6 \, V/m$ which is quite weak. As can be seen from Figsure 41(b)-(e) the peak of the current shifts to the left with increasing value of $\Omega\tau$. In comparing the peak values of Figure 41 (d) with the result in [37] (see Figure 2) for $\Omega\tau = 1$, the ratio $\frac{|j_{max}^{CNs}|}{|j_{max}^{SL}|} \approx 40$ and for or $\Omega\tau = 2$, the ratio $\frac{|j_{max}^{CNs}|}{|j_{max}^{SL}|} \approx 44$ which is quite substantial.

We sketched also the graph of j_z/j_o against $\Omega\tau$ for $\beta_1 = 0.3, \ 0.5, \ 0.9,$ $1 \ and \ 2$. The graph also displayed a NDC. See Figure 43. Interestingly unlike in SL as indicated in [37] where the current is positive and has a maximum at the value $\Omega\tau \approx 0.71$ irrespective of the amplitude of the electric field E_1 in carbon nanotubes because of the high stark component the maximum peak shifts towards the left with increasing value of β_1 see Figure 43 (b)-(d).

(a)

(b)

(c)

(d)

(e)
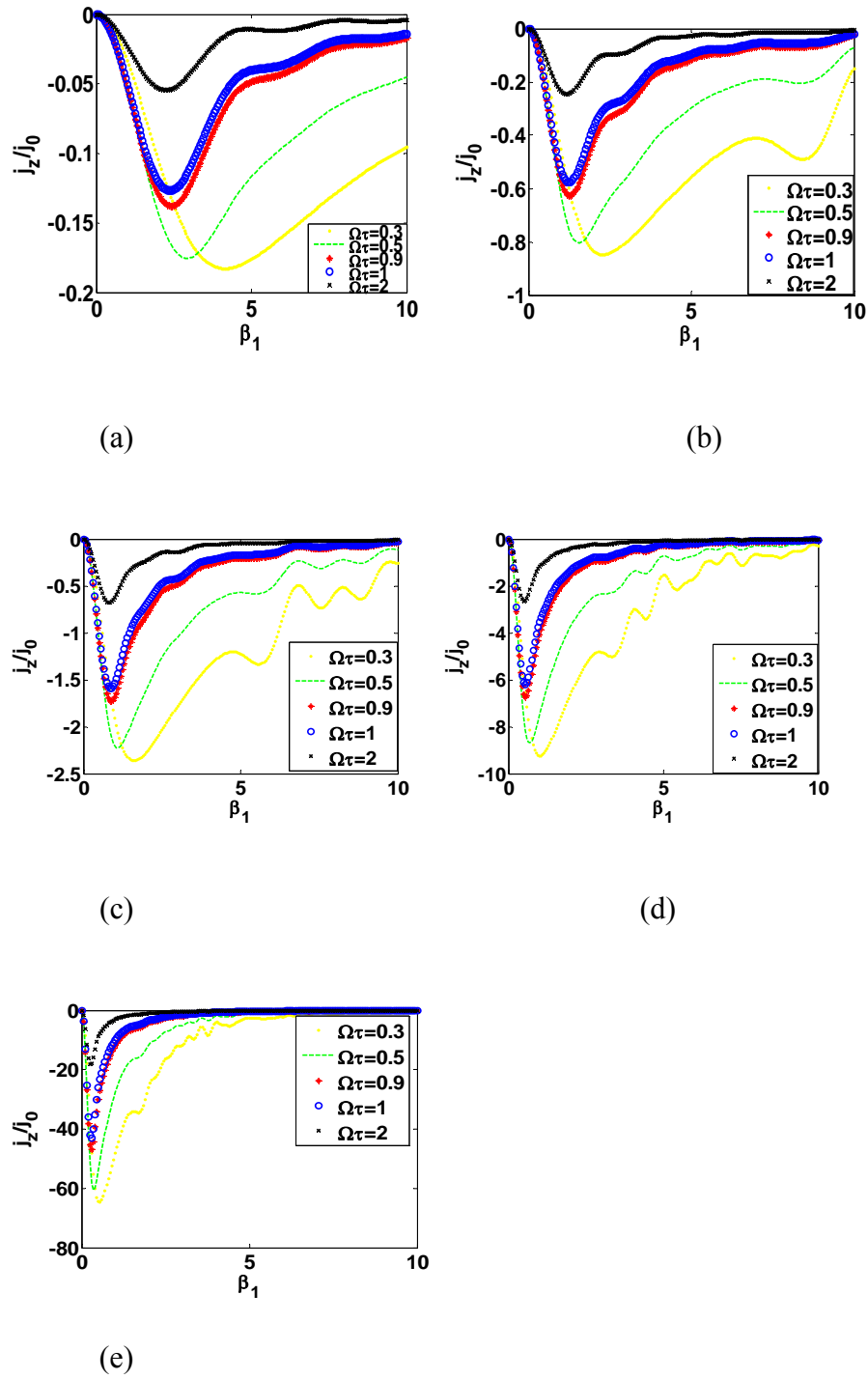
Figure 41: j_z/j_o **is plotted against** β_1**for** $(\cdots)\,\Omega\tau = 0.3;\ (\cdots)\,\Omega\tau = 0.5;\ (****)\,\Omega\tau = 0.9\ (oooo)\Omega\tau = 1;\ and\,(\cdots)\ \Omega\tau = 2$ **. When (a)** $r = 1,$ **(b)** $r = 2$ **, (c)** $r = 3,$ **(d)** $r = 5,$ **and (e)** $r = 10$.
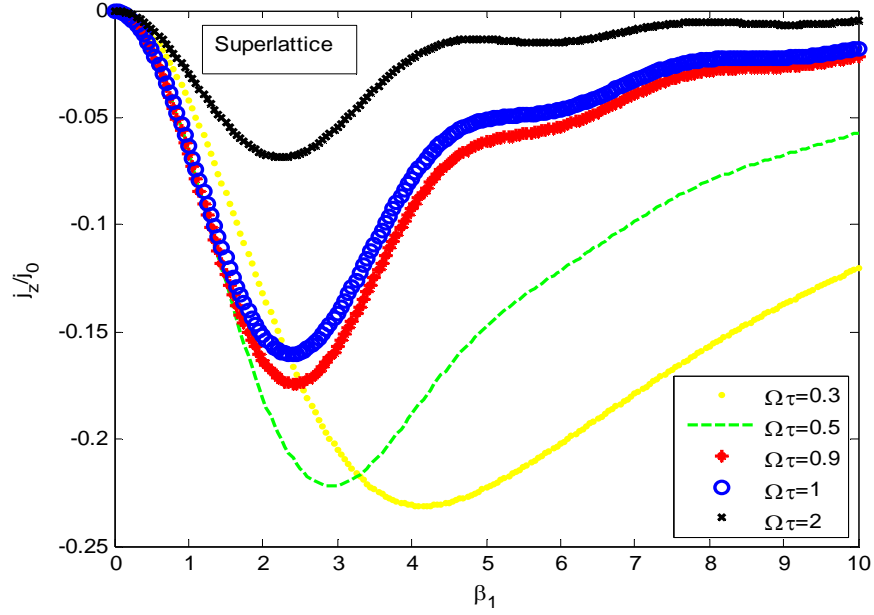
Figure 42: j_z/j_o is plotted against β_1 for $(\cdots) \, \Omega\tau = 0.3$; $(\cdots) \, \Omega\tau = 0.5$; $(****) \, \Omega\tau = 0.9 \, (oooo)\Omega\tau = 1; and \, (\cdots) \, \Omega\tau = 2.$

However, when $r = 1$ as stated above it behaves like SL. See Figure 43(a). It is worthwhile to note that $\Omega\tau_{max}$ can be used to determine the relaxation time of the dominant type of scattering (i.e. electron-phonon) in the nanotube. It is important to note that when the phase shifts θ lies between $\frac{\pi}{2}$ and $\frac{3\pi}{2}$ there is an inversion. See Figure 43.
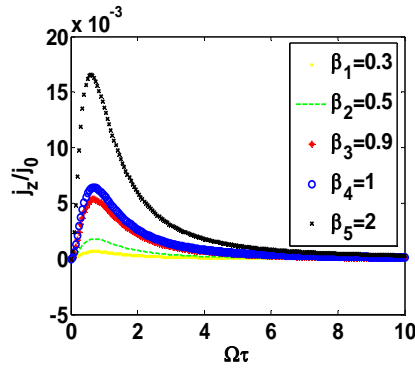
(a)

(b)

(c)

(d)

(e)
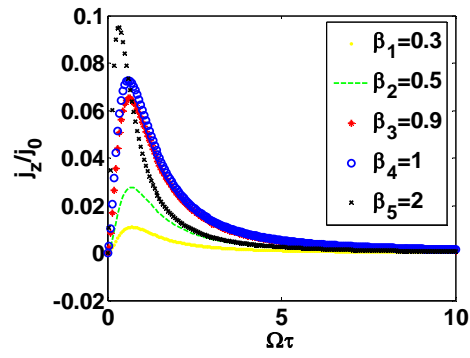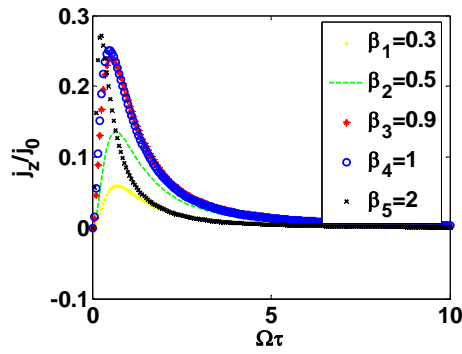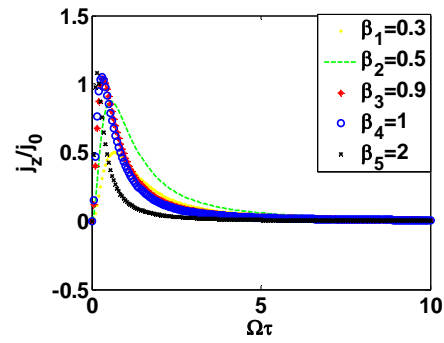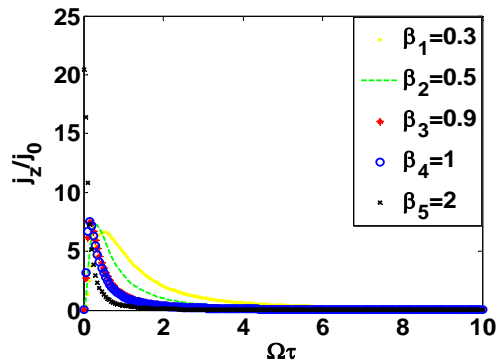
Figure 43: j_z/j_o is plotted against $\Omega\tau$ for (—) $\beta_1 = 0.3$; (···) $\beta_1 = 0.5$; (∗∗∗) $\beta_1 = 0.9$; (ᵒᵒᵒ) $\beta_1 = 1$; and (···) $\beta_1 = 2$. When (a) $r = 1$, (b) $r = 2$, (c) $r = 3$, (d) $r = 5$, and (e) $r = 10$.

97
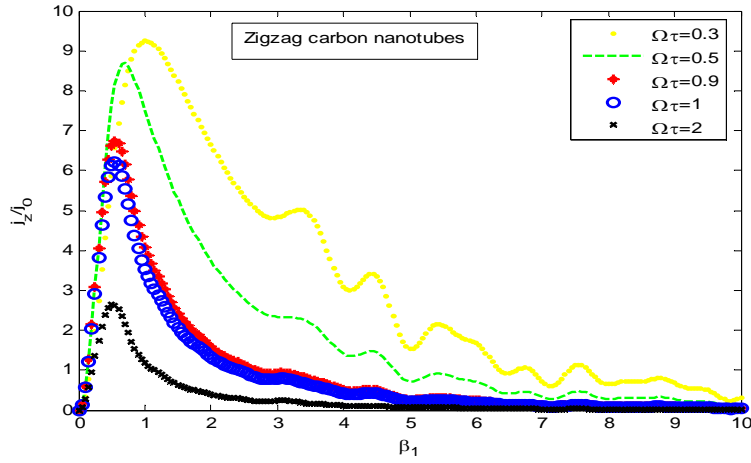
Figure 44: j_z/j_o is plotted against β_1 for $(\cdots)$ $\Omega\tau = 0.3$; $(\cdots)$ $\Omega\tau = 0.5$; $(****)$ $\Omega\tau = 0.9$ $(oooo)\Omega\tau = 1$ and $(\cdots)$ $\Omega\tau = 2$. When $r = 5$ and the phase shift θ lies between $\frac{\pi}{2}$ and $\frac{3\pi}{2}$.

We sketched also 3 dimensional graphs of the current against β_1 and n (see Figure 45).

(a)   (b)
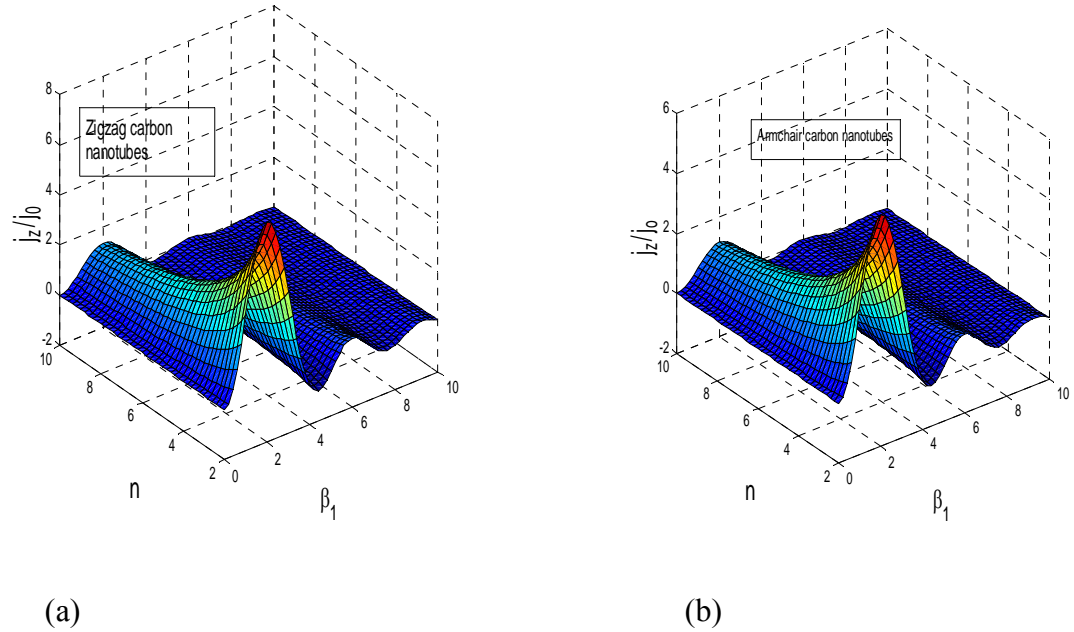
Figure 45: J_z/J_0 is plotted against β_1 and n for (a) zigzag and (b)armchair carbon nanotubes.

Rectification of sinusoidal signals by means of Armchair carbon nanotubes

The rectification of sinusoidal signals by means of single wall carbon nanotubes (CNs) due the harmonic mixing of two coherent electromagnetic waves with commensurate frequencies of $\omega_1 = \Omega$ and $\omega_2 = 2\Omega$ is investigated theoretically by solving the Boltzmann transport equation. We observed that nonohmicity in the $I - V$ characteristics is attributed to the nonparabolicity of the electron energy band which is very strong in carbon nanotubes because of high stark component. We found that smooth rectification is a function of both the frequency and the stark component. We suggest the use of this approach for sinusoidal rectification as well as the generation of terahertz radiation in CNs.

99

This can also be used for determining of the electron relaxation time in CNs [113, 114].

We discuss sinusoidal rectification by means of CNs subjected to an electric field with two frequencies $\omega_1 = \Omega$ and $\omega_2 = 2\Omega$ by solving the Boltzmann's transport equation.

Figure 46 illustrates the graphs of j_z/j_o on β_1 for $\Omega\tau = 0.3, 0.5, 0.9,$ 1 and 2 when (a)$r = 1$, (b) $r = 2$, (c) $r = 3$, (d) $r = 5$, and (e) $r = 10$. In the low limit of β_1, we observed that as β_1 increases, the magnitude of the normalized current j_z/j_o increases and at $\beta_1 = \beta_1{}^{max}$ the normalized current reaches a maximum value. Further increase of β_1 results in the decrease of the magnitude of j_z/j_o. Thus, the region with negative differential conductivity (NDC) $\partial j_z/\partial\beta_1 < 0$. For $r = 1$, the curves for the nanotubes are qualitatively the same as the superlattice except that the peaks occur at higher values see Figures 47(a), 48(a) and 49(a). As the r values increase, the magnitude of the normalized current also increases. For $r > 1$ we observed that the current decreases monotonically in the NDC region when $\Omega\tau \gg 1$. On the other hand for $\Omega\tau \ll 1$we noted some fluctuations in the NDC region. To further understand how the parameters, r and $\Omega\tau$ affect the rectification processes, j_z/j_o is plotted against β_1 for $\Omega\tau = 0.3$ and $\Omega\tau = 2$when (a) $r = 1$, (b) $r = 2$, (c) $r = 3$, and (d) $r = 10$ see Figure 48 and 49 respectively. It is interesting to note that for $r = 1$ and $\Omega\tau = 0.3$ we observed smooth rectification for the CNs and SL see Figure 47(a). However, in Figure 48 (b)-(d) for $r > 1$ we noted some fluctuations in the NDC region for only the CNs. We also noted smooth rectification in CNs when $r = 10$and $\Omega\tau = 2$. See Figure 49 (d). In contrast, we observed fluctuations in the CN and

SL for $r < 10$ and $\Omega\tau < 2$ see Figure 49 (a)-(c). The rectifications in the situations above can be attributed to non ohmicity of the carbon nanotube for the situation where it Bloch oscillates and the high stark component (summation over r). We also noted that the electric field strength necessary to induce the stark frequency for the observation of negative differential conductivity occurs at weaker field for an increasing values of r. As can be seen from Figure 47, 48, and 49, the peak of the current shifts to the left with increasing value of r.
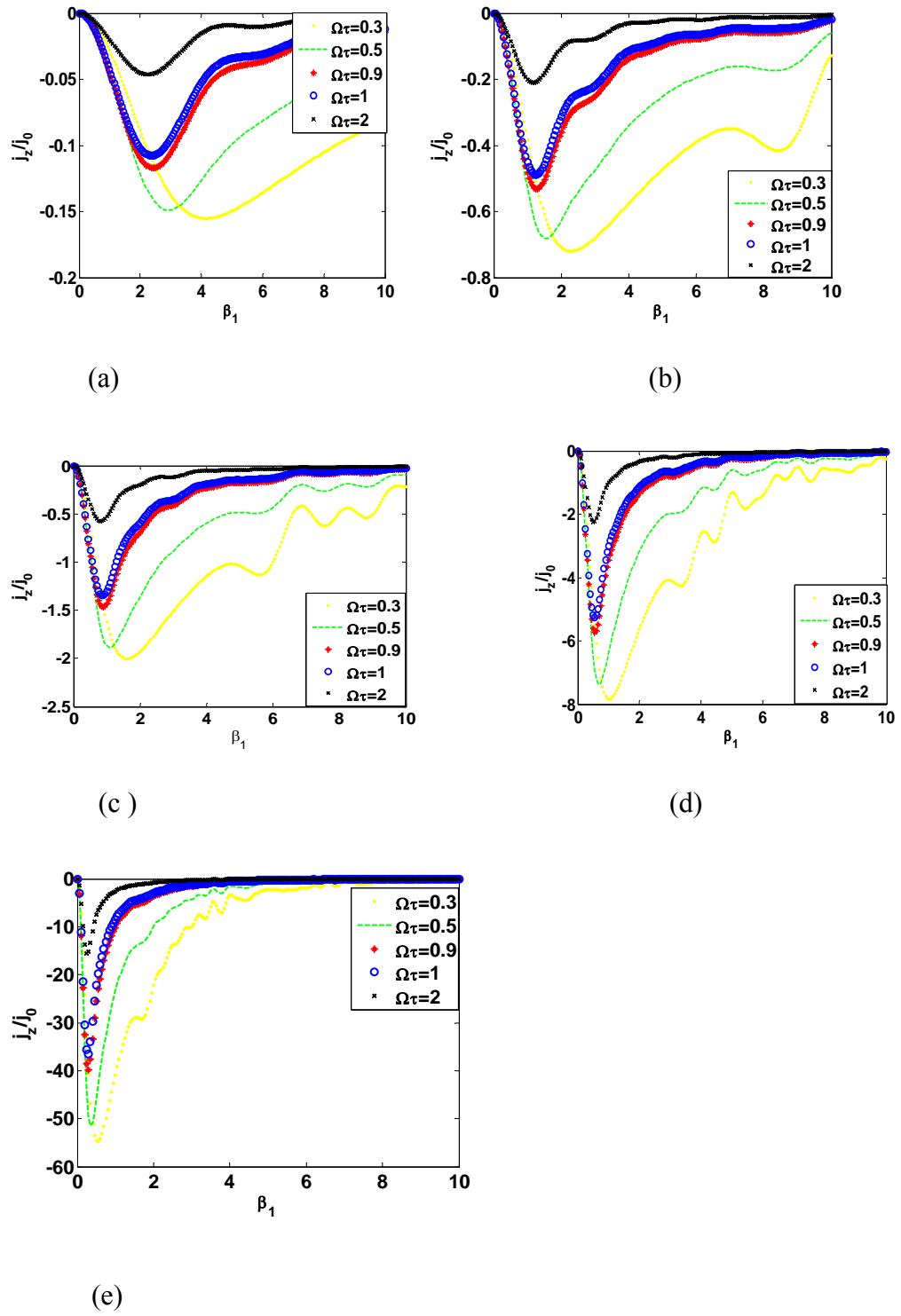
(a)

(b)

(c)

(d)

(e)

Figure 46. j_z/j_o **is plotted against** β_1**for** $(\cdots)\,\Omega\tau = 0.3;\;(\cdots)\,\Omega\tau = 0.5;\;(****)\,\Omega\tau = 0.9\;(oooo)\Omega\tau = 1;\;and\,(\cdots)\;\Omega\tau = 2$ **. When (a)** $r = 1,$ **(b)** $r = 2$ **, (c)** $r = 3,$ **(d)** $r = 5,$ **and (e)** $r = 10.$

(a)

(b)

(c)

(d)
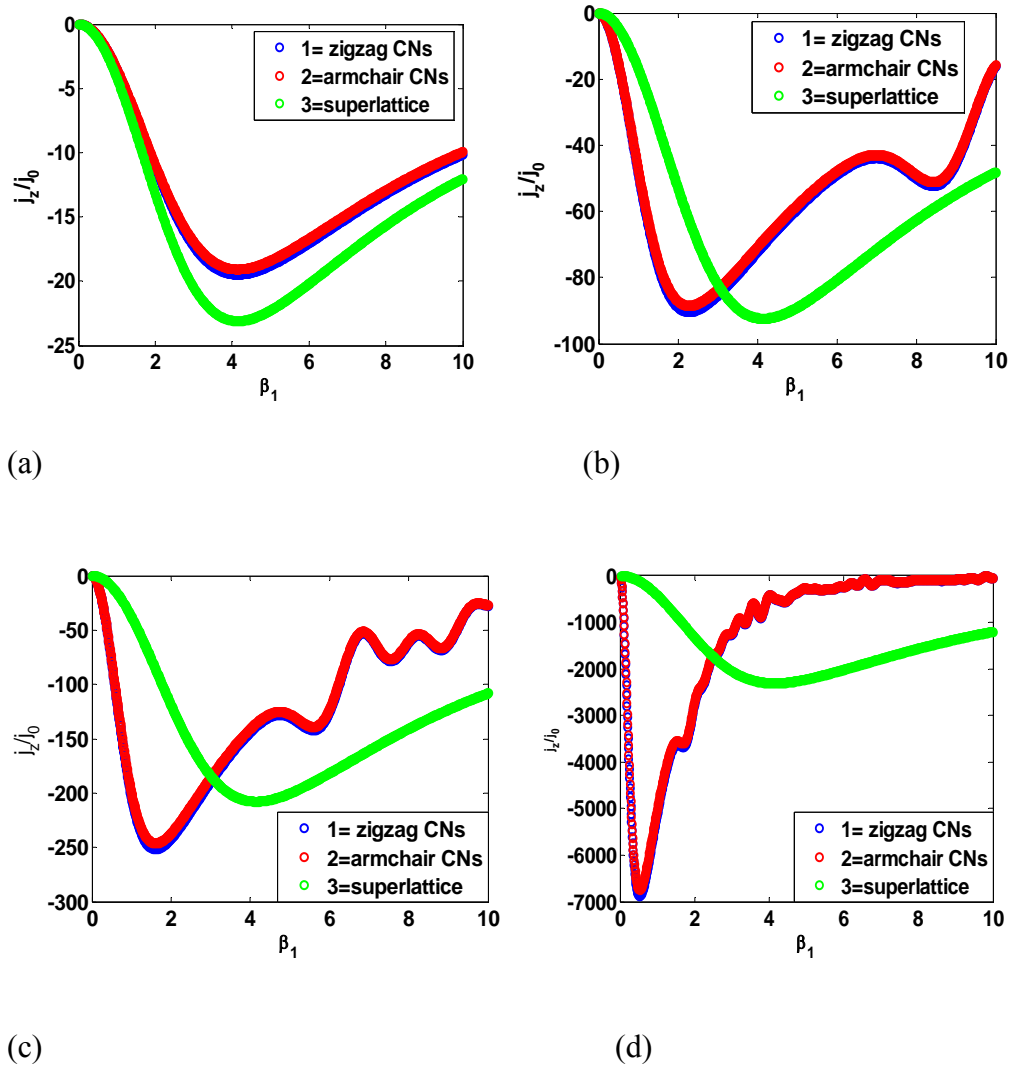
Figure 47. j_z/j_o **is plotted against** β_1**for** $\Omega\tau = 0.3$; $(\cdots)$ **Superlattice**; $(\ast\ast\ast)$**Armchair CNs**; $(oooo)$**Zigzag CNs**. **When (a)** $r = 1$, **(b)** $r = 2$, **(c)** $r = 3$, **and (d)** $r = 10$.

103
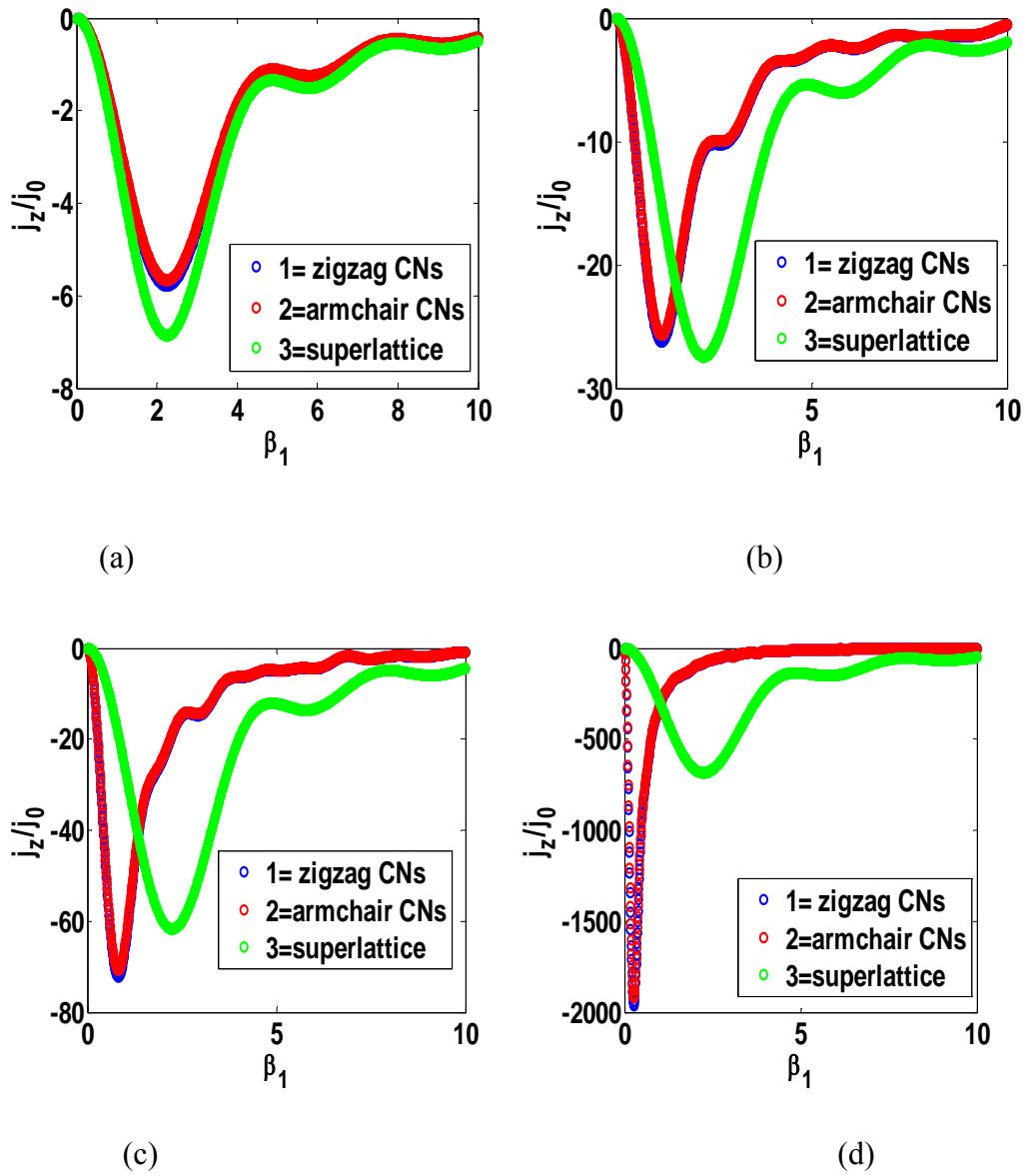
Figure 48. j_z/j_o **is plotted against** β_1 **for** $\Omega\tau = 2$; $(\cdots)$ **Superlattice;** $(***)$ **Armchair CNs;** $(oooo)$ **Zigzag CNs. When (a)** $r = 1$, **(b)** $r = 2$, **(c)** $r = 3$, **and (d)** $r = 10$.

CHAPTER FIVE

CONCLUSION AND RECOMMENDATIONS

Conclusion

Using the Boltzmann transport kinetic equation we theoretically obtained equations for the current density in CNs at room temperature when simultaneously exposed to a constant (dc) and high-frequency (ac) electromagnetic fields. We observed several physical effects using these equations.

We theoretically analyzed the generation and amplification of THz radiation in a CN subjected to ac-dc driven fields. In the conditions where the constant electric field E_o is equal to the amplitude of the AC electric field E_1 we observed NDC when $\omega\tau \ll 1$ (quai-static case) and the peak decreases with increasing E_1. This phenomenon can be used for the generation of terahertz radiation without electric current instability.

The dependence of real part of the high-frequency conductivity j_z/j_o on ω/ω_B was elucidated for the electron transport problem. We observe that the real part of the differential conductivity becomes more negative with increasing frequency and resonance enhancement appears just below the Bloch frequency when the differential conductivity is turning positive. This resonance

enhancement is indicative for terahertz gain without the formation of current instabilities induced by a negative dc conductivity.

We further investigated domainless amplification of THz gain for the situation where the ac field becomes large. It was observed that distinctive peaks appeared in the $V - I$ characteristic curve and because of the resonances the differential conductivity is positive at certain ranges of the dc field and THz radiation can be achieved without electric instabilities.

We have studied the direct current generation due to the harmonic wave mixing in carbon nanotubes and suggest the use of this approach in generation of THz radiation. We noted that smooth rectification is a function of both the frequency and the stark component. Thus, THz and dc generation and amplification in CNs provided by nonlinear motion of electrons in CNs is due to strong nonlinearity of CNs, which can be related to the dynamical localization of electrons in strong external fields. In this work we restricted ourselves to a single CN. The experimental conditions for an observation of the dc current effect are practically identical to those fulfilled in a recent experiment on the generation of harmonics of the THz radiation in a semiconductor superlattice [20]. This method can also be used to determine the relaxation time τ.

Recommendations

It may be possible to give an extension of this approach supplemented by the analysis of the phase-matching condition and extended to the case of oblique incidence of the driving field to the parallel-arranged CNs (CN ropes).

106

Further work can also be done on the following; generation of terahertz radiation by wave mixing in doped CNs as well as undoped chiral CNs, negative differential effect in doped CNs, and high-frequency differential conductivity in doped CNs. The others are high harmonic generation in doped CNs, and the effect of high-frequency field on transport properties of doped CNs using hot electron transport.

It may equally be possible to study these effects in graphene.

REFERENCES

[1] Siegel, P. H. "Terahertz technology", IEEE transactions on microwave
     theory and techniques, 50**,** no.3, pp. 910-928, 2002.

[2] Tonouchi, M. "Cutting-edge terahertz techniques", Nature photonics,
     1, pp.97-105, 2007.

[3] Miles, R. E., Harrison, P., and Lippens, D. "Terahertz sources and systems",
     Springer, 2001.

[4] Marandi, A. " Design and modeling of semiconductor terahertz sources
     based on nonllinear difference-frequency mixing", A thesis submitted
     in partial fulfilment of requirements for the degree of master of applied
     science, university of vicoria, canada, pp. 1-5, 2008.

[5] DeLucia, F. C. "Sensing with terahertz radiation", Ch. Spectroscopy in the
     terahertz Spectral regime, pp. 39-115. Springer, 2003.

[6] Philips, T. G. and Keene, J. "Submillimeter astronomy", Proceedings of the
     IEEE, 80, no.11, pp. 1662-1 677, 1992.

[7] Chapman, S. C., Blain, A.W., Ivison R.J.and Smail, I. R. "A median
     redshift of 2.4 for galaxies bright at submillimeter wavelength", Nature,
     422, no. 695-698, 2003.

[8] Swain, M. R. "Optics for studying star formation at high redshift",
     Astronomical Society of the Pacific, Publications, **11**0, no.750, pp. 991-
     994, 1998.

[9] Pickett, H. M. "THz Spectroscopy of the atmosphere", in Proc. SPIE, 3617, 1999.

[10] Hu, B. B. and Nuss, M. C. "Imaging with terahertz waves", Optics Letters, 20, pp. 1717-1718, 1995.

[11] Mittleman, D., Gupta, M., Neelamani, R., Baraniuk, R., Rudd, J. and Koch, M. "Recent Advances in terahertz imaging", Applied Physics B: Lasers and Optics, 68, no.6, pp.1085-1094, 1999.

[12] Crawley, D., Longbottom, C., Wallace, V.P., Cole, B., Arnone, D. and Pepper, M. "Three-Dimensional terahertz pulse imaging of dental tissue", Journal of Biomedical Optics, 8, no.2, pp. 303-307, 2003.

[13] Woodward, R. M., Cole, B. E., Wallace, V.P., Pye, R. J., Arnone, D. and Linfield, E. H. "Terahertz pulse imaging in reflection geometry of human skin cancer and skin tissue", Physics in Medicine and Biology,. 47, pp.3853-3863, 2002.

[14] Dickson, J. C. "Terahertz imaging of subjects with concealed weapons", inProc. SPIE, 6212, 2006.

[15] Mehdi, I. "Terahertz multiplier circuits", in IEE MTT-S International Microwave Symposium, pp. 341-344, 2006.

[16] Ferguson, B. and Zhang, X. C. "Materials for terahertz science and technology", Nature Materials, 1, pp. 26-40, 2002.

[17] Inguscio, M., Moruzzi, G., Evenson, K. M. and jennings, D. A. "A review offrequency measurements of optically pumped lars for 0.1 to 8THz", Journal of Appplied Physics, 60, no. 161, 1986.

[18] Roberson, C. W. and Sprangle, P. "A review of free-electron lasers",
      Physics Fluids B, **1,** no. 1, 1989.

[19] Williams, B. S." Terahertz quantum cascade lasers", Nature Photonics,
      1, pp.517-525, 2007.

[20] Faist, J., Capasso, F., Sivco, D. L., Sirtori, C., Hutchinson, A. L. and Cho,
      A. Y. "Quantum cascade lasers", Science 264**,** no. 5158, pp. 553-556, 1994.

[21] Kazarinov, R. F. and Suris, R. A. "Possibilty of the amplification of
      electromagnetic waves in a semiconductor with superlattice", Soviet
      Physics semiconductors-USSR, **5** pp.707-709. 1971.

[22] Pamplin, B. R. "Molecular Beam Epitaxy", Elservier, 1980.

[23] Lee, A. W. M., Qin, Q., Kumar, S., Williams, B. S., Hu, Q. and Reno, J. L.
      "High power and high- tempeture terahertz quantum cascade lasers bsed on
      lens coupled metal-metal wave quides", Optical Letters, 19, 2840-2844,
      2007.

[24] Baker, C., Gregory, J., Evans, M., Evans, Tribe, W., Linfield, E. and
      Missous, M. "All- Optoelectronics terahertz system using low-temperature-
      grown InGaAs Phtomixers", Optics Express, **13,**no. 23, pp. 9639-9644,
      2005.

[25] Esaki, L. and Tsu, R. "Superlattice and Negative Differential Conductivity
      in Semiconductors", IBM J. Res. Dev. 14, pp. 61-65, 1970.

[26]   Bouchard, A.M., and Luban M. "Semiconductor superlattices as terahertz
      generators", Phys. Rev. B. 47**,** 6815, 1983.

[27] Ktitorov, S. A., Simin, G. S. and Sindalovskii, V. Y. "Bragg reflections and
      the high-frequency conductivity of an electronic solid-state plasma", Fizika

Tverdogo Tela, **13**, pp. 2230-2233, 1971. [Soviet Physics - Solid State 13, 1872-1874, 1972].

[28] Büttiker, M. and Thomas, H. "Current Instability and Domain Propagation Due to Bragg Scattering", Phys. Rev. Lett. **38**, 78 (1977), Z. Phys. 33, 275 (1979), Z. Phys. 34, \301, 1979.

[29] Schomburg, E., Blomeier, T., Hofbeck, K., Grenzer, J. Brandl, S., Lingott, I., Ignatov, A. A. Renk, K.F., Pavel'ev, D.G., Koschurinov, Y. Ya. Melzer, B. Ustinov, V. M. Ivanov, S. V. Zhukov, A. and Kop'ev, P. S. "Current oscillation in superlattices with different miniband widths", Phys. Rev. B 58,7, 4035, 1998.

[30] Hyart, T., Alekseev, K. N., Leppanen, A., and Thumeberg, E. V., "Terahertz Bloch oscillator with suppressed electric domains: Effect of elastic scattering", arXiv:cond-mat/0511145v1

[31] Ryndyk, D.A., Demarina, N.V., Keller, J., and Schomburg, E. "Superlattice with hot electron injection: an approach to a Bloch oscillator", Phys. Rev. **B** 67, 2003.

[32] Copeland,J. A., "A New Mode of Operation for Bulk Negative Resistance", Proc. IEEE **54**, 1479, 1966.

[33] Kroemer, H. "Large-amplitude oscillation dynamics and domain suppression in a superlattice Bloch oscillator", cond-mat/0009311 (2000).

[34] Romanov, Y. Bovin, V. and Orlov, L. "Nonlinear amplification of electromagnetic oscillations in semiconductors with superlattices", Sov. Phys. Semicond. **12**, 9, 987, 1978. [Fiz. Tekh. Poluprovodn. 12, 1665 (1978)].

[35] Mensah, S. Y. "The effect of high frequency field on the transport properties of superlattices", J. Phys.: Condens. Matter **4,** L325, 1992.

[36] Klappenberger, F., Alekseev, K. N., Renk, K. F., Scheuerer, R., Schomburg, E., Allen, S. J. Ramian, G.R. Scott, J. S. S Kovsh, A. Ustinov, V. and Zhukov, A. "Ultrafast creation and annihilation of space-charge domains in a semiconductor superlattice observed by use of terahertz fields", Eur. Phys. J. B 39, 483-489, 2004.

[37] Dragoman, D. and Dragoman, M. "*Terahertz fields and applications*", Progress in Quantum Electronics **28**, pp. 1–66, 2004.

[38]   Iijima, S. "Helical microtubules of graphitic carbon", Nature **354**, pp. 56– 58, 1991.

[39] Saito, R. Dresselhaus, G. and Dresselhaus, M.S. "*Physical Properties of Carbon Nanotubes*", Imperial College Press, London, 1998.

[40] Dresselhaus, M.S., Dresselhaus, G. and Avouris, P.H. "*Carbon Nanotubes: Synthesis, Structure, Properties, and Applications*", Springer-Verlag, Berlin, 2001.

[41]   Reich, S., Thomsen, C. and Maultzsch, J. "*Carbon Nanotubes: Basic Concepts and Physical Properties*", Wiley, Berlin, 2004.

 [42] Manohara, H.M. Bronikowski, M.J. Hoenk, M. Hunt, B.D. and Siegel, P.H."High-current-density field emitters based on arrays of carbon nanotube bundles", J. Vac. Sci. Technol. B **23**, pp. 157–161, 2005.

[43] Maksimenko, A.S. and Ya. Slepyan, G. "Negative differential conductivity in carbon Canotubes", Phys. Rev. Lett. **84**, pp. 362– 365, 2000.

[44] Pennington,G. and Goldsman, N. "Semiclassical transport and phonon scattering of electrons in semiconducting carbon nanotubes", Phys. Rev. B, **68**, p. 045426, 2003.

[45] Dragoman, D. and Dragoman, M. "Terahertz oscillations in semiconducting carbon nanotube resonant-tunneling diodes", Physica E **24**, pp. 282–289, 2004.

[46] Odintsov, A.A. "Schottky Barriers in Carbon Nanotube Heterojunctions", Phys. Rev. Lett. 85, pp. 150–153, 2000.

[47] L´eonard F. and Tersoff, J. "Negative Differential Resistance in Nanotube Devices", Phys. Rev. Lett. **85**, pp. 4767–4770, 2000.

[48] Yang, M.H., Teo, K.B.K., Milne, W.I. and Hasko, D.G. "Carbon nanotube Schottky diode and directionally dependent field-effect transistor using asymmetricacontacts", Appl. Phys. Lett. **87,** p. 253116, 2005.

[49] Lu, C., An, L., Fu, Q. Liu, J., Zhang, H. and Murduck, J. "Schottky diodes from Asymmetric metal-nanotube contacts", Appl. Phys. Lett. **88**, p. 133501, 2006.

[50] Kibis, O.V., Parfitt, D.G.W. and Portnoi, M.E. "Superlattice properties of carbon nanotubes in a transverse electric field", Phys. Rev. B **71,** pp. 035411, 2005.

[51] Slepyan, G.Ya., Maksimenko, S.A., Kalosha, V.P., Herrmann, J., Campbell, E.E.B. and Hertel, I.V. "Highly efficient high-order harmonic generation by metallic carbon Nanotubes", Phys. Rev. A **60**, pp. 777–780, 1999. 1999.

[52] Slepyan, G. Ya., Maksimenko, S.A., Kalosha, V.P., Gusakov, A.V. andHerrmann, J. Phys. Rev. A **63,** 053808, 2001.

113

[53] Dragoman, D. and Dragoman, M. "Terahertz continuous wave amplification in semiconductor carbon nanotubes", Physica E 25, pp. 492–496, 2005.

[54] Dragoman, M., Cismaru, A., Hartnagel H. and Plana, R. "Reversible metal-semiconductor transitions for microwave switching applications", Appl. Phys. Lett. 88, p. 073503, 2006.

[55] Slepyan, G. Ya. Shuba, M.V. Maksimenko, S.A. and Lakhtakia, A. "Theory of optical scattering by achiral carbon nanotubes and their potential as optical nanoantennas", Phys. Rev. B 73, p. 195416, 2006.

[56] Kroto, H. W., Heath, J. R., Obrien, S. C., Curl, R. F. and Smalley, R. E. "C-60-Buckminsterfullerene", Nature, **318**, 162–163, 1985.

[57] Michael, J. O. "*Carbon Nanotubes Properties and Applications*", Taylor and Francis Group, LLC, pp. 2-16, 2006.

[58] Dresselhaus, M. S., Dresselhaus, G. and Saito, R. "*Physics of carbon nanotubes*", Carbon, **33**, 883–91, 1995.

[59] Smalley, R. E. "*Formation and properties of C60 and the fullerenes*", National Institute of Standards and Technology, Dec. 6–7, 1990.

[60] Dresselhaus, M. S. "Oral presentation at fullerene workshop", University of Pennsylvania, 1991.

[61] Iijima, S. and Ichihashi, T. "Single-shell carbon nanotubes of 1-nm diameter", Nature, **363**, 603–605, 1993.

[62] Bethune, D. S., Klang, C. H., de Vries, M. S., Gorman, G., Savoy, G.,Vazquez, J. and Beyers, R. "Cobalt-catalysed growth of carbon nanotubes with single-atomic-layer walls", Nature, **363**, 605–607, 1993.

[63] Bacon, R. "Growth, structure, and properties of graphite whiskers", Journal of Applied Physics, **31**, 283–290, 1960.

[64] Oberlin, A., Endo, M., and Koyama, T. "Filamentous growth of carbon through benzene decomposition", Journal of Crystal Growth, **32**, 335–349, 1976.

[65] Nacci, C. "*Scanning Tunneling Microscopy Investigation of Functionalized Carbon Nanotubes*", Anno Accademico, Pp.2-16, 2005.

[66] Pan, Z.W., Xie, S. S., Chang, B.H., Wang, L. L., Lui, W., Zhou, W.Y., Li, W.Z., Qian, L. "Very long carbon nanotubes", Nature 394 631-632, Numb. X., Nature, **394,** 631, 1998.

[67] Dekker, C. "Disorder and Interaction Quantum Hall and Mesoscopic Systems", Presentaion, 1998.

[68] Walters, D. A., Ericson , L. M., Casavant, M. J., Liu, J., Colbert, D. T., Smitgh, K.A., and Smalley, R. E. , "Elastic strain of freely suspended single-wall carbon nanotube ropes", Appl. Phys. Lett. **74** , 3803, 1999.

[69] Ishikawa H., Fudetani, S. and Hirohashi, M., "Mechanical properties of thin films measured by nanoindenters", Appl. Surf. Sci. **178**, 56, 2001.

[70] Kracke, B., and Damaschhke , B., "Measurement of nanohardness and nanoelasticity of thin gold films with scanning force microscope", Appl Phys. Lett. 77, 361, 2000.

[71]   Kun, L., Marko, B., and Siegmar R., "Conductance Spikes

in Single-walled Carbon Nanotube Field-effect Transistor", Applied

Phys Lett. **75**, 2494, 1999.

[72]   Martel, R., Schmidt, T., Shea, H.R., Hertel, T., and Avouris Ph.,

"Single wall and Multi-wall Carbon Nanotube Field-effect

Transistors", Applied Phys Lett. **73**, 2447, 1998.

[73] Bing Z., "State of Art in Nanotechnology Development",

Presentation, Department of ECE, University of Arizona, 2002.

synthesis and structure and properties and applications", Berlin

Springer-Verlag 2001.

[74] Tans, S. J., Devoret, M. H., Dai, H., Thess, A., Smalley, R. E.,

Geerligs, L. J., and Dekker, C.,"Individual Single-Wall Carbon

Nanotubes as Quantum Wires", Nature **386 ,** 474**,** 1997.

[75]   Clauss, W., Bergeron, D. J., and Johnson, A. T., "Atomic Resolution

STM Imaging of Twisted Single-Wall Carbon Nanotube", PRB **58,**

4266, 1998.

 [76] Wildöer, J. W. G., Venema, L. C., Rinzler, A. G., Smalley, R. E., and

Dekker, C.,"Electronic Structure of Atomically Resolved Carbon

Nanotubes", Nature **391**, 59, 1998.

[77] Odom, T. W., Huang, J.L., Kim, P., and Lieber, C. M., "Atomic

Structure and Electronic Properties of Single-Walled Carbon

Nanotubes", Nature **391,** 1998.

[78] Lemay, S.G, Janssen, J.W., van den Hout, M., Mooij, M., Bronikowski, M.J., Willis P.A., Smalley R.E,.Kouwenhoven L.P, and Dekker, C. "Two-dimensional imaging of electronic wavefunctions in Carbon nanotubes", Nature **412**, 17, 2001.

[79] Venema, L.C., Wildöer, J.W.G., Janssen, J.W., Ans, S.J.T, Tuinstra,

H.L.J.T., Kouwenhoven L.P., and Dekker C. "Imaging Electron Wave Functions of Quantized Energy Levels in Carbon Nanotubes", Science, **283**, p52 -55, 1999.

[80] Maltezopoulos, T., Kubetzk , A., Morgenstern, M., Wiesendanger, R., Lemay, S.G. and Dekker, C., "Direct observation of c onfined states in metallic single-wall carbon nanotubes", Appl. Phys. Lett. **83**,1011, 2003.

[81] Leroy, B.J., Lemay, S.G., Kong, J., and Dekker, C., "Scanning tunneling spectroscopy of suspended single-wall carbon nanotubes", Appl. Phys. Lett. **84**, 4280, 2004.

[82] Odom, T.W., Huang, J.L., Kim, P., and Lieber, C.M. J. "Structure and Electronic Properties of Carbon Nanotubes", Phys. Chem. B, **104**, 2794, 2000.

 [83]   Venema, L.C., Wildöer, J.W.G., Tuinstra, H.L.J.T., Dekker, C., Rinzler, A.G., and Smalley, R.E. "Length control of individual carbon nanotubes by nanostructuring with the scanning tunneling microscope", Appl. Phys. Lett., **71**, 2629, 1997.

[84] Venemaand, L.C., Wildöer, J.W.G., Dekker, C.**,** Rinzler, G.A., and
Smalley, R.E. "STM atomic resolution images of single-wall carbon
nanotubes", Appl. Phys. A, **66**, 153, 1998.

[85] Dai, H. "Carbon Nanotubes: Opportunities and Challenges", Surf.
Sci., 500, 218, 2002.

[86] Ajayan, P.M. and Zhou, O.Z., "Carbon Nanotubes: Synthesis,
Structure, Properties and Applications", Top. Appl. Phys., **80**, pp.
391–425., 2001.

[87] Qian, D., Wagner, G.J., Liu, W.K., Yu, M.F., and Ruoff, R.S.
"Mechanics of carbon nanotubes", Appl. Mech., Rev. **55**, 495, 2002.

[88] de Heer, W. A, Chatelain , A., Ugarte, D. "A Carbon Nanotube
Field-Emission Electron Source", Science, **270**, 1179, 1995.

[89] Rinzler, A. G., Hafner, J. H. , Nikolaev, P., Nordlander, P., Colbert,
D. T., Smalley, R. E. Lou, L., Kim, S. G., and Tománek, D.
"Unraveling Nanotubes: Field Emission from an Atomic Wire",
Science, **269**, 1550, 1995.

[90] Dresselhaus, M. S., Dresselhaus, G., and. Eklund, P. C. "*In Science of
Fullerenes and Carbon Nanotubes*" , Academic Press, Inc., New York,
1996.

[91] Brennan, K.F. "*The Physics of Semiconductors: With Applications to
Optoelectronic Devices*", Cambridge University Press, 1999.

[92] White, C. T. and Mintmire, J.W. "Density of States Reflects
Diameter in Nanotubes", Nature **394**, 29, 1998.

[93] Schönenberger, C. "Bandstructure of Graphene and Carbon Nanotubes: An Exercise in Condensed Matter Physics", 2001.

[94] Collins, P.G., and Avouris, P. "Nanotubes for Electronics", Scientific American, 2000.

[95] Saito, R., Fujita, M., Dresselhaus, G. and Dresselhaus, M. S. "Electronic structure of graphene tubules based on C60", Phsy. Rev. B, **46**, 1804, 1992.

[96] Suenaga, K. , Okazaki, T., Wang C.R., Bandow, S., Shinohara, H., and Iijima, S., *"Direct imaging of Sc2@C84 molecules encapsulated inside single-wall carbon nanotubes by high resolution electron microscopy with atomic sensitivity*", Phys. Rev. Lett. **90**, 055506 ,2003.

[97] Saito, R., Dresselhaus, G. and Dresselhaus, M. S. "*Physical Properties of Carbon Nanotubes*", World Scientific Publishing Company, 1st edition, 1998.

[98] Delaney P., Choi H. J., Ihm, J., Louie, S. G., and Cohen, M. L., "*Broken symmetry and pseudogaps in ropes of carbon nanotubes*", PRB **60**, 7899, 1999.

[99] Wallace P.R. "The Band Theory of Graphite", Phys. Rev. 71, 622,1947.

[100] Mintmire, J.W. and White, C.T. "Universal Density of States for Carbon Nanotubes", Phys. Rev. Lett. 81, 2506 - 2509, 1998.

[101] White, C. T. and Todorov, T. N. "Armchair carbon nanotubes as long ballistic conductors", Nature, **393**, 240, 1998.

[102] Ventra, M. D., Evoy, S., Heflin, J. R., *"Introduction to Nanoscale Science and Technology"*, Kluwer Academic Publishers, 2004.

[103] Dresselhaus, M.S. "Nanotechnology - New tricks with nanotubes", Nature **391**, 19, 1998.

[104] Saito R., Fujita M., Dresselhaus G., and Dresselhaus M.S. "Electronic structure of chiral graphene tubules", Appl. Phys. Lett., **60**, 2204, 1992.

[105] Kane, C., Balents, L. and Fisher, M. P. A. "Coulomb Interactions and Mesoscopic Effects in Carbon Nanotubes", Phys. Rev. Lett. 79, 5086 –5089, 1997.

[106] Lin, M. F. and Shung, K. W.K. "Magnetization of graphene tubules", Phys. Rev. B 52, pp. 8423–8438, 1995.

[107] Jishi, R. A., Dresselhaus, M. S., and Dresselhaus, G. "Electron-phonon coupling and the electrical conductivity of fullerene nanotubules", Phys. Rev. B 48, 11385 - 11389, 1993.

[108] Kane, C. L., Mele, E. J., Lee, R. S., Fischer, J. E., Petit, P., Dai, H., Thess, A., Smalley, R. E.,. Verscheueren, A. R. M., Tans, S. J. and Dekker, C., "Temperature Dependent Resistivity of Single Wall Carbon Nanotubes", Europhys. Lett. 41, 683-688 (1998).

[109] Balents, L. and Fisher, M. P. A, "Quantized thermal transport in the fractional quantum Hall effect", Phys. Rev. B 55, 973 (1997).

[110] Krotov,Y. A., Lee, D.-H. and Louie, S. G., "Low Energy Properties of (*n,n*) aCarbon Nanotubes", Phys. Rev. Lett. 78, 4245-4248 (1997).

[111] Egger, R. and Gogolin, A. O., "Effective Low-Energy Theory for Correlated Carbon Nanotubes", Phys. Rev. Lett. 79, 5082 (1997).

[112] Mensah, S.Y., Abukari, S. S., Mensah, N. G., Dompreh, K. A. Twum, A. and Allotey, F. K. A., "Generation of Terahertz Radiation by Wave Mixing in Zigzag Carbon Nanotubes", arXiv:1002.3233

[113] Mensah, S.Y., Abukari, S. S., Mensah, N. G., Dompreh, K. A. Twum, A. and Allotey, F. K. A., "Generation of Terahertz Radiation by Wave Mixing in Armchair Carbon Nanotubes", arXiv:1005.2869.

[114]   Abukari, S. S. Mensah, S.Y. Mensah, N. G. Dompreh, K. A. Twum A., and AAllotey, F. K., "Direct current generation due to wave mixing in zigzag carbon nanotubes", arXiv: 1007.1772v1 [cond-mat.mes-hall]

APPENDIX A

Current Density for Zigzag Carbon Nanotube

$$\frac{\partial f(p,t)}{\partial t} + eE(t)\frac{\partial f(p)}{\partial P} = -\frac{[f(p) - f_0(p)]}{\tau} \tag{A1}$$

$$f(p,t) = \Delta p_\varphi \sum_{s=1}^{n} \delta(p_\varphi - s\Delta p_\varphi) \sum_{r\neq 0} f_{rs}\, e^{iarp_z}\emptyset_\upsilon(t) \tag{A2}$$

$$f_0(p) = \Delta p_\varphi \sum_{s=1}^{n} \delta(p_\varphi - s\Delta p_\varphi) \sum_{r\neq 0} f_{rs}\, e^{iarp_z} \tag{A3}$$

Substituting Eqs. (A2) and (A3) into Eq.(A1) we get

$$\frac{\partial \emptyset_\upsilon(t)}{\partial t} + \left(iearE_0 + \frac{1}{\tau}\right)\emptyset_\upsilon(t) = \frac{1}{\tau} \tag{A4}$$

Solving the homogeneous differential equation corresponding to Eq. (A4) we obtain

$$\emptyset_\upsilon(t) = C(t)e^{-\int\left[iearE_0 + \frac{1}{\tau}\right]dt} = C(t)e^{-iearE_0 t}.e^{-\frac{t}{\tau}} \tag{A5}$$

Then by differentiating eq. (A5) we have

$$\frac{\partial \emptyset_\upsilon(t)}{\partial t} = \left[\frac{\partial C(t)}{\partial t} - \left(iearE_0 + \frac{1}{\tau}\right)C(t)\right]e^{-iearE_0 t}.e^{-\frac{t}{\tau}} \tag{A6}$$

Substituting for $\emptyset_\upsilon(t)$ and $\frac{\partial \emptyset_\upsilon(t)}{\partial t}$ in Eq. (A4), we obtain

$$\frac{\partial C(t)}{\partial t}e^{-iearE_0 t}.e^{-\frac{t}{\tau}} = \frac{1}{\tau}$$

$$\Rightarrow C(t) = \int \frac{1}{\tau}e^{iearE_0 t}.e^{\frac{t}{\tau}}.dt$$

$$C(t) = \frac{e^{iearE_0t} \cdot e^{\frac{t}{\tau}}}{(1 + iear\tau)} \tag{A7}$$

Substituting Eq. (A7) into Eq.(A5) we get

$$\emptyset_\upsilon(t) = \frac{1}{(1 + iearE_0\tau)} \tag{A8}$$

The surface current density is defined by

$$j_z = \frac{2e}{(2\pi\hbar)^2} \iint f(p) \, v_z(p) d^2p, \tag{A9}$$

or

$$j_z = \frac{2e}{(2\pi\hbar)^2} \sum_{s=1}^{n} \int_0^{\frac{2\pi}{a}} f\left(p_z, s\Delta p_\varphi, \emptyset_\upsilon(t)\right) v_z(p_z, s\Delta p_\varphi) dp_z \tag{A10}$$

Where the integration is over the first Brillouin zone, v_z is given by

$$v_z(p_z, s\Delta p_\varphi) = \frac{\partial \varepsilon_s(p_z)}{\partial P_z} \tag{A11}$$

$$\frac{\varepsilon(p_z, s\Delta p_\varphi)}{\gamma_0} = \varepsilon_s(p_z) = \sum_{r \neq 0} \varepsilon_{rs} \, e^{iarp_z}$$

$$v_z((p_z, s\Delta p_z) = \gamma_0 \sum_{r \neq 0} \frac{\partial\left(\varepsilon_{rs} e^{iearp_z}\right)}{\partial p_z} = \gamma_0 \sum_{r \neq 0} iar \, \varepsilon_{rs} e^{iearp_z} \tag{A12}$$

From Eq. (A2),

$$f(p, t) = \sum_{r \neq 0} f_{rs} \, e^{iarp_z} \emptyset_\upsilon(t) \tag{A13}$$

Substituting Eqs. (A13) and (A12) into Eq. (A10) we obtain the current density,

j_z

$$= \frac{2e}{(2\pi\hbar)^2} i\gamma_0 a\Delta p_\varphi \sum_{s=1}^{n} \int_0^{\frac{2\pi}{a}} \left(\sum_{r\neq 0} f_{rs}\, e^{iarp_z} \emptyset_\upsilon(t) \right) \left(\sum_{r'\neq 0} ia\, r'\varepsilon_{rs} e^{iearp_z} \right) dp_z \quad (A14)$$

But current density j_z can also be written as

$$j_z = i \sum_{s=1}^{n} j_{os} \emptyset_\upsilon(t) \quad\quad\quad (A15)$$

So from eqs. (A14) and (A15), we obtain

$$j_{os} = \frac{2e}{(2\pi\hbar)^2}\gamma_0 a\Delta p_\varphi \sum_{s=1}^{n} \int_0^{\frac{2\pi}{a}} \left(\sum_{r\neq 0} f_{rs}\, e^{iarp_z} \right) \left(\sum_{r'\neq 0} ia\, r'\varepsilon_{rs} e^{iearp_z} \right) dp_z$$

$$j_{os} = \frac{2e}{(2\pi\hbar)^2}\gamma_0 a\Delta p_\varphi \sum_{s=1}^{n} \int_0^{\frac{2\pi}{a}} \left(\sum_{r\neq 0} f_{rs} e^{iarp_z} \right) \left(\sum_{r'\neq 0} ia\, r'\varepsilon_{rs} e^{iearp_z} \right) dp_z$$

$$j_{os} = \frac{2e}{(2\pi\hbar)^2}\gamma_0 a\Delta p_\varphi \sum_{s=1}^{n}\sum_{r\neq 0}\sum_{r'\neq 0} r' f_{rs}\varepsilon_{rs} \int_0^{\frac{2\pi}{a}} e^{iea(r+r')p_z} dp_z \quad\quad (A16)$$

Noting that each of r and r' is summation from $-\infty$ to $+\infty$, we integrate Eq. (A16) and have,

$$j_{os} = \frac{2e}{(2\pi\hbar)^2}\gamma_0 a\Delta p_\varphi \sum_{s=1}^{n} 2 \sum_{r=1} 2 \sum_{r'=1} r' f_{rs}\varepsilon_{rs} \frac{2\pi}{a} \delta_{r,-r'}$$

$$j_{os} = \frac{2e}{(2\pi\hbar)^2}\gamma_0 a\Delta p_\varphi \sum_{s=1}^{n} 4 \sum_{r=1} r' f_{rs}\varepsilon_{rs} \frac{2\pi}{a}$$

$$j_{os} = \frac{2e}{(2\pi\hbar)^2}\frac{2\pi}{a}\gamma_0 a\Delta p_\varphi 4 \sum_{s=1}^{n} \sum_{r=1} r f_{rs}\varepsilon_{rs} \quad\quad\quad (A17)$$

Simplifying the constant terms in

$$\frac{2e^2}{(2\pi\hbar)^2}\frac{2\pi}{a}\gamma_0 a^2\Delta p_\varphi 4 = \frac{4e^2}{\pi\hbar^2}\gamma_0 a\Delta p_\varphi = \frac{4e^2}{\pi\hbar^2}\gamma_0 \frac{\pi\sqrt{3}}{an} = \frac{4\,e^2\gamma_0\sqrt{3}}{n\hbar^2} \quad\quad (A18)$$

$$j_{os} = \frac{4\,e^2\gamma_0\sqrt{3}}{n\hbar^2}\sum_{r=1} r \sum_{s=1}^{n} f_{rs}\varepsilon_{rs} \tag{A19}$$

Substituting Eq. (A19) into Eq. (A15) and using Eq. (A8), we have

$$j_z = i\sum_{s=1}^{n} j_{os}\emptyset_v(t) = \frac{4\,e^2\gamma_0\sqrt{3}}{n\hbar^2}\,i\sum_{r=1}\frac{r(1 - iearE_0\tau)}{1 + (earE_0\tau)^2}\sum_{s=1}^{n} f_{rs}\varepsilon_{rs} \tag{A20}$$

Now expanding Eq. (A20) and considering the real part we have,

$$j_z = \frac{4\,e^2\gamma_0\sqrt{3}}{n\hbar^2}\sum_{r=1}^{\infty}\frac{r^2eaE_0\tau}{1 + (earE_0\tau)^2}\sum_{s=1}^{n} f_{rs}\varepsilon_{rs} \tag{A21}$$

High-frequency Differential Conductivity in Zigzag Carbon nanotube

Substituting Eqs. (A2) and (A3) into Eq.(A1) and using

$E(t) = E_0 + E_1 cos\omega t$ we get,

$$\frac{\partial \emptyset_\upsilon(t)}{\partial t} + \left[i(earE_0 + earE_1 cos\omega t) + \frac{1}{\tau} \right] \emptyset_\upsilon(t) = \frac{1}{\tau} \qquad (B1)$$

Solving the homogeneous differential equation corresponding to Eq.(B1) we

obtain

$$\emptyset_\upsilon(t) = C(t)e^{-\int \left[i(earE_0 + earE_1 cos\omega t) + \frac{1}{\tau} \right] dt}$$

$$= C(t)e^{-iearE_0 t}.e^{-\frac{iearE_1 sin\omega t}{\omega}}.e^{-\frac{t}{\tau}} \qquad (B2)$$

Then by differentiating eq. (B2) we have

$$\frac{\partial \emptyset_\upsilon(t)}{\partial t} = \left[\frac{\partial C(t)}{\partial t} - i(earE_0 + earE_1 cos\omega t)C(t) \right]$$

$$\times \left(e^{-iearE_0 t}.e^{-\frac{iearE_1 sin\omega t}{\omega}}.e^{-\frac{t}{\tau}} \right)$$

Substituting for $\emptyset_\upsilon(t)$ and $\frac{\partial \emptyset_\upsilon(t)}{\partial t}$ in Eq. (B1)

$$\frac{\partial C(t)}{\partial t}e^{-iearE_0 t}.e^{-\frac{iearE_1 sin\omega t}{\omega}}.e^{-\frac{t}{\tau}} = \frac{F_{rs}}{\tau}$$

$$\Rightarrow C(t) = \int \frac{1}{\tau}e^{iearE_0 t}.e^{\frac{iearE_1 sin\omega t}{\omega}}.e^{\frac{t}{\tau}}dt \qquad (B3)$$

The integrand in eq. (B3) can be written as,

126

$$e^{(iearE_0+\frac{1}{\tau})t}.e^{\frac{iearE_1 sin\omega t}{\omega}}$$

Let $\quad \beta = \dfrac{eaE_1}{\omega}$

Using the Bessel function expression

$$exp(\pm ir\beta sin\omega t) = \sum_{k=-\infty}^{\infty} J_k(r\beta)\, exp(\pm ik\omega t) \qquad\qquad (B4)$$

Hence the integrand in (B3) becomes

$$\sum_{k=-\infty}^{\infty} J_k(r\beta)\, exp\left[\frac{1+i(earE_0+k\omega)\tau}{\tau}\right]t \qquad\qquad (B5)$$

Substituting Eq. (B5) into (B3) we obtain,

$$C(t) = \sum_{k=-\infty}^{\infty} J_k(r\beta)\frac{1}{1+i(earE_0+k\omega)\tau}\, exp\left[\frac{1+i(earE_0+k\omega)\tau}{\tau}\right]t$$

Therefore the expression for $\emptyset_\upsilon(t)$ in Eq. (B2) becomes

$$\emptyset_\upsilon(t)_= \left[\sum_{k=-\infty}^{\infty} J_n(\beta)\frac{1}{1+i(earE_0+k\omega)\tau}\, exp\left[\frac{1+i(earE_0+k\omega)\tau}{\tau}\right]t\right]$$

$$\times \left(e^{-iearE_0 t}.e^{-\frac{iearE_1 sin\omega t}{\omega}}.e^{-\frac{t}{\tau}}\right)$$

$$\emptyset_\upsilon(t) = exp\left(-\frac{iearE_1 sin\omega t}{\omega}\right)\sum_{k=-\infty}^{\infty} J_k(\beta)\frac{1}{1+i(earE_0+k\omega)\tau}e^{k\omega\tau t} \qquad (B6)$$

Using the Bessel function expression

127

$$exp(\pm ir\beta sin\omega t) = \sum_{m=-\infty}^{\infty} J_m(r\beta)\, exp(\pm im\omega t)$$

We obtain,

$$\emptyset_\upsilon(t) = \sum_{k=-\infty}^{\infty}\sum_{m=-\infty}^{\infty} \frac{J_k(r\beta)J_m(r\beta)}{1+i(earE_0+k\omega)\tau}\, exp(i(k-m)\omega t)$$

Let us change indeces $k-m=\upsilon$. Then,

$$\emptyset_\upsilon(t) = \sum_{k=-\infty}^{\infty}\sum_{m=-\infty}^{\infty} \frac{J_k(r\beta)J_{k-\upsilon}(r\beta)}{1+i(earE_0+k\omega)\tau}\, exp(i\upsilon\omega t)$$

Averaging over a period of time t

$$\emptyset_\upsilon(t) = \sum_{k=-\infty}^{\infty} \frac{J_k^2(r\beta)}{1+i(\Omega r+k\omega)\tau} \qquad (B7)$$

Where $\Omega = eaE_0$

The surface current density is defined by

$$j_z = \frac{2e}{(2\pi\hbar)^2}\iint f(p)\, v_z(p)d^2p, \qquad (B8)$$

or

$$j_z = \frac{2e}{(2\pi\hbar)^2}\sum_{s=1}^{n}\int_0^{\frac{2\pi}{a}} f\left(p_z, s\Delta p_\varphi, \emptyset_\upsilon(t)\right) v_z\left(p_z, s\Delta p_\varphi\right)dp_z \qquad (B9)$$

Where the integration is over the first Brillouin zone, v_z is given by

$$v_z\left(p_z, s\Delta p_\varphi\right) = \frac{\partial \varepsilon_s(p_z)}{\partial p_z} \qquad (B10)$$

$$\frac{\varepsilon(p_z, s\Delta p_\varphi)}{\gamma_0} = \varepsilon_s(p_z) = \sum_{r \neq 0} \varepsilon_{rs} \, e^{iarp_z}$$

$$v_z((p_z, s\Delta p_z) = \gamma_0 \sum_{r \neq 0} \frac{\partial\left(\varepsilon_{rs} e^{iearp_z}\right)}{\partial p_z} = \gamma_0 \sum_{r \neq 0} iar \, \varepsilon_{rs} e^{iearp_z} \qquad (B11)$$

From Eq. (A2),

$$f(p) = \sum_{r \neq 0} f_{rs} \, e^{iarp_z} \emptyset_\upsilon(\mathrm{t}) \qquad\qquad (B12)$$

Substituting Eqs. (B12) and (B11) into Eq. (B9) we obtain the current density as,

$$j_z$$

$$= \frac{2e}{(2\pi\hbar)^2} i\gamma_0 a\Delta p_\varphi \sum_{s=1}^{n} \int_0^{\frac{2\pi}{a}} \left(\sum_{r \neq 0} f_{rs} \, e^{iarp_z} \emptyset_\upsilon(\mathrm{t})\right)\left(\sum_{r' \neq 0} ia \, r' \varepsilon_{rs} e^{iearp_z}\right) dp_z (B13)$$

But current density J_z can also be written as

$$j_z = i \sum_{s=1}^{n} j_{os} \emptyset_\upsilon(t) \qquad\qquad (B14)$$

$$j_z = \frac{2e}{(2\pi\hbar)^2} i\gamma_0 a\Delta p_\varphi \sum_{s=1}^{n} \int_0^{\frac{2\pi}{a}} \left(\sum_{r \neq 0} f_{rs} \, e^{iarp_z} \sum_{k=-\infty}^{\infty} \frac{J_k^2(r\beta)}{1 + i(\Omega r + k\omega)\tau}\right)$$

$$\times \left(\sum_{r' \neq 0} ia \, r' \varepsilon_{rs} e^{iearp_z}\right) dp_z$$

$$j_z = \frac{2e}{(2\pi\hbar)^2} i\gamma_0 a\Delta p_\varphi \sum_{s=1}^{n} \int_0^{\frac{2\pi}{a}} \left(\sum_{r \neq 0} \sum_{r \neq 0} f_{rs} \, e^{iarp_z} \sum_{k=-\infty}^{\infty} \frac{J_k^2(r\beta)}{1 + i(\Omega r + k\omega)\tau}\right)$$

$$\times \left(\sum_{r' \neq 0} ia \, r' \varepsilon_{rs} e^{iearp_z}\right) dp_z$$

$$j_z = \frac{2e}{(2\pi\hbar)^2} i\gamma_0 a\Delta p_\varphi \sum_{s=1}^{n}\sum_{r\neq 0}\sum_{r'\neq 0} r' f_{rs}\varepsilon_{rs} \sum_{k=-\infty}^{\infty} \frac{J_k^2(r\beta)}{1+i(\Omega r + k\omega)\tau}$$

$$\times \int_0^{\frac{2\pi}{a}} e^{iea(r+r')p_z} dp_z \quad (B15)$$

Noting that each of r and r' is summation from $-\infty$ to $+\infty$, we integrate Eq. (B15) and obtain,

j_z
$$= \frac{2e}{(2\pi\hbar)^2} i\gamma_0 a\Delta p_\varphi \sum_{s=1}^{n} 2\sum_{r=1} 2\sum_{r'=1} r' f_{rs}\varepsilon_{rs} \sum_{k=-\infty}^{\infty} \frac{J_k^2(r\beta)}{1+i(\Omega r + k\omega)\tau} \frac{2\pi}{a}\delta_{r,-r'}$$

Taking the r and r' summations over $1 \leq r \leq \infty$ and $1 \leq r' \leq \infty$, we add a factor 2 for each of the r and r' is summation from $-\infty$ to $+\infty$,

$$j_z = \frac{2e}{(2\pi\hbar)^2} i\gamma_0 a\Delta p_\varphi \sum_{s=1}^{n} 4\sum_{r=1} r' f_{rs}\varepsilon_{rs} \sum_{k=-\infty}^{\infty} \frac{J_k^2(r\beta)}{1+i(\Omega r + k\omega)\tau} \frac{2\pi}{a}$$

j_z
$$= \frac{2e}{(2\pi\hbar)^2} \frac{2\pi}{a} i\gamma_0 a\Delta p_\varphi 4 \sum_{r=1} r \sum_{s=1}^{n} f_{rs}\varepsilon_{rs} \sum_{k=-\infty}^{\infty} \frac{J_k^2(r\beta)(1-i(\Omega r + k\omega)\tau)}{1+\big((\Omega r + k\omega)\tau\big)^2} \quad (B16)$$

Now expanding Eq. (B16) and considering the real part we have,

$$j_z = \frac{2e^2}{(2\pi\hbar)^2} \frac{2\pi}{a}\gamma_0 a^2\Delta p_\varphi 4 \sum_{r=1} r \sum_{s=1}^{n} f_{rs}\varepsilon_{rs} \sum_{k=-\infty}^{\infty} \frac{J_k^2(r\beta)(\Omega r + k\omega)\tau}{1+\big((\Omega r + k\omega)\tau\big)^2} \quad (B17)$$

Simplifying the constant terms in (B 17)

$$\frac{2e}{(2\pi\hbar)^2}\frac{2\pi}{a}\gamma_0 a\Delta p_\varphi 4 = \frac{4e}{\pi\hbar^2}\gamma_0\Delta p_\varphi = \frac{4e}{\hbar^2}\gamma_0 \frac{2\hbar\sqrt{3}}{3an} = \frac{8e\gamma_0}{\sqrt{3}\hbar n a_{c-c}} \quad (B18)$$

Eq. (B17), then becomes,

130

$$j_z = \frac{8e\gamma_0}{\sqrt{3}\hbar n a_{c-c}} \sum_{r=1}^{\infty} r \sum_{s=1}^{n} f_{rs}\varepsilon_{rs} \sum_{k=-\infty}^{\infty} \frac{J_k^2(r\beta)(\Omega r + k\omega)\tau}{1 + ((\Omega r + k\omega)\tau)^2} \qquad (B19)$$

From (B16) we obtain

$$j_z = \frac{8e\gamma_0}{\sqrt{3}\hbar n a_{c-c}} \sum_{r=1}^{\infty} r \sum_{s=1}^{n} f_{rs}\varepsilon_{rs} \left[\frac{J_0^2(r\beta)(i + (\Omega r)\tau)}{1 + (\Omega r\tau)^2} \right.$$

$$\left. + \sum_{k=1}^{\infty} \frac{J_1^2(r\beta)(i + (\omega + \Omega r)\tau)}{1 + ((\Omega r + \omega)\tau)^2} + \sum_{k=-1}^{\infty} \frac{J_{-1}^2(r\beta)(i + (\Omega r - \omega)\tau)}{1 + ((\Omega r - \omega)\tau)^2} \right]$$

When the electric field amplitudes are small $\beta \ll 1$, we can use the Bessel

function approximation $J_{\pm 1}^2 \sim (r\beta/2)^2$ and $J_0^2 \sim 1 - \frac{r^2\beta^2}{2}$

$$j_z = \frac{8e\gamma_0}{\sqrt{3}\hbar n a_{c-c}} \sum_{r=1}^{\infty} r \sum_{s=1}^{n} f_{rs}\varepsilon_{rs} \left[\left(1 - \frac{r^2\beta^2}{2}\right)\left(\frac{(i + (\Omega r)\tau)}{1 + (\Omega \tau)^2}\right) \right.$$

$$\left. + \frac{r^2\beta^2}{4} \left(\frac{(i + (\omega + \Omega r)\tau)}{1 + ((\Omega r + \omega)\tau)^2} + \frac{(i + (\Omega r - \omega)\tau)}{1 + ((\Omega r - \omega)\tau)^2} \right) \right]$$

Considering the real part we obtain,

$$j_z = \frac{8e\gamma_0}{\sqrt{3}\hbar n a_{c-c}} \left(\frac{(\Omega r\tau)r^2\beta^2}{2} \right) \sum_{r=1}^{\infty} r^2 \sum_{s=1}^{n} f_{rs}\varepsilon_{rs}$$

$$\times \left(\frac{(1 + (\omega\tau)^2 - (\Omega r\tau)^2)}{\left[1 + ((\Omega r - \omega)\tau)^2\right]\left[1 + ((\Omega r + \omega)\tau)^2\right]} \right) \qquad (B20)$$

and the imaginary part

$$j_z = \frac{8e\gamma_0}{\sqrt{3}\hbar n a_{c-c}} \left(\frac{(\omega\tau)r^2\beta^2}{2}\right) \sum_{r=1}^{\infty} r \sum_{s=1}^{n} f_{rs}\varepsilon_{rs}$$

$$\times \left(\frac{i\omega\tau(1 - 3(\Omega r\tau)^2 + (\omega\tau)^2)}{[1 + (\Omega r\tau)^2]\left[1 + ((\Omega r - \omega)\tau)^2\right]\left[1 + ((\Omega r + \omega)\tau)^2\right]}\right) \quad (B21)$$

APPENDIX C

Substituting Eqs. (A2) and (A3) into Eq.(A1) and using

$$E(t) = E_0 + E_1 cos\omega_1 t + E_2 cos\omega_2 t \quad \text{we get}$$

$$\frac{\partial \emptyset_\upsilon(t)}{\partial t} + \left[i(earE_0 + earE_1 cos\omega_1 t + earE_2 cos\omega_2 t) + \frac{1}{\tau}\right]\emptyset_\upsilon(t) = \frac{1}{\tau} \quad (1C)$$

Solving the homogeneous differential equation corresponding to Eq.(1C) we obtain

$$\emptyset_\upsilon(t) = C(t)e^{-\int\left[i(earE_0 + earE_1 cos\omega_1 t + earE_2 cos\omega_2 t) + \frac{1}{\tau}\right]dt}$$

$$= C(t)e^{-iearE_0 t}.e^{-\frac{iearE_1 sin\omega_1 t}{\omega_1}}.e^{-\frac{iearE_2 sin\omega_2 t}{\omega_2}}.e^{-\frac{t}{\tau}} \qquad (2C)$$

Then by differentiating eq. (2C) we have

$$\frac{\partial \emptyset_\upsilon(t)}{\partial t} = \left[\frac{\partial C(t)}{\partial t} - i(earE_0 + earE_1 cos\omega_1 t + earE_2 cos\omega_2 t)C(t)\right]$$

$$\times e^{-iearE_0 t}. \quad e^{-\frac{iearE_1 sin\omega_1 t}{\omega_1}}.e^{-\frac{iearE_2 sin\omega_2 t}{\omega_2}}.e^{-\frac{t}{\tau}}$$

Substituting for $\emptyset_\upsilon(t)$ and $\frac{\partial \emptyset_\upsilon(t)}{\partial t}$ in Eq. (1C)

$$\frac{\partial C(t)}{\partial t}e^{-iearE_0 t}.e^{-\frac{iearE_1 sin\omega_1 t}{\omega_1}}.e^{-\frac{iearE_2 sin\omega_2 t}{\omega_2}}.e^{-\frac{t}{\tau}} = \frac{1}{\tau}$$

$$\Rightarrow C(t) = \int \frac{1}{\tau}e^{iearE_0 t}.e^{-\frac{iearE_1 sin\omega_1 t}{\omega_1}}.e^{-\frac{iearE_2 sin\omega_2 t}{\omega_2}}.e^{-\frac{t}{\tau}}dt \quad (3C)$$

The integrand in eq. (3C) can be written as,

$$e^{(iearE_0 + \frac{1}{\tau})t} \cdot e^{-\frac{iearE_1 sin\omega_1 t}{\omega_1}} \cdot e^{-\frac{iearE_2 sin\omega_2 t}{\omega_2}}$$

Let $\quad \beta_1 = \frac{eaE_1}{\omega_1}$ and $\beta_2 = \frac{eaE_2}{\omega_2}$

Using the Bessel function expression

$$exp(\pm ir\beta sin\omega t) = \sum_{k=-\infty}^{\infty} J_k(r\beta) \, exp(\pm ik\omega t) \qquad\qquad (4C)$$

$$\sum_{k_1,k_2 =-\infty}^{\infty} J_{k_1}(r\beta_1) J_{k_2}(r\beta_2) exp\left[\frac{1 + i(earE_0 + k_1\omega_1 + k_2\omega_2)\tau}{\tau}\right] t \qquad (5C)$$

Substituting Eq. (5C) into (3C) we obtain,

$$C(t) = \sum_{K_1,K_2 =-\infty}^{\infty} J_{k_1}(r\beta_1) J_{k_2}(r\beta_2) exp\frac{[1 + i(earE_0 + k_1\omega_1 + k_2\omega_2)\tau]t}{1 + i(earE_0 + k_1\omega_1 + k_2\omega_2)\tau}$$

Therefore the expression for f_r in Eq. (2C) becomes

$$\emptyset_\upsilon(t)_= \left(e^{-\frac{iearE_1 sin\omega_1 t}{\omega_1}} \cdot e^{-\frac{iearE_2 sin\omega_2 t}{\omega_2}}\right)$$

$$\times \sum_{k_1,k_2 =-\infty}^{\infty} J_{k_1}(r\beta_1) J_{k_2}(r\beta_2) exp\frac{[i(k_1\omega_1 + k_2\omega_2)]t}{1 + i(earE_0 + k_1\omega_1 + k_2\omega_2)\tau}$$

Using the Bessel function expression

$$exp(\pm ir\beta sin\omega t) = \sum_{m=-\infty}^{\infty} J_n(r\beta) \, exp(\pm im\omega t)$$

Let us change indeces $k_\iota - m_\iota = \upsilon_\iota$. Then

134

$$\emptyset_\upsilon(t) = \sum_{k_1,k_2=-\infty}^{\infty} \sum_{m_1,m_2=-\infty}^{\infty} J_{k_1}(r\beta_1)J_{k_2}(r\beta_2)J_{k_1-v_1}(r\beta_1)J_{k_2-v_2}(r\beta_2)$$

$$\times \left(exp \frac{(iv_1\omega_1 + iv_2\omega_2)t}{1 + i(earE_0 + k_1\omega_1 + k_2\omega_2)\tau} \right) \quad (6C)$$

$$\emptyset_\upsilon(t) = \sum_{k_1,k_2=-\infty}^{\infty} \sum_{v_1,v_2=-\infty=-\infty}^{\infty} J_{k_1}(r\beta_1)J_{k_2}(r\beta_2)J_{k_1-v_1}(r\beta_1)J_{k_2-v_2}(r\beta_2)$$

$$\times \left(\frac{1 - i(earE_0 + k_1\omega_1 + k_2\omega_2)\tau}{1 + \left((earE_0 + k_1\omega_1 + k_2\omega_2)\tau\right)^2} \right) \quad (7C)$$

Now going through steps (B8 –B18) in appendix B, we obtain,

$$j_{z=} \frac{8e\gamma_0}{\sqrt{3}\,\hbar n a_{c-c}} \sum_{r=1}^{\infty} r \sum_{k_1,k_2=-\infty}^{\infty} \sum_{v_1,v_2=-\infty}^{\infty} J_{k_1}(r\beta_1)J_{k_2}(r\beta_2)J_{k_1-v_1}(r\beta_1)J_{k_2-v_2}(r\beta_2)$$

$$\times \left(\frac{(earE_0 + k_1\omega_1 + k_2\omega_2)\tau}{1 + \left((earE_0 + k_1\omega_1 + k_2\omega_2)\tau\right)^2} \right) \sum_{s=1}^{n} f_{rs}\varepsilon_{rs} \quad (8C)$$

APPENDIX D

Substituting Eqs. (A2) and (A3) into Eq.(A1) and using

$E(t) = E_0 + E_1 cos\omega_1 t + E_2 cos(\omega_2 t + \theta)$ we get

$$\frac{\partial \emptyset_\upsilon(t)}{\partial t} + \left[i\big(earE_0 + earE_1 cos\omega_1 t + earE_2 cos(\omega_2 t + \theta)\big) + \frac{1}{\tau} \right] \emptyset_\upsilon(t)$$

$$= \frac{1}{\tau} (1D)$$

Solving the homogeneous differential equation corresponding to Eq.(1D) we

obtain

$$\emptyset_\upsilon(t) = C(t)e^{-\int \left[i\left(earE_0 + earE_1 cos\omega_1 t + earE_2 cos(\omega_2 t + \theta)\right) + \frac{1}{\tau}\right] dt}$$

$$= C(t)e^{-iearE_0 t} . e^{-\frac{iearE_1 sin\omega_1 t}{\omega_1}} . e^{-\frac{iearE_2 sin(\omega_2 t + \theta)}{\omega_2}} . e^{-\frac{t}{\tau}} \qquad (2D)$$

Then by differentiating eq.((2D) we have

$$\frac{\partial \emptyset_\upsilon(t)}{\partial t} = \left[\frac{\partial C(t)}{\partial t} - i\big(earE_0 + earE_1 cos\omega_1 t + earE_2 cos(\omega_2 t + \theta)\big)C(t) \right]$$

$$\times e^{-iearE_0 t} . \quad e^{-\frac{iearE_1 sin\omega_1 t}{\omega_1}} . e^{-\frac{iearE_2 sin(\omega_2 t + \theta)}{\omega_2}} . e^{-\frac{t}{\tau}}$$

Substituting for $\emptyset_\upsilon(t)$ and $\frac{\partial \emptyset_\upsilon(t)}{\partial t}$ in Eq. (1D)

$$\frac{\partial C(t)}{\partial t} e^{-iearE_0 t} . e^{-\frac{iearE_1 sin\omega_1 t}{\omega_1}} . e^{-\frac{iearE_2 sin((\omega_2 t + \theta))}{\omega_2}} . e^{-\frac{t}{\tau}} = \frac{1}{\tau}$$

$$\Rightarrow C(t) = \int \frac{1}{\tau} e^{iearE_0 t} . e^{-\frac{iearE_1 sin\omega_1 t}{\omega_1}} . e^{-\frac{iearE_2 sin((\omega_2 t + \theta))}{\omega_2}} . e^{-\frac{t}{\tau}} dt \quad (3D)$$

The integrand in eq. (3D) can be written as,

$$e^{(iearE_0+\frac{1}{\tau})t} \cdot e^{-\frac{iearE_1 sin\omega_1 t}{\omega_1}} \cdot e^{-\frac{iearE_2 sin(\omega_2 t+\theta)}{\omega_2}}$$

Let $\beta_1 = \dfrac{earE_1}{\omega_1}$ and $\beta_2 = \dfrac{eaE_2}{\omega_2}$

Using the Bessel function expression

$$exp(\pm ir\beta sin\omega t) = \sum_{k=-\infty}^{\infty} J_k(r\beta)\, exp(\pm ik\omega t) \qquad (4D)$$

Therefore integrand in (3D) becomes

$$\sum_{k_1,k_2=-\infty}^{\infty} J_{k_1}(r\beta_1) J_{k_2}(r\beta_2) exp\left[\frac{1+i(earE_0+k_1\omega_1+k_2\omega_2)\tau}{\tau}\right] t.\, exp(ik_2\theta) \ (5D)$$

Substituting Eq. (5D) into (3D) we obtain,

$$C(t) = \sum_{k_1,k_2=-\infty}^{\infty} J_{k_1}(r\beta_1) J_{k_2}(r\beta_2) exp$$

$$\times \left(\frac{exp[1+i(earE_0+k_1\omega_1+k_2\omega_2)\tau]t}{1+i(earE_0+k_1\omega_1+k_2\omega_2)\tau}\right) exp(ik_2\theta)$$

Therefore the expression for $\emptyset_\upsilon(t)$ in Eq. (2D) becomes

$$\emptyset_\upsilon(t) = \left(e^{-\frac{iearE_1 sin\omega_1 t}{\omega_1}} \cdot e^{-\frac{iearE_2 sin((\omega_2 t+\theta_1))}{\omega_2}}\right)$$

$$\times \sum_{k_1,k_2 =-\infty}^{\infty} J_{k_1}(r\beta_1) J_{k_2}(r\beta_2) exp \frac{[i(k_1\omega_1 + k_2\omega_2)]t}{1 + i(earE_0 + k_1\omega_1 + k_2\omega_2)\tau} exp(ik_2\theta)$$

Using the Bessel function expression

$$exp(\pm ir\beta sin\omega t) = \sum_{m=-\infty}^{\infty} J_m(r\beta) \, exp(\pm im\omega t)$$

Let us change indeces $k_\iota - m_\iota = \upsilon_\iota$. Then

$$\emptyset_\upsilon(t) = \sum_{k_1,k_2 =-\infty}^{\infty} \sum_{m_1,m_2 =-\infty}^{\infty} J_{k_1}(r\beta_1) J_{k_2}(r\beta_2) J_{m_1}(r\beta_1) J_{m_2}(r\beta_2)$$

$$\times \left(exp \frac{[i(k_1 - m_1)\omega_1 + i(k_2 - m_2)\omega_2]t}{1 + i(earE_0 + k_1\omega_1 + k_2\omega_2)\tau} \right) expi((k_2 - m_2)\theta)$$

$$\emptyset_\upsilon(t) = \sum_{k_1,k_2 =-\infty}^{\infty} \sum_{\upsilon_1,\upsilon_2 =-\infty}^{\infty} J_{k_1}(r\beta_1) J_{k_2}(r\beta_2) J_{k_1-\upsilon_1}(r\beta_1) J_{k_2-\upsilon_2}(r\beta_2)$$

$$\times \left(exp \frac{[i\upsilon_1\omega_1 + i\upsilon_2\omega_2]t}{1 + i(earE_0 + k_1\omega_1 + k_2\omega_2)\tau} \right) exp(i\upsilon_2\theta) \quad (6D)$$

$$\emptyset_\upsilon(t) = \sum_{k_1,k_2 =-\infty}^{\infty} \sum_{\upsilon_1,\upsilon_2 =-\infty}^{\infty} J_{k_1}(r\beta_1) J_{k_2}(r\beta_2) J_{k_1-\upsilon_1}(r\beta_1) J_{k_2-\upsilon_2}(r\beta_2)$$

$$\times \left(\frac{exp(i\upsilon_1\omega_1 t + i\upsilon_2(\omega_2 t + \theta))}{1 + i(earE_0 + k_1\omega_1 + k_2\omega_2)\tau} \right) exp(i\upsilon_2\theta)$$

$$\emptyset_\upsilon(t) = \sum_{K_1,K_2 =-\infty}^{\infty} \sum_{\upsilon_1,\upsilon_2 =-\infty}^{\infty} J_{K_1}(r\beta_1) J_{K_2}(r\beta_2) J_{K_1-\upsilon_1}(r\beta_1) J_{K_2-\upsilon_2}(r\beta_2)$$

$$\times \left(\frac{(1 - i(earE_0 + K_1\omega_1 + K_2\omega_2)\tau)}{1 + ((earE_0 + K_1\omega_1 + K_2\omega_2)\tau)^2} \right)$$

$$\times \{cos(v_1\omega_1 t + v_2(\omega_2 t + \theta)) + isin(v_1\omega_1 t + v_2(\omega_2 t + \theta))\} \quad (7D)$$

Following the steps developed in Eqs. (B8-B18) in appendix B. The current density obtained is

$$j_{z=} \frac{8e\gamma_0}{\sqrt{3}\,\hbar na_{c-c}} \sum_{r=1}^{\infty} r \left[\frac{(earE_0 + k_1\omega_1 + k_2\omega_2)\tau cos(v_2\theta) + sin(v_2\theta)}{1 + ((earE_0 + k_1\omega_1 + k_2\omega_2)\tau)^2} \right]$$

$$\times \sum_{k_1,k_2 = -\infty}^{\infty} \sum_{v_1,v_2 = -\infty}^{\infty} J_{k_1}(r\beta_1)J_{k_2}(r\beta_2)J_{k_1-v_1}(r\beta_1)J_{k_2-v_2}(r\beta_2) \sum_{s=1}^{n} f_{rs}\varepsilon_{rs} \quad (8D)$$

Substituting Eqs. (A2) and (A3) into Eq.(A1) and using

$$E(t) = E_1 cos\omega_1 t + E_2 cos(\omega_2 t + \theta) \quad \text{we get}$$

$$\frac{\partial \emptyset_\upsilon(t)}{\partial t} + \left[i\left(earE_1 cos\omega_1 t + earE_2 cos(\omega_2 t + \theta)\right) + \frac{1}{\tau} \right] \emptyset_\upsilon(t) = \frac{1}{\tau} \quad (1E)$$

Solving the homogeneous differential equation corresponding to Eq.(1E) we obtain

$$\emptyset_\upsilon(t) = C(t)e^{-\int \left[i(earE_1 cos\omega_1 t + earE_2 cos(\omega_2 t + \theta)) + \frac{1}{\tau} \right] dt}$$

$$= C(t)e^{-\frac{iearE_1 sin\omega_1 t}{\omega_1}} . e^{-\frac{iearE_2 sin(\omega_2 t + \theta)}{\omega_2}} . e^{-\frac{t}{\tau}} \quad (2E)$$

Then by differentiating eq.((2E) we have

$$\frac{\partial \emptyset_\upsilon(t)}{\partial t} = \left[\frac{\partial C(t)}{\partial t} - i\left(earE_1 cos\omega_1 t + earE_2 cos(\omega_2 t + \theta)\right)C(t) \right]$$

$$\times \quad e^{-\frac{iearE_1 sin\omega_1 t}{\omega_1}} . e^{-\frac{iearE_2 sin(\omega_2 t + \theta)}{\omega_2}} . e^{-\frac{t}{\tau}}$$

Substituting for $\emptyset_\upsilon(t)$ and $\frac{\partial \emptyset_\upsilon(t)}{\partial t}$ in Eq. (1E)

$$\frac{\partial C(t)}{\partial t} e^{-\frac{iearE_1 sin\omega_1 t}{\omega_1}} . e^{-\frac{iearE_2 sin((\omega_2 t + \theta))}{\omega_2}} . e^{-\frac{t}{\tau}} = \frac{1}{\tau}$$

$$\Rightarrow C(t) = \int \frac{1}{\tau} e^{\frac{iearE_1 sin\omega_1 t}{\omega_1}} . e^{\frac{iearE_2 sin((\omega_2 t + \theta))}{\omega_2}} . e^{\frac{t}{\tau}} dt \quad (3E)$$

The integrand in eq. (3E) can be written as,

$$e^{\frac{t}{\tau}}.\, e^{\frac{iearE_1 sin\omega_1 t}{\omega_1}}.\, e^{\frac{iearE_2 sin(\omega_2 t+\theta)}{\omega_2}}$$

Let $\quad \beta_1 = \dfrac{eaE_1}{\omega_1}$ and $\beta_2 = \dfrac{eaE_2}{\omega_2}$

Using the Bessel function expression

$$exp(\pm ir\beta sin\omega t) = \sum_{k=-\infty}^{\infty} J_n(r\beta)\, exp(\pm ik\omega t) \qquad (4E)$$

Therefore the integrand in (3E) becomes,

$$\sum_{k_1,k_2 =-\infty}^{\infty} J_{k_1}(r\beta_1) J_{k_2}(r\beta_2) exp\left[\frac{1+i(k_1\omega_1 + k_2\omega_2)\tau}{\tau}\right] t.\, exp(ik_2\theta) \qquad (5E)$$

Substituting Eq. (5E) into (3E) we obtain,

$$C(t) = \sum_{k_1,k_2 =-\infty}^{\infty} J_{k_1}(r\beta_1) J_{k_2}(r\beta_2) \left[\frac{exp[1+i(k_1\omega_1 + k_2\omega_2)\tau]t}{1+i(k_1\omega_1 + k_2\omega_2)\tau}\right] exp(in_2\theta)$$

Therefore the expression for $\emptyset_\upsilon(t)$ in Eq. (2E) becomes

$$\emptyset_\upsilon(t) = \left(e^{-\frac{ieaE_1 sin\omega_1 t}{\omega_1}}.\, e^{-\frac{ieaE_2 sin((\omega_2 t+\theta_1))}{\omega_2}}\right)$$

$$\times \sum_{k_1,k_2 =-\infty}^{\infty} J_{K_1}(r\beta_1) J_{K_2}(r\beta_2) \frac{exp[1+i(k_1\omega_1 + k_2\omega_2)]t}{1+i(k_1\omega_1 + k_2\omega_2)\tau} exp(ik_2\theta)$$

Using the Bessel function expression

$$exp(\pm ir\beta sin\omega t) = \sum_{m=-\infty}^{\infty} J_n(r\beta) \, exp(\pm im\omega t)$$

Let us change indeces $k_\iota - m_\iota = \upsilon_\iota$. Then

$$\emptyset_\upsilon(t)_{=} \sum_{k_1,k_2 =-\infty}^{\infty} \sum_{m_1,m_2 =-\infty}^{\infty} J_{k_1}(r\beta_1)J_{k_2}(r\beta_2)J_{m_1}(r\beta_1)J_{m_2}(r\beta_2)$$

$$\times \left(exp \frac{[i(k_1 - m_1)\omega_1 + i(k_2 - m_2)\omega_2]t}{1 + i(k_1\omega_1 + k_2\omega_2)\tau} \right) expi\big((k_2 - m_2)\theta\big)$$

$$\emptyset_\upsilon(t)_{=} \sum_{k_1,k_2 =-\infty}^{\infty} \sum_{\upsilon_1,\upsilon_2 =-\infty}^{\infty} J_{k_1}(r\beta_1)J_{k_2}(r\beta_2)J_{k_1-\upsilon_1}(r\beta_1)J_{k_2-\upsilon_2}(r\beta_2)$$

$$\times \left(exp \frac{[i\upsilon_1\omega_1 + i\upsilon_2\omega_2]t}{1 + i(k_1\omega_1 + k_2\omega_2)\tau} \right) exp(i\upsilon_2\theta) \quad (6E)$$

$$\emptyset_\upsilon(t)_{=} \sum_{k_1,k_2 =-\infty}^{\infty} \sum_{\upsilon_1,\upsilon_2 =-\infty}^{\infty} J_{k_1}(r\beta_1)J_{k_2}(r\beta_2)J_{k_1-\upsilon_1}(r\beta_1)J_{k_2-\upsilon_2}(r\beta_2)$$

$$\times \left(\frac{exp\big(i\upsilon_1\omega_1 t + i\upsilon_2(\omega_2 t + \theta)\big)}{1 + i(k_1\omega_1 + k_2\omega_2)\tau} \right)$$

$$\emptyset_\upsilon(t)_{=} \sum_{k_1,k_2 =-\infty}^{\infty} \sum_{\upsilon_1,\upsilon_2 =-\infty}^{\infty} J_{k_1}(r\beta_1)J_{k_2}(r\beta_2)J_{k_1-\upsilon_1}(r\beta_1)J_{k_2-\upsilon_2}(r\beta_2)$$

$$\times \left(\frac{1 - i(k_1\omega_1 + k_2\omega_2)\tau}{1 + \left((k_1\omega_1 + k_2\omega_2)\tau\right)^2} \right) \times \left\{ cos\big(\upsilon_1\omega_1 t + \upsilon_2(\omega_2 t + \theta)\big) \right.$$

$$\left. + isin\big(\upsilon_1\omega_1 t + \upsilon_2(\omega_2 t + \theta)\big) \right\} \qquad (7E)$$

Following the steps developed in Eqs. (B8-B18) in appendix B. The current density obtained is

$$j_{z=} \frac{8e\gamma_0}{\sqrt{3}\,\hbar n a_{c-c}} \sum_{r=1}^{\infty} r \left[\frac{(k_1\omega_1 + k_2\omega_2)\tau cos(\upsilon_2\theta) + sin(\upsilon_2\theta)}{1 + \left((k_1\omega_1 + k_2\omega_2)\tau\right)^2} \right]$$

$$\times \sum_{k_1,k_2 = -\infty}^{\infty} \sum_{\upsilon_1,\upsilon_2 = -\infty}^{\infty} J_{k_1}(r\beta_1) J_{k_2}(r\beta_2) J_{k_1-\upsilon_1}(r\beta_1) J_{k_2-\upsilon_2}(r\beta_2) \sum_{s=1}^{n} f_{rs}\varepsilon_{rs} \quad (8E)$$

Taking $\omega_1 = \Omega$ and $\omega_2 = 2\Omega$ Eq. (8E) becomes

$$j_{z=} \frac{8e\gamma_0}{\sqrt{3}\,\hbar n a_{c-c}} \sum_{r=1}^{\infty} r \left[\frac{(k_1 + 2k_2)\Omega\tau cos(\upsilon_2\theta) + sin(\upsilon_2\theta)}{1 + \left((k_1 + 2k_2)\Omega\tau\right)^2} \right]$$

$$\times \sum_{k_1,k_2 = -\infty}^{\infty} \sum_{\upsilon = -\infty}^{\infty} J_{k_1}(r\beta_1) J_{k_2}(r\beta_2) J_{k_1-2\upsilon}(r\beta_1) J_{k_2-\upsilon}\big(r\beta_2\big) \sum_{s=1}^{n} f_{rs}\varepsilon_{rs} \quad (9E)$$

Taking terms of $k_2 = 1$ and $\upsilon = 1$ we obtain

$$\sum_{k_2=1}^{\infty} \sum_{\upsilon=1}^{\infty} J_{k_2}(r\beta_2) J_{k_2-\upsilon}(r\beta_2) = J_1(r\beta_2) J_0(r\beta_2)$$

We employ

$$J_{\pm 1}(r\beta_2) \sim {r\beta_2}/{2} \;\; ; \;\; J_0(r\beta_2) \sim 1 - \left({r^2\beta_2{}^2}/{4} \right)$$

Hence,

$$\sum_{k_2=1}^{\infty}\sum_{v=1}^{\infty} J_{k_2}(r\beta_2)J_{k_2-v}(r\beta_2) = J_1(r\beta_2)J_0(r\beta_2) = \left(\frac{r\beta_2}{2}\right)\left(1-\left(\frac{r^2\beta_2^2}{4}\right)\right)$$

$$\sum_{k_2=1}^{\infty}\sum_{v=1}^{\infty} J_{k_2}(r\beta_2)J_{k_2-v}(r\beta_2) = J_1(r\beta_2)J_0(r\beta_2) \cong \frac{r\beta_2}{2} \quad (10E)$$

Substituting Eq. (10E) into Eq. (9E) and taking $k = (k_1 + k_2)$ we obtain

$$j_z = \frac{2e^2\gamma_0 a}{\sqrt{3}\,\hbar na_{c-c}} E_2\cos\theta \sum_{r=1}^{\infty} r^2 \sum_{k=-\infty}^{\infty} \frac{kJ_k(r\beta_1)J_{k-2}(r\beta_1)}{1+(k\Omega\tau)^2} \sum_{s=1}^{n} f_{rs}\varepsilon_{rs} \quad (11E)$$

Following the approach of [30]

We can rewrite (9E) in the form

$$j_z = \frac{8e\gamma_0}{\sqrt{3}\hbar na_{c-c}} \sum_{r=1}^{\infty} r[A(\mu_1,\mu_2,v) + B(\mu_1,\mu_2,v)]$$

$$\times \sum_{k_1,k_2=-\infty}^{\infty}\sum_{v=-\infty}^{\infty} J_{k_1}(r\beta_1)J_{k_2}(r\beta_2)J_{k_1-2v}(r\beta_1)J_{k_2+v}(r\beta_2)\sum_{s=1}^{n} f_{rs}\varepsilon_{rs} \quad (10E)$$

Where

$$A(\mu_1,\mu_2,v) = \frac{(k_1+2k_2)\Omega\tau\cos(v_2\theta)}{1+\left((k_1+2k_2)\Omega\tau\right)^2}, \quad B(\mu_1,\mu_2,v) = \frac{\sin(v_2\theta)}{1+\left((k_1+2k_2)\Omega\tau\right)^2}, \quad (11E)$$

Using the Bessel function property $J_n(r\beta) \cong r\beta^n$ for $\beta \ll 1$, we shall consider

only nonvanishing lowest order in $\beta_{1,2} \ll 1$ terms in (10E). We start with terms of

$[k_1 = 0, k_2 = 0, v_2 = \pm1]$

$$[A(0,0,1) + B(0,0,1)]J_0(\beta_1)J_0(\beta_2)J_{-2}(\beta_1)J_1(\beta_2) +$$

$$[A(0,0,-1) + B(0,0,-1)]J_0(r\beta_1)J_0(r\beta_2)J_2(r\beta_1)J_{-1}(r\beta_2) =$$

$$2sinJ_0(r\beta_1)J_0(r\beta_2)J_2(r\beta_1)J_1(r\beta_2) \tag{12E}$$

$$[A(0,-1,1) + B(0,-1,1)]J_0(\beta_1)J_{-1}(\beta_2)J_{-2}(\beta_1)J_0(\beta_2) + [A(0,1,-1) +$$

$$B(0,1,-1)]J_0(\beta_1)J_1(\beta_2)J_2(\beta_1)J_0(\beta_2) = 2\left[\frac{2x}{1+4x^2} - \frac{sin\theta}{1+4x^2}\right] \tag{13E}$$

$$[A(1,0,1) + B(1,0,1)]J_1(r\beta_1)J_0(r\beta_2)J_{-1}(r\beta_1)J_1(r\beta_2) + [A(-1,0,-1) +$$

$$B(-1,0,-1)]J_{-1}(r\beta_1)J_0(r\beta_2)J_1(r\beta_1)J_{-1}(r\beta_2) =$$

$$-2\left[\frac{xcos\theta}{1+x^2} + \frac{sin\theta}{1+x^2}\right]J_1^2(r\beta_1)J_0(r\beta_2)J_1(r\beta_2) \tag{14E}$$

$$[A(1,-1,1) + B(1,-1,1)]J_1(r\beta_1)J_{-1}(r\beta_2)J_{-1}(r\beta_1)J_2(r\beta_2) + [A(-1,1,-1) +$$

$$B(-1,1,-1)]J_{-1}(r\beta_1)J_1(r\beta_2)J_1(r\beta_1)J_0(r\beta_2) =$$

$$2\left[\frac{-xcos\theta}{1+x^2} + \frac{sin\theta}{1+x^2}\right]J_1^2(r\beta_1)J_0(r\beta_2)J_1(r\beta_2) \tag{15E}$$

$$[A(2,0,1) + B(2,0,1)]J_2(\beta_1)J_0(\beta_2)J_0(\beta_1)J_1(\beta_2) +$$

$$[A(-2,0,-1) + B(-2,0,-1)]J_{-2}(\beta_1)J_0(\beta_2)J_0(\beta_1)J_1(\beta_2) = 2\left[\frac{2xcos\theta}{1+4x^2} +\right.$$

$$\left.\frac{sin\theta}{1+4x^2}\right]J_2(\beta_1)J_0(\beta_2)J_0(\beta_1)J_1(\beta_2) \tag{16E}$$

$$[A(2,-1,1) + B(2,-1,1)]J_2(\beta_1)J_{-1}(\beta_2)J_0(\beta_1)J_1(\beta_2) + [A(-2,1,-1) +$$

$$B(-2,1,-1)]J_{-2}(\beta_1)J_1(\beta_2)J_0(\beta_1)J_0(\beta_2) =$$

$$-2\sin J_2(\beta_1)J_1(\beta_2)J_0(\beta_1)J_0(\beta_2) \qquad (16E)$$

All other terms in Eq. (10E) either compensate each other or are of the order which is greater than β^3. Combining (12E) – (16E), we get the following formular for the DC

$$
\begin{aligned}
j_{z=} &\frac{8e\gamma_0}{\sqrt{3}\hbar n a_{c-c}} \sum_{r=1}^{\infty} r \sum_{s=1}^{n} f_{rs}\varepsilon_{rs} \left[\frac{8x\cos\theta}{1+4x^2} J_0(\beta_1)J_1(\beta_2)J_2(\beta_1)J_0(\beta_2) \right. \\
&\left. - \frac{4x\cos\theta}{1+x^2} J_1^2(\beta_1)J_0(\beta_2)J_1(\beta_2) \right] \\
&\approx \frac{8e\gamma_0}{\sqrt{3}\hbar n a_{c-c}} \sum_{r=1}^{\infty} r \sum_{s=1}^{n} f_{rs}\varepsilon_{rs} \left[\frac{1}{2}\left(\frac{x}{1+4x^2} - \frac{x}{1+x^2} \right) \right] \beta_1^2 \beta_2 \cos\theta \\
&= -\frac{12e\gamma_0}{\sqrt{3}\hbar n a_{c-c}} \sum_{r=1}^{\infty} r \left(\frac{x^3}{4x^4+5x^2+1} \right) r^2 \beta_1^2 r \beta_2 \cos\theta \sum_{s=1}^{n} f_{rs}\varepsilon_{rs} \quad (E17)
\end{aligned}
$$

Where $x = \Omega\tau$ and we used the expansion (see ref [30]).

$$J_n(\beta) \approx (\beta/2)^n (1/n!), \quad , \beta \ll 1.$$

Where $\Omega = eaE_0$, $f_{rs} = \frac{a}{2\pi\Delta p_\varphi S} \int_0^{\frac{2\pi}{a}} \frac{e^{-iarp_z}}{1+\exp(\varepsilon_s(p_z)/k_B T)} dp_z$,

$\varepsilon_{rs} = \frac{a}{2\pi\gamma_0} \int_0^{\frac{2\pi}{a}} \varepsilon_s(p_z)e^{-iearp_z} dp_z$, $\beta_1 = \frac{eaE_1}{\omega_1}$ and $\beta_2 = \frac{eaE_2}{\omega_2}$,

Current Density for Armchair Carbon Nanotubes

Following similar steps in appendices A, B, C, D and E we obtain the

current densities for armchair carbon nanotubes as follows;

$$j_z = \frac{4\,e^2\gamma_0}{\sqrt{3}\,n\hbar^2}\sum_{r=1}^{\infty}\frac{r^2 E_0\tau}{1+(\Omega r\tau)^2}\sum_{s=1}^{n}f_{rs}\varepsilon_{rs}$$

$$j_z = \frac{8e\gamma_0}{3\hbar n a_{c-c}}\sum_{r=1}^{\infty}r\sum_{k=-\infty}^{\infty}\frac{J_k^2(r\beta)(\Omega r + k\omega)\tau}{1+(\Omega r + k\omega)^2\tau^2}\sum_{s=1}^{n}f_{rs}\varepsilon_{rs}$$

$$j_z = \frac{8e\gamma_0}{3\hbar n a_{c-c}}\left(\frac{(\Omega r\tau)\beta^2}{2}\right)\sum_{r=1}^{\infty}r\sum_{s=1}^{n}f_{rs}\varepsilon_{rs}$$

$$\times\left(\frac{(1+(\omega\tau)^2-(\Omega r\tau)^2)}{\left[1+((\Omega r-\omega)\tau)^2\right]\left[1+((\Omega r+\omega)\tau)^2\right]}\right)$$

and the imaginary part

$$j_z = \frac{8e\gamma_0}{3\hbar n a_{c-c}}\left(\frac{(\omega\tau)\beta^2}{2}\right)\sum_{r=1}^{\infty}r\sum_{s=1}^{n}f_{rs}\varepsilon_{rs}$$

$$\times\left(\frac{i\omega\tau(1-3(\Omega r\tau)^2+(\omega\tau)^2)}{[1+(\Omega r\tau)^2]\left[1+((\Omega r-\omega)\tau)^2\right]\left[1+((\Omega r+\omega)\tau)^2\right]}\right)$$

$$j_z = \frac{4e^2\gamma_0 a}{3\hbar n a_{c-c}}E_2\cos\theta\sum_{r=1}^{\infty}r^2\sum_{n=-\infty}^{\infty}\frac{kJ_k(r\beta_1)J_{k-2}(r\beta_1)}{1+(k\Omega\tau)^2}\sum_{s=1}^{n}f_{rs}\varepsilon_{rs}$$

147

$$\approx \frac{8e\gamma_0}{3\hbar n a_{c-c}} \sum_{r=1}^{\infty} r \sum_{s=1}^{n} f_{rs}\varepsilon_{rs} \left[\frac{1}{2}\left(\frac{x}{1+4x^2} - \frac{x}{1+x^2}\right)\right]\beta_1^2\beta_2\cos\theta$$

$$= -\frac{12e\gamma_0}{\sqrt{3}\hbar n a_{c-c}} \sum_{r=1}^{\infty} r \left(\frac{x^3}{4x^4+5x^2+1}\right)\beta_1^2\beta_2\cos\theta \sum_{s=1}^{n} f_{rs}\varepsilon_{rs}$$

Where $\Omega = ebE_0$, $f_{rs} = \frac{a}{2\pi\Delta p_\varphi S} \int_0^{\frac{2\pi}{a}} \frac{e^{-ibrp_z}}{1+exp(\varepsilon_s(p_z)/k_BT)} dp_z$,

$\varepsilon_{rs} = \frac{a}{2\pi\gamma_0} \int_0^{\frac{2\pi}{a}} \varepsilon_s(p_z)e^{-iebrp_z} dp_z$, $\beta_1 = \frac{ebE_1}{\omega_1}$ and $\beta_2 = \frac{ebE_2}{\omega_2}$,

APPENDIX F

BOLTZMANN EQUATION DERIVATION

The Boltzmann equation is an equation for the time t evolution of the distribution function $f(\vec{r}, \vec{k}, t)$ in one-particle phase space, where $\vec{r}$ and $\vec{k}$ are position and wave vector respectively.

We consider the non-equilibrium distribution function $f(\vec{r}, \vec{k}, t)$ to represent the number of electrons at time t in the phase space volume $d\vec{r} \, d\vec{k}$ about the point $\vec{r}, \vec{k}$. Hence the number of electrons per unit volume at time t in the volume element $d\vec{r} \, d\vec{k}$ about $\vec{r}, \vec{k}$ is given by $f(\vec{r}, \vec{k}, t) \frac{d\vec{r} \, d\vec{k}}{(2\pi)^3}$. Here the chance of spinflip occurring during a scattering process is usually so remote to be negligible for conduction electron in a metal and $\frac{d\vec{r} \, d\vec{k}}{(2\pi)^3}$ is just the phase space density of states. It is important to note that in equilibrium, $f(\vec{r}, \vec{k}, t)$ reduces to the Fermi distribution function as given by

$f(E) = \frac{1}{e^{(E-E_F)/K_B T}+1}$, and $f(\vec{r}, \vec{k}, t) \frac{d\vec{r} \, d\vec{k}}{(2\pi)^3}$ differs from $f(E)$ in the presence of applied fields and / or temperatue gradients. Now, let the collision rate to be a function of position $\vec{r}$ and wave vector $\vec{k}$ i.e $\tau = \tau(\vec{r}, \vec{k})$ .The collisions play the role to maintain thermodynamic equilibrium at local temperature $T(r)$ and do not alter the form of distribution function

$$f(\vec{r}, \vec{k}, t) = f_o(\vec{r}, \vec{k}, t) \frac{1}{e^{(E(\vec{k}) - E_F)/K_B T(r)} + 1} \qquad (1)$$

In the time interval dt, a fraction $\frac{dt}{\tau(\vec{r},\vec{k})}$ of the electrons with wave vector $\vec{k}$ near

position $\vec{r}$ will suffer a collision that alters the wave vector of the electrons but not

the distribution function as given by equation (1). Hence, the distribution of those

electrons which emerge after collisions with wave vector during the same interval

dt must precisely compensate for this loss. Thus

$$df(\vec{r}, \vec{k}, t) = \frac{dt}{\tau(\vec{r}, \vec{k})} f_o(\vec{r}, \vec{k})$$

or

$$\frac{df(\vec{r}, \vec{k}, t)}{dt} = \frac{f_o(\vec{r}, \vec{k})}{\tau(\vec{r}, \vec{k})} \qquad (2)$$

This is the relaxation-time approximation. If one goes for a more realistic

description of collisions, then instead of relaxation-time approximation, one

would used the probability per unit time that an electron with wave vector $\vec{k}$ will

be scattered with wave vector $\vec{k'}$ as a result of collision. This scattering

probability is defined in terms of quantity $P_{kk'}$ in the following manner. The

probability per unit time that an electron known to be occupying the state $\vec{k'}$ be

scattered into infinitesimal volume elements $d\vec{k'}$ about $\vec{k'}$ known to be

unoccupied is given by $\frac{P_{kk'} d\vec{k'}}{(2\pi)^3}$. Since transition into occupied states in volume

elements $d\vec{k'}$ about $\vec{k'}$ is forbidden by Paul exclusion principle, therefore the

actual rate of transition must be reduced by fraction of these states that actually

are occupied. This fraction is $[1 - f(\vec{k'})]$. The total probability per unit time of a collision is then calculated by summing over all final wave vectors $\vec{k}$, which is defined as $\frac{1}{\tau(\vec{k})}$.

$$\frac{1}{\tau(\vec{k})} = \int \frac{d\vec{k'}}{8\pi^3} P_{kk'} [1 - f(\vec{k'})] \qquad (3)$$

Since the electrons not only scattered out of state $\vec{k}$ but also scattered into it from other states, we represent equation (3) in different way. We define $\left(\frac{df(\vec{k})}{dt}\right)_{out}$ on the basis of equation (2) as

$$\left(\frac{df(\vec{k})}{dt}\right)_{out} = -\frac{f(\vec{k})}{\tau(\vec{k})} \qquad (4)$$

Using equation (3), we have

$$\left(\frac{df(\vec{k})}{dt}\right)_{out} = -f(\vec{k}) \int \frac{d\vec{k'}}{8\pi^3} P_{kk'} [1 - f(\vec{k'})] \qquad (5)$$

Similarly,

$$\left(\frac{df(\vec{k})}{dt}\right)_{in} = +f(\vec{k'}) \int \frac{d\vec{k'}}{8\pi^3} P_{k'k} [1 - f(\vec{k'})] \qquad (6)$$

This is because while scattering in, the electrons find only a fraction $[1 - f(\vec{k'})]$ vacant in $d\vec{k}$ about $\vec{k}$ and $f(\vec{k'})$ represents the fraction on the electrons occupying in $d\vec{k'}$ about $\vec{k'}$. Also, in this process the collision probability $P_{kk'}$

151

will be replaced by $P_{k'k}$. Since during collision electron can be scattered either in

or out of $d\vec{k}$ hence $\left(\frac{df(\vec{k})}{dt}\right)_{coll}$ is given by

$$\left(\frac{df(\vec{k})}{dt}\right)_{coll} = \left(\frac{df(\vec{k})}{dt}\right)_{in} + \left(\frac{df(\vec{k})}{dt}\right)_{out}$$

$$= \int \frac{d\vec{k'}}{8\pi^3}\{P_{kk'}f(\vec{k})[1-f(\vec{k'})] - f(\vec{k'})P_{k'k}[1-f(\vec{k})]\} \quad (7)$$

In the relaxation-time approximation, this is given by

$$\left(\frac{df(\vec{k})}{dt}\right)_{coll} = -\frac{[f(\vec{k}) - f_o(\vec{k})]}{\tau(\vec{k})} \quad (8)$$

Let us now look into the structure of nonequilibrium distribution function f at

time t from its value of an infinitesimal time dt earlier. An electron at $\vec{r}, \vec{k}$ at time

t must have been at $\vec{r} - \vec{v}(\vec{k})dt, \vec{k} - \frac{\vec{F}\,dt}{\hbar}$ at time $t - dt$, where $\vec{v}(\vec{k})$ and $\vec{F}$

represent the velocity and force on electron respectively. If there were no

collisionsm then every electron at the point $\vec{r} - \vec{v}(\vec{k})dt, \vec{k} - \frac{\vec{F}\,dt}{\hbar}$ will reach the

point $\vec{r}, \vec{k}$. Hence

$$f(\vec{r}, \vec{k}, t) = f\left(\vec{r} - \vec{v}(\vec{k})dt, \vec{k} - \frac{\vec{F}\,dt}{\hbar}, t - dt\right) \quad (9)$$

If there were collisions, then the corrections for scattering of electrons going

either in or out is given by

$$f(\vec{r}, \vec{k}, t) = f\left(\vec{r} - \vec{v}(\vec{k})dt, \vec{k} - \frac{\vec{F}dt}{\hbar}, t - dt\right) + \left(\frac{df(\vec{k})}{dt}\right)_{in} dt$$

$$+ \left(\frac{df(\vec{k})}{dt}\right)_{out} dt \qquad (10)$$

Expanding the first term of equation (10) to linear order in dt and taking the limit

as $dt \to 0$, we obtain

$$\frac{\partial f}{\partial t} + \vec{v} \cdot \frac{\partial}{\partial \vec{r}} f + \vec{F} \frac{1}{\hbar} \frac{\partial}{\partial \vec{k}} f = \left(\frac{\partial f}{\partial t}\right)_{coll} = -\frac{[f(\vec{k}) - f_o(\vec{k})]}{\tau(\vec{k})} \qquad (11)$$

APPENDIX A

QUESTIONNAIRE FOR NCCE OFFICIALS

The purpose of this interview is to gather information on NCCE and Ghana's democracy. The data is for academic purpose and the information that you provide would not be divulged to anyone. I will be very grateful if you would respond to the items as candidly as possible.

Thank you.

Section A – Biographic Data

1. Gender   Male   [   ]   Female [   ]

2. Age(years)   18-25 [   ]   26 – 30 [   ]

                   31 – 35 [   ]   36 – 40 [   ]

                   41 and above [   ]

3. Qualification   Basic Education [   ]   Secondary Education [   ]

                   Tertiary Education [   ]

   Others specify ……………………………………………………...

4. Marital Status Widowed [   ]   Separated [   ]

                   Married etc [   ]

5. Occupation   Farming / Fishing [   ] Govt. / Public / Civil Service [ ]

                   Business / Petty Trader [   ]   Artisan [   ]

                   Industry [   ]

6. Number of years in service: 1-5 years [   ]   6-10 years [ ]   11 – 15 years [   ]

          16 – 20 years [   ]   21 – 25 years [ ] 26 and above [   ]

Section B – The impact of activities of the NCCE on Ghanaians

7. Have you heard about the institution of NCCE?

   Yes [   ]   No [   ]   Not quite sure [   ]

8. Have you heard or seen the NCCE organizing a forum or education campaign either public or on the radio.

   Yes [   ]   No   [   ]   Not quite sure [   ]

9. Do you remember what they were discussing

   Yes [   ]   No   [   ]   Not quite sure [   ]

10. What was it based on?

   a.   Politics [   ]   b. Education [   ]   c. Culture [   ]

11. Have you enjoyed any seminar by the NCCE?

   Yes [   ]   No   [   ]   Not quite sure [   ]

12. How often do you experience such seminars?

   Once in a year [   ]   Twice in a year [   ] More often   [   ]

13. Do you have knowledge on some of your fundamental human rights?

   Yes [   ]   No   [   ]   Not quite sure [   ]

	Excellent	Very Good	Good	Average
14. Freedom of speech, expression and of the press				
15. Freedom of religion				
16. Freedom of assembly and association				
17. Right to equal protection of the law				
18. Right to own property				
19. Right to due process and fair trial				

If 'Yes' how would you rate your knowledge on the following:

How would you assess the following functions of the NCCE?

	Excellent	Very good	Good	Average
20. Civic Education				
21. Electoral Education				
22. Sex Education				
23. HIV/ AIDS Education.				
24. Constitutional Education				

Section C – Dissemination of Government Policies and Programmes

25. Do you know some of your civic responsibilities as a Ghanaian?

Yes [　　] No [　　] Not quite sure [　　]

26. By which of the following means did you get to know?

   Media [   ]   School [   ]   NCCE [   ] Church [   ]

27. Do you know any government policies and programmes?

   Yes   [   ]   No   [   ]   Not quite sure [   ]

Are these the ways through which the NCCE disseminates government policies

and programmes?

	S. A.	A	S. D	D.
28. Media				
29. Religious bodies				
30. Public education				
31. Civic centers				
32. Civic clubs				
33. Schools				
34. Seminars				
35. Forums				

36. Logistics is one of the difficulties confronting the NCCE.				
37. Inadequate personnel is the bane of NCCE				
38. Remuneration of NCCE official is nothing to write home about.				

39. The government has not provided adequate funding for the operations of the NCCE.				
40. The inability of the NCCE to upgrade the skills of its personnel is one of its challenges				
41. Lack of much interests by some previous government has thwarted the efforts of the NCCE				
42. Accommodation in the form of inadequate offices is a problem facing the NCCE.				
43. An inadequate official vehicle for the NCCE is also hampering the activities of the NCCE.				
44. Lack of public trust in the NCCE is also thwarting their efforts.				

Section D – Challenges Facing the NCCE

Section E – Ways of Improving the Activities of the NCCE

	S. A	A	D	S. D
45. In – service training for the officials of the NCCE.				
46. Re – introduction of civic education in schools				
47. Improving the conditions of service of NCCE personnel.				
48. Provision of logistics by the government.				
49. The media should sponsor the programmes of the NCCE as a way of honouring its social responsibilities.				
50. The government should increase the budget of NCCE				
51. Recruitment into the service should be base on qualification rather than political appointment.				
52. Provision of office accommodation to both district and regional				

APPENDIX B

INTERVIEW GUIDE FOR GENERAL PUBLIC

The purpose of this interview is to gather information on NCCE and Ghana's democracy. The data is for academic purpose and the information that you provide would not be divulged to anyone. I will be very grateful if you would respond to the items as candidly as possible.

Thank you.

Section A – Biographic Data

1. Gender :   Male [   ]   Female [   ]

2. Age(years):   18-25 [   ]   26 – 30 [   ]

      31 – 35 [   ]   36 – 40 [   ]

      42 and above [   ]

3. Qualification: Basic Education [   ]   Secondary Education [   ]

      Tertiary Education [   ]   Others specify …………….

4. Marital Status : Widowed [   ]   Separated [   ]

      Married   [   ]

5. Occupation: Farming / Fishing [   ] Govt. / Public / Civil Service [   ]

      Business / Petty Trader [   ]

      Artisan [   ]   Industry [   ]

6. Number of years in service: 1-5 years [   ]   6-10 years [   ]

      11 – 15 years [   ]   16 – 20 years [   ]

      21 – 25 years [   ]   26 and above   [   ]

Section B – The Impact of Activities of the NCCE on Ghanaians

7. Have you heard about the institution of NCCE? ……..………………………

8. Have you heard or seen the NCCE organizing a forum or education campaign

    either public or on the radio. …………..…….……………………….………

9. Do you remember what they were discussing ………………………..……

10. What was it based on? a. Politics [   ]   b. Education [   ] c. Culture [   ]

11. Have you enjoyed any seminar by the NCCE? ….……………………………

12. How often do you experience such seminars?

    Once in a year [   ]   Twice in a year [   ]   More often   [   ]

13. Do you have knowledge on some of your basic fundamental human rights?,

    …………………………………………………………………………………..

    If 'Yes' how would you rate your knowledge on the following:

	Excellent	Very good	Good	Average
14. Freedom of speech, expression and of the press				
15. Freedom of religion				
16. Freedom of assembly and association				
17. Right to equal protection of the law				
18. Right to own property				
19. Right to due process and fair trial				

How would you assess the following functions of the NCCE?

	Excellent	Very good	Good	Average
20. Civic Education				
21. Electoral Education				
22. Sex Education				
23. HIV/ AIDS Education				
24. Constitutional Education				

Section C – Dissemination of Government Policies and Programmes

25. Do you know some of your civic responsibilities as a Ghanaian? ………

26. By which of the following means did you get to know your civic responsibilities?

   Media [   ]   School [   ]   NCCE [   ]   Church [   ]

27. Do you know any government policies and programmes? ……………………

Are these the ways through which the NCCE disseminates government policies and programmes?

	S. A	A	S.D	D
28. Media				
29. Religious bodies				
30. Public education				
31. Civic centers				

32. Civic clubs				
33. Schools				
34. Seminars				
35. Fora				

36. Logistics is one of the difficulties confronting the NCCE.				
37. Inadequate personnel is the bane of NCCE				
38. Remuneration of NCCE official is nothing to write home about.				
39. The government has not provided adequate funding for the operations of the NCCE				
40. The inability of the NCCE to upgrade the skills of its personnel is one of its challenges				
41. Lack of much interests by some previous government has thwarted the efforts of the NCCE				
42. Accommodation in the form of inadequate offices is a problem facing the NCCE				
43. Inadequate official vehicle for the NCCE is also hampering the activities of the NCCE.				
44. Lack of public trust in the NCCE is also thwarting their efforts				

Section D – Challenges Facing the NCCE

Section E – Ways of Improving the Activities of the NCCE

	S. A	A	D	S. D
45. In - service training for the officials of the NCCE				
46. Re-introduction of civic education in schools				
47. Improving the conditions of service of NCCE personnel				
48. Provision of logistics by the government.				
49. The media should sponsor the programmes of the NCCE as a way of honouring its social responsibilities.				
50. The government should increase the budget of NCCE				
51. Recruitment into the service should be based on qualification rather than political appointment.				
52. Provision of office accommodation to both district and regional level				

Can the following factors help to improve the activities of the NCCE?